UNIVERSITY OF OKLAHOMA

GRADUATE COLLEGE

PEPTIDE AGGREGATION INDUCED IMMUNOGENIC CELL DEATH

A DISSERTATION

SUBMITTED TO THE GRADUATE FACULTY

in partial fulfillment of the requirements for the

Degree of

DOCTOR OF PHILOSOPHY

By

GOKHAN GUNAY
Norman, Oklahoma
2022

Downloaded from SHAREOK. Persistent Handle URL: https://hdl.handle.net/11244/336874

PEPTIDE AGGREGATION INDUCED IMMUNOGENIC CELL DEATH

A DISSERTATION APPROVED FOR THE
STEPHENSON SCHOOL OF BIOMEDICAL ENGINEERING

BY THE COMMITTEE CONSISTING OF

Dr. Handan Acar, Chair

Dr. Sepideh Razavi

Dr. Qinggong Tang

Dr. Stefan Wilhelm

© Copyright by GOKHAN GUNAY 2022
All Rights Reserved.

Acknowledgements

I would like to thank Dr. Acar for her support and guidance throughout my PhD education and providing me an opportunity in her lab. I also would like to thank my committee members Dr. Wilhelm, Dr. Tang, and Dr. Razavi for their guidance, support, and fruitful discussions.

I would like to thank Seren and my family for constantly reminding me what is really important in this life. I would like to thank Dr. Chen for his guidance and advice on how to approach academia but more importantly to life. I would like to thank the department for providing an opportunity for me to be an instructor of record for two BME lab courses. It was a great experience for me, and I can only hope that they were beneficial to students.

Table of Contents

Acknowledgements iv

List of Figures x

List of Tables xix

Abstract xx

Chapter 1: Introduction 1

1. Introduction 1

1.1. Immune System 1

1.2. Immunogenic Cell Death and Damage Associated Molecular Patterns 6

1.2.1. HMGB-1 8

1.2.2. ATP 9

1.2.3. CRT 10

1.2.4. Heat Shock Proteins 10

1.2.5. Interleukin-1 family cytokines 11

1.3. DAMPs activate immune cells 12

1.4. ICD and DAMP Release Inducers 14

1.4.1. Chemotherapeutics 14

1.4.2. Physical therapies 16

1.4.3. Antimicrobial peptides 17

1.4.4. Protein/Peptide aggregation 20

1.4.5. Peptide Aggregation Model to Induce ICD and DAMP release 23

Chapter 2: Peptide Aggregation Induced Immunogenic Rupture (PAIIR) 26

2.1. Introduction 26

2.2. Results and Discussion 31

2.2.1. Designing Peptides as ICD Inducing Tools 31

2.2.2. Cell Viability 35

2.2.3. Cell Membrane rupture Through Peptide Assembly 38

2.2.4. [II] Aggregation-Induced Cell Death is Immunogenic 43

2.2.5. Peptide Assembly Induced ICD in Different Cell Types 48

2.2.6. [II] Induced Immune Response Enhances the Specific Antibody Formation Against Influenza Antigens 50
2.3. Conclusions 54
2.4. Experimental Section 55
2.4.1. Statistical Analysis 55
2.4.2. Materials 55
2.4.3. Cell Culture and Reagents 55
2.4.4. Synthesis and Characterization of FF Peptides 56
2.4.5. Peptide Aggregation Analysis 57
2.4.6. TEM Analysis 58
2.4.7. Peptide Treatment and Viability Experiments 58
2.4.8. Induction of Different Cell Death Modalities 58
2.4.9. Protein Extraction and Quantification 59
2.4.10. Immunoblotting Reagents 59
2.4.11. Procedure 60
2.4.12. LDH Assay 60
2.4.13. Flow Cytometry 61
2.4.14. Immunocytochemistry 61
2.4.15. Cytochrome c Staining 61
2.4.16. THP-1 Differentiation 62
2.4.17. Ethics 62
2.4.18. Immunization and Sera Collection 62
2.4.19. ELISA 63
Chapter 3: Controllable Peptide Aggregation Induced Immunogenic Cell Death 64
3.1. Introduction 64
3.2. Results and Discussion 66
3.2.1. [II] aggregation kinetics depend on albumin concentration 66
3.2.2. [II] aggregation induces cell stress 67
3.2.3. [II] aggregation induced ICD can be modulated 73
3.2.4. [II] aggregation induced ICD induces protective immunity 75
3.3. Conclusions 77

3.4. Experimental section 78
3.4.1. Peptide Synthesis 78
3.4.2. Atomic Force Microscopy 79
3.4.3. Cell Culture 80
3.4.4. Peptide Preparation for in vitro Experiments 80
3.4.5. Immunoblotting, Reagents 80
3.4.6. Procedure 81
3.4.7. Immunocytochemistry 81
3.4.8. LDH Release 82
3.4.9. Propidium Iodide Staining 82
3.4.10. Bone Marrow-derived Dendritic Cell Generation 83
3.4.11. Enzyme-Linked Immunosorbent Assay (ELISA) 83
3.4.12. Ethics 83
3.4.13. Prophylactic Vaccination Model 84

Chapter 4: Tumor Spheroid Model to Study Peptide Aggregation Induced Immunogenic Cell Death 85
4.1. Introduction 85
4.1.1. Matrix-free MCTS Formation 89
4.1.1.1. Liquid Overlay Technique 89
4.1.1.2. Hanging Drop Technique 91
4.1.1.3. Spinner Flask Technique 91
4.1.1.4. Magnetic Levitation Technique 92
4.2. The effects of size and shape of the ovarian cancer spheroids on the drug resistance and migration 93
4.2.1. Abstract 94
4.2.2. Introduction 94
4.2.3. Materials & Methods 96
4.2.3.1. Cell Culture and Reagents 96
4.2.3.2. Spheroid Formation and Characterization 97
4.2.3.3. Characterization of Spheroids 98
4.2.3.4. Drug Treatment and Viability Experiments 98

4.2.3.5. Immunocytochemistry....99
4.2.3.6. Protein Extraction and Quantification....100
4.2.3.7. Immunoblotting....100
4.2.3.8. Migration Assay....101
4.2.3.9. Statistical Analysis....102
4.2.4. Results....102
4.2.4.1. Expression of Epithelial-to-Mesenchymal Markers in Monolayers of EOC Cells....102
4.2.4.2. Spheroid Formation and Characterization....104
4.2.4.3. Expression of Epithelial-to-Mesenchymal Markers in EOC Spheroids....107
4.2.4.4. Size and Shape Dependent Cytotoxicity in EOC spheroids....110
4.2.4.5. Migration Profiles of EOC Spheroids....115
4.2.5. Discussion....117
4.3. [II] aggregation-induced ICD in breast cancer spheroid model....121
4.3.1. Introduction....121
4.3.2. Results and Discussion....123
4.3.2.1. Spheroid formation of EMT6 cells....123
4.3.2.2. [II] peptide aggregation induces cell membrane damage in spheroids....125
4.3.2.3. EMT6 spheroids are resistant to chemotherapeutics....129
4.3.2.4. [II] aggregation-induced DAMP release is superior to chemotherapeutics....131
4.3.2.5. [II] peptide aggregation-induced DAMP release activates BMDCs....133
4.3.2.6. [II] treated spheroid conditioned medium is non-toxic to BMDCs....135
4.3.3. Conclusions....137
4.3.4. Experimental Section....138
4.3.4.1. Materials....138
4.3.4.2. Peptide synthesis....138
4.3.4.3. Thioflavin T (ThT) Assay....140
4.3.4.4. Cell Culture and Reagents....140
4.3.4.5. Spheroid Formation and Characterization....140
4.3.4.6. Peptide and chemotherapeutics preparation and treatment....141
4.3.4.7. LDH measurement....141
4.3.4.8. Extracellular ATP measurement....142

4.3.4.9. Extracellular dsDNA measurement....142
4.3.4.10. Immunoblotting reagents....142
4.3.4.11. Procedure....143
4.3.4.12. BMDC generation....143
4.3.4.13. Co-culture of spheroid conditioned medium with BMDCs....143
4.3.4.14. Enzyme-Linked Immunosorbent Assay (ELISA)....144
Chapter 5: Conclusions and Future Perspectives....145
References....152

List of Figures

Figure 1 Cellular immunity. Cellular immunity involves direct destruction of tumor or infected cell by cytotoxic T cells and natural killer cells. This figure is prepared using BioRender. 3

Figure 2 Functionality of antibodies. Antibodies are responsible for the following functionalities: neutralization of microbes and toxins, opsonization and phagocytosis of microbes and antibody-dependent cellular cytotoxicity (ADCC). This figure is prepared using BioRender. 4

Figure 3 DAMPs activate immune cells. This figure is prepared using BioRender. 13

Figure 4 Cell membrane damage leads to the release of DAMPs. These local DAMPs activate antigen-presenting cells for the uptake, processing, and presentation of antigens. 30

Figure 5 Peptide groups and aggregation kinetics. (A) CoOP groups and individual counterparts were used in this study. (B) CAC of co-assembled peptides with DPH. (C) Macroscopic CoOP aggregates incubated with Congo Red. (D) Determination of aggregation kinetics of CoOPs and (E) individual counterparts by ThT assay. Data are representative of three experiments. 32

Figure 6 TEM images of [VV], [WW], [LL] and [II] peptides. Scale bar: 500 nm. 34

Figure 7 Cytotoxicity of peptides to OVCAR-8 cells. Negative peptides were added to the cells, followed by corresponding positive peptides. (A) Live-dead images of OVCAR-8 cells treated with peptide combinations and corresponding individual counterparts at 6h (peptide concentration is 0.5 mM) (B) Zeta potential of individual and combined peptides. (C) Illustration of peptide preparation for [WW] and [II]. The effect of peptide preparation on cell viability for [WW] (D) and [II] (E). The scale bar is 200 μm. Data are representative of at least three experiments. Statistical analysis via one-way ANOVA test, data are mean ± SD, ****p<0.0001. 36

Figure 8 [II] induces membrane rupture. (A) Time and concentration-dependent cell membrane damage of [II] were analyzed through PI uptake (scale bar is 100 μm). (B) Time-dependent viability measurement and (C) time-dependent nuclear size analysis. (D) Actin cytoskeleton staining of [II] treated OVCAR-8 cells at 1,3 and 6h, scale bar is 20 μm. (E) Internalization of FITC-KFFIIK and (F) FITC-[II] for 1, 3 and 6h, scale bar is 100 μm. (G) Experimental plan of [II] transfer and viability experiment. (H) Effect of [II] transfer on cell viability at 6h. Data are representative of at least three experiments. Statistical analysis was done with one-way ANOVA test. Data are mean ± SD, ****p<0.0001. 41

Figure 9 Propidium iodide (PI) uptake analysis by using flow cytometry. Representative histograms of untreated cells and cells treated with 0.25-0.5 and 1 mM [II] peptide for 6h (A). Percent (PI) positive cells at 6h. 42

Figure 10 6h and 24h cell viability measurements of OVCAR-8 cells treated with 0.1, 0.2, 0.3, 0.4 and 0.5 mM [II] peptide. Statistical analysis was done by one-way analysis of variance (ANOVA) with Tukey's multiple-comparison test. Data shown are mean ± SD, ****p<0.0001. n=3 replicates. 43

Figure 11 [II] induces DAMP release and secondary pyroptosis. (A) Time-dependent LDH release. (B) Time-dependent extracellular ATP release. (C) Western blot analysis of HMGB-1 and HSP90 release at 6h. (D) Caspase-3 cleavage after treatment with Cisplatin, F/T, heat treatment and 1-2-3 and 6h of [II] treatment. (E) Phase-contrast images of control and [II] treated OVCAR-8 cells at 6h, yellow arrows indicate bubbles emerging from pyroptotic cells. (F) Caspase-3 and GSDME cleavage of OVCAR-8 cells with and without treatment with [II]. (G) Time-dependent cytochrome c release into the cytoplasm from OVCAR-8 cells. The scale bar is 100 μm. (H) Schematic

illustration of the phagocytosis assay. (I) Phagocytosis of OVCAR-8 cells by THP-1 differentiated macrophages after 6h of [II] and control treatment. Data are representative of at least three experiments. Statistical analysis via one-way ANOVA test, data are mean ± SD, ****p<0.0001.46

Figure 12 [II] induced membrane rupture and DAMP release is not cell type specific. (A) GSDME analysis of OVCAR-8, B16F10, Panc02 and 3T3 cells. (B) PI uptake at 6h of [II] treatment on cells. (C) HMGB-1 and HSP90 release to the supernatant (SN) at 6h. (D) Time dependent viability measurement. (E) Time-dependent LDH release. (F) Phase-contrast images of [II] treated fibroblasts at 1, 3 and 6h. Data are representative of at least three experiments. Statistical analysis was done by one-way ANOVA test, data shown are mean ± SD, ****p<0.0001, ***p<0.001.....49

Figure 13 PAIIR induces influenza-antigen specific antibody formation. (A) Timeline and the plan of the vaccination study: BALB/c mice were vaccinated at D0 followed by a booster at D60, serum was collected at D14, 28 and 75. (B) Antigen-specific serum IgG1 titers at D14, 28 and 75. (C) Serum IgG2a titers at D14, 28 and 75. (D) Serum IgG1 and IgG2a titers against [II] peptide at D14, D28 and D75. Statistical analysis was done by one-way analysis of variance (ANOVA) with Tukey's multiple-comparison test, data shown are mean ± SD ****p<0.0001, **p<0.01, *p<0.1 n=6 mice. 52

Figure 14 Effect of [II] peptide injection on skin. [II] peptide and PBS control were injected, and skin was monitored immediately after injection followed by 6 and 24h. 53

Figure 15 Aggregation kinetics depend on albumin concentration. AFM images of [II]-albumin structures (Scale bar = 100 nm).....67

Figure 16 [II] aggregation on the cell membrane induces cell stress (A) Immunocytochemistry of YAP localization (YAP = green, Actin = red, Nuclei = blue) (B) and phosphorylation based on aggregation (YAP-P = green). (C) Western blot analysis of YAP, YAP phosphorylation, eIF2α, and eIF2α phosphorylation in different time points, β -actin was used as an internal loading control. (D) Immunocytochemistry of CRT cell surface localization (CRT = green, Actin = red, Nuclei = blue). (Scale bars = 20 μm) 70

Figure 17 [II] aggregation on YAP phosphorylation localization. Immunocytochemistry of CRT cell surface localization (YAP phosphorylation = green, Actin = red, Nuclei = blue). (Scale bars = 20 μm) 71

Figure 18 [II] aggregation on CRT localization. Immunocytochemistry of CRT cell surface localization (CRT = green, Actin = red, Nuclei = blue). (Scale bars = 20 μm) 72

Figure 19 Quantification on CRT intensity on the cell membrane. Five random cells were selected and analyzed through ImageJ by measuring mean fluorescence intensity. 72

Figure 20 Cell membrane damage can be modulated through control of [II] peptide aggregation. (A) LDH release of cells treated with 0.5 mM [II] peptide prepared in indicated albumin %s for 3, 6 and 24h. (B) Schematic illustration showing the effect of fibrillar and oligomer-like structures on the membrane damage. (C) Propidium iodide uptake of cells treated with 0.5 mM [II] peptide prepared in indicated albumin %s for 3, 6 and 24h. The scale bar is 50 μm. 74

Figure 21 [II] peptide aggregation induced cell death stages effect immunogenicity. Experimental design involving the treatment of EMT6 cells for 1.5 and 3h with 0.5 mM [II] peptide prepared in 0.02%, 0.2% and 2% albumin, transfer of supernatant onto BMDCs and analysis of IL-1β release 24h later (A). Release of IL-1β from BMDCs at 24h (B). Propidium iodide (C) and ATP

analysis (D) of dying cells prior to injection. Experimental design for prophylactic vaccination (E). Tumor-free mice survival graph (F) This figure is prepared using BioRender. 76

Figure 22 MCTS Biology. MCTS provide an in vitro platform for the investigation of cell-cell and cell-ECM interactions. Additionally, MCTS mimic in vivo solid tumors in terms of nutrient, oxygen and pH gradients and zone formation.....88

Figure 23 Matrix-free formation techniques. A) In the liquid overlay technique, cells are seeded onto a surface that prevents adhesion, encouraging cell-cell adhesion. B) In the hanging drop technique, cells are suspended in drops from the underside of a culture plate lid. C) In the spinner flask technique, rotational motion encourages cell-cell adhesion. D) In the magnetic levitation technique, cells take in magnetic nanoparticles and are aggregated by magnetic force. 93

Figure 24. Analysis of EMT markers in OVCAR-3 and OVCAR-8 cell lines. (A) Confocal imaging of actin cytoskeleton (red, left column), E-cadherin (green, center column) and Vimentin (green, right column). Scale bar is 50 μm, and blue staining indicates DAPI (nuclei) in each image. (B) Western blotting of E-Cadherin and Vimentin; and housekeeping □-actin was included for total protein loading control. (C) Illustration of OVCAR-3 and OVCAR-8 in epithelial and mesenchymal phenotype spectrum. 103

Figure 25 Spheroid formation of ovarian cancer cell lines. OVCAR-3, SKOV-3 and OVCAR-8 spheroids were initiated with 50, 100, 200 and 500 cells and monitored for 6 days every 24h Scale bar is 100 μm.....104

Figure 26. Characterization of OVCAR-3 and OVCAR-8 spheroid formation. (A) OVCAR-3 spheroids were initiated with 50, 100, 200, and 500 cells, and images were taken on day 1 and day 6. (B) Projected surface area characterization of OVCAR-3 spheroids (C) Circularity of OVCAR-

3 spheroids at day 6 (D) Solidity of OVCAR-3 spheroids at day 6. (E) OVCAR-8 spheroids were initiated with 50, 100, 200 and 500 cells, and images were taken on day 1 and day 6 (F) Projected surface area characterization of OVCAR-8 spheroids (G) Circularity of OVCAR-8 spheroids at day 6 (H) Solidity of OVCAR-8 spheroids at day 6. For each cell numbers to initiate the spheroids, n=24 spheroids were analyzed by randomly selecting 8 spheroids from 3 independent experiments. Scale bars are 100 μm. 106

Figure 27 Projected spheroid area of OVCAR-8 spheroids from day 1 to day 6. Area of OVCAR-8 spheroids were measured every day. 3 spheroids per each independent 3 experiments were evaluated. 107

Figure 28. Morphology analysis and epithelial-to-mesenchymal marker expression of ovarian cancer spheroids. (A) Strategy for imaging of spheroids by using water immersion objective. (B) OVCAR-3 and OVCAR-8 spheroids with initiation cell numbers of 50, 100, 200 and 500 were stained for F-actins (red) and DAPI for nuclei (blue), imaged for their morphology. Scale bar is 100 μm. Inset indicates magnified sections from spheroids, scale bar is 20 μm. (C) E-Cadherin (green, left column), Vimentin (green, right column), and DAPI for nuclei (blue) imaging of OVCAR-3 and OVCAR-8 spheroids with initiation cell number of 200. Top-view panel indicates the top of the OVCAR-8 spheroids, Scale bar is 100 μm. (D) Panel indicates western blot of E-Cadherin and Vimentin from ovarian cancer monolayers and their spheroids (initiation cell number of 200). Housekeeping β-actin was included for total protein loading control. 109

Figure 29 Taxol and Cisplatin treatment of OVCAR-3 and OVCAR-8 monolayers for 48h. Cytotoxicity of Taxol and Cisplatin at various concentrations were analyzed by using Alamar Blue at 48h. 111

Figure 30 Size analysis of large OVCAR-3 and OVCAR-8 spheroids. OVCAR-3 and OVCAR-8 spheroids were initiated with 5000 cells in U-bottom 96 well plates and monitored for 6 days. Scale bar is 250 μm. 10 spheroids were analyzed. 112

Figure 31. Effect of Taxol and Cisplatin treatment for 72 h on the viability and morphology of the EOC spheroids. (A-D) OVCAR-3 and OVCAR-8 spheroids with the initiation cell number of 50, 100, 200, 500 and 5000 were treated with different concentrations of Taxol and Cisplatin and at 72h viability was measured by CellTiter-Glo3D. Statistical analysis was done by 2-way ANOVA test **** p<0.0001, *** p<0.001, ** p<0.01, * p<0.1.....113

Figure 32 Effect of Taxol and Cisplatin treatment for 48 h on the viability and morphology of the EOC spheroids. (A-D) OVCAR-3 and OVCAR-8 spheroids with the initiation cell number of 50, 100, 200, 500 and 5000 were treated with different concentrations of Taxol and Cisplatin and at 48h viability was measured by CellTiter-Glo3D. (E-G) Images represent the spheroids with the initiation cell number of 200. Scale bar is 100 μm. Statistical analysis was done by 2-way ANOVA test *** p<0.001, ** p<0.01, * p<0.1. 114

Figure 33. Migration assays. (A) Expression of the transcription factor Slug was analyzed using western blot in OVCAR-3 and OVCAR-8 both as monolayer cells and as spheroids (initiation cell number of 200). Housekeeping vinculin was included for total protein loading control. (B) Wound closure of OVCAR-3 and OVCAR-8 monolayers at 6 h, 24 h and 48 h. Scale bar is 200 μm, (C) Area closure was quantified from a total of 9 different regions for both cell lines. (D) Schematic depiction of the migration assay for spheroids. (E) 6-days old OVCAR-3 and OVCAR-8 spheroids were plated on the 6-well plates and imaged at 6-24 and 48 h after seeding. (F) Area of the spheroids and migration area was quantified at 6-24 and 48 h using ImageJ. Scale bar is 100 μm.

Total of 15 spheroids were analyzed from each group by randomly choosing 5 spheroids from 3 independent experiments. Statistical analysis was done by 2-way ANOVA test, **** p<0.0001, * p<0.1.....116

Figure 34 EMT6 spheroid formation and characterization. A. Schematic explanation of ultra-low attachment spheroid formation. B. Representative brightfield images of EMT6 spheroids for 7 days. C. Spheroid area, D. Circularity, and E. Solidity of spheroids for 7 days. The scale bar is 500 μm. 124

Figure 35 [II] aggregation induces controllable membrane damage in the EMT6 spheroid model. Relative viability measurements of A. 1 mM, B. 0.75 mM, and C. 0.5 mM [II] peptide prepared in different albumin concentrations at 24h. LDH release measurements of D. 1 mM, E. 0.75 mM, and F. 0.5 mM [II] peptide prepared in different albumin concentrations at 24h. G. ThT measurement of 1 mM, 0.75 mM, and 0.5 mM [II] peptide prepared in 1% albumin. H. Schematic showing the transition from aggregated state to fibrillar structure with increasing peptide concentration. I. Comparison of LDH release of 1 mM, 0.75 mM, and 0.5 mM [II] peptide prepared in 1% albumin. J. Representative calcein (green) and propidium iodide (red) images of spheroids treated with 1 mM, 0.75 mM, and 0.5 mM [II] peptide prepared in 1% albumin. Statistical analysis was done with a one-way ANOVA test; data are mean ± SD, **p<0.01. The scale bar is 500 μm. 128

Figure 36 IC_{50} values of chemotherapeutics in monolayer and spheroid culture. A. IC_{50} values of mitoxantrone and cisplatin on monolayer culture at 24h. The scale bar is 50 μm. B. IC_{50} values of mitoxantrone and cisplatin on spheroid culture at 24h. The scale bar is 250 μm. 130

Figure 37 DAMP release from EMT6 spheroids. A. Release of LDH, B. Extracellular ATP, C. dsDNA, and D. HMGB-1 after [II], mitoxantrone, and cisplatin treatment at 24h. E. Schematic represents the DAMPs released by [II] aggregation. Statistical analysis was done with one-way ANOVA test; data are mean ± SD, **p<0.01, ***p<0.001, ****p<0.0001.....133

Figure 38 [II] aggregation-induced DAMP release activates BMDCs. A. Experimental plan for the treatment of BMDCs with tumor spheroid conditioned mediums. B. Release of IL-6, C. IL-1β, and D. IL-10, from BMDCs at 6h and 24h after tumor spheroid conditioned medium treatment. Statistical analysis was done with two-way ANOVA test; data are mean ± SD, *p<0.1, ****p<0.0001.....134

Figure 39 [II] treated spheroid conditioned medium is not cytotoxic to BMDCs. A. Schematic of the design for the viability measurement of BMDCs. B. Viability measurement of BMDCs after incubation with spheroid conditioned mediums at 24h. C. Viability and D. LDH and E. IL-1β release (6h) of BMDCs after [II] peptide treatment. Statistical analysis was done with one-way ANOVA (B and E) and two-way ANOVA tests (C and D); data are mean ± SD, ****p<0.0001. 136

List of Tables

Table 1. DAMPs, detection methods, receptor interactions and resulting immune functionalities. 7

Table 2. ICD and DAMP release inducing agents and their potential limitations.....19

Table 3 List of acronyms.....148

Abstract

Cell death is an inevitable biological outcome, every living thing dies. However, how cells die is an important question and ultimately is decisive in homeostasis and disease progression. Immune system is in the center of health and disease conditions and its proper activation is critical for life. In case of infection/cancer, immune system recognizes and kills the infected/cancerous cells. Proper recognition and activation solely depend on the activation of specialized cells called antigen presenting cells (APCs). These cells present components of the non-host called antigens and directs the immune system towards it. Evolutionary conserved receptors on these cells are specialized to recognize several patterns and motifs. These motifs are called pathogen associated molecular patterns (PAMPs) and damage associated molecular patterns (DAMPs) exogeneous and endogenous factors, respectively. DAMPs gained increasing attention since the initial proposal of the Danger Theory, which proposes that the immune system responds to danger. One of the most infamous examples of DAMP release in disease conditions is the neurodegenerative disorders. Aggregating peptides such as amyloid beta (Aβ), damage the cell membranes of healthy cells leading to DAMP release and increased neuroinflammation. While resulting in an ultimately undesired disease progression, membrane damaging role of aggregating proteins can be harnessed for immunotherapy applications for the induction of ICD and DAMP release. However, utilization of peptides such as Aβ are difficult to synthesize, characterize and lead to uncontrollable heterogeneous structures. Biologically, antibodies form against Aβ, drastically limiting their utilization for immunotherapy applications. Therefore, tools that are easy to synthesize, characterize and mimic the functionality of

membrane damage and DAMP release without inducing serious side effects have high potential to be utilized in multiple different immunotherapy applications.

In this dissertation, an engineering platform called co-assembly of oppositely charged peptides (CoOP) and its applications in ICD and DAMP release is studied. Inspired by the aggregation induced-cell membrane damage of Aβ, we introduced two oppositely charged peptide pairs called EFFIIE and KFFIIK forming [II] peptide. We first studied the cellular consequences of [II] peptide and found that [II] peptide aggregation induces ICD and DAMP release in several different healthy and cancer cell lines. Leveraging the DAMP-releasing effect of [II] peptide, we developed a quadrivalent influenza vaccine and found significantly elevated IgG1 and IgG2a responses, corresponding to the engagement of Th2 and Th1 immunity, respectively. Next, we showed the controllability of [II] peptide aggregation, which ultimately leads to control over DAMP release and the immunogenicity of dying cells. Different aggregation profiles lead to differential membrane damage and DAMP release profiles. When cells were treated with [II] peptide at different aggregation states, the dying cells led to protection in a prophylactic vaccination model against breast cancer, and differences in aggregation status led to differential protection levels. Lastly, we used [II] peptide aggregation model in a three-dimensional spheroid model of breast cancer and compared this activity with known chemotherapeutics. [II] peptide treated spheroids displayed superior DAMP release and dendritic cell activation.

Successful stimulation of ICD and DAMP release is a fundamental and challenging strategy to induce robust antigen-specific immune response. [II] peptide aggregation is a controllable tool that can be used as an adjuvant in vaccination strategies as well as a treatment modality against cancer.

Chapter 1: Introduction

1. Introduction

Peptides are formed by amino acids bound together through peptide bonds and ultimately are the building blocks of life. They are found in every cell/tissue and have different functionalities in health and disease. Peptides facilitate several different biological functions including but not limited to, cell-receptor interactions (cell signaling, adhesion), host defense (anti-microbial peptides and anti-cancer peptides), neurodegenerative disorders (amyloid aggregation induced cell death) and specific activation of the immune system (peptide presentation). These functionalities are inheritably depended on the types and orders of amino acids forming the peptides. Due to their involvement in almost every biological process, peptides are commonly used in multiple fields of science including but not limited to, biology, chemistry, materials science, physics, biotechnology, and nanotechnology. Being biocompatible, biodegradable, and easy to synthesize had made them ideal candidates to guide biological functionalities.

1.1. Immune System

All living organisms are exposed to foreign substances (invaders) that are capable of inducing harm to the host. Starting from individual cells to multicellular organisms this constant interaction of host with invaders evolved both the host and the invader. Discriminating self from non-self primarily established a network of protection which is now referred to as the immune system. Diverse set of specialized cell types and mediators called cytokines and chemokines function to protect the host from pathogens, viruses, and cancer. Immune system is divided into two categories: innate immunity and adaptive (acquired) immunity. Innate immunity refers to

the initial line of defense against invaders, it is fast but not highly specific, however, often times does not lead to memory formation with the exception of trained immunity occurring through genetic encoding. Adaptive immunity on the other hand, is highly specific, develops over time and provides memory.

Part of innate immunity, cells called antigen presenting cells (APCs) such as dendritic cells (DCs) patrol the tissues and identify the threat (e.g., pathogens, viruses, or cancer cells). They phagocytose this threat or its components and get activated. Then, they undergo a maturation in which they process antigens (enzymatically process and placement on major histocompatibility (MHC molecules), followed by migration to the secondary lymphoid organs where they present these antigens to the adaptive immune cells called lymphocytes. These cells are evolved to possess an enormous diversity of their antigen receptors to ensure developing a response against any given pathogen. Each lymphocyte carries a slightly different antigen receptor and will only get activated upon strong receptor-antigen interaction between the lymphocyte and APCs. Once antigen is successfully recognized by a lymphocyte and the activatory signals are provided, that lymphocyte will undergo a fast proliferation to make more of the same copy, a process called clonal expansion. Successful stimulation of adaptive immunity is critical for eliminating the invaders and provides faster response due to memory formation in case of encountering the same invader in the future.

Adaptive immunity can be divided into two broad categories: cellular immunity and humoral immunity (antibody-mediated immunity). Cellular immunity refers to direct recognition and destruction of infected and cancerous cells. It involves cytotoxic effector cells called CD8 + T cells (Cytotoxic T lymphocyte, CTL) and natural killer (NK) cells **(Figure *1*)**. Once the infected or tumor

cell is recognized, CTLs and NK cells release cytotoxic mediators called perforin and granzyme B[1] and induce cell death. Successful stimulation of cellular immunity is critical in protection against infectious diseases and cancers.

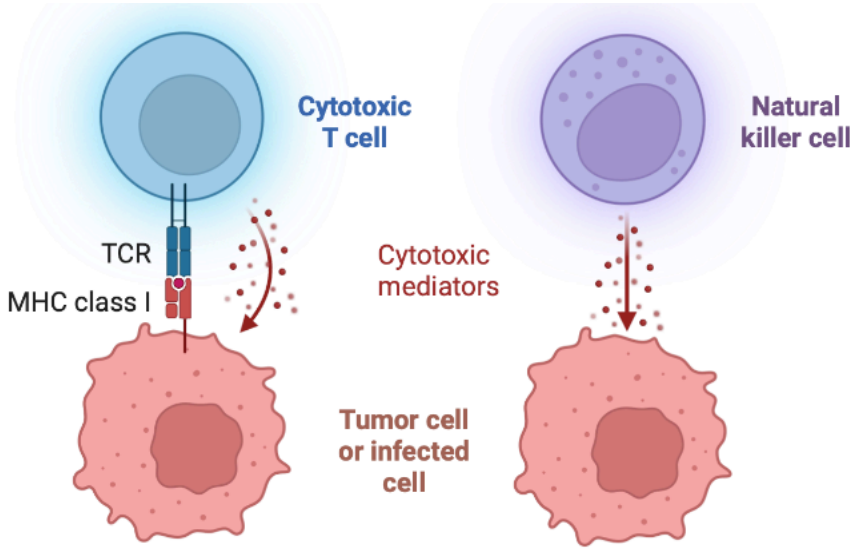


Figure 1 Cellular immunity. Cellular immunity involves direct destruction of tumor or infected cell by cytotoxic T cells and natural killer cells. This figure is prepared using BioRender.

Humoral immunity on the other hand involves the secretion antibodies which function in neutralization, phagocytosis, and antibody-dependent cellular cytotoxicity (ADCC). Antibodies also play role in the activation of complement system, which is reviewed extensively before[2]. Antibodies are composed of variable and constant regions and there are 5 types of antibodies: IgG, IgA, IgE, IgM and IgD. These antibodies recognize and bind to antigens from their variable region.

Among different antibody types, IgG is the main component of humoral immunity due to its small size, high diffisubility and its abundance which is 10-20% of plasma proteins[3]. IgG antibodies are

comprised of 4 different subclasses: IgG1, IgG2, IgG3 and IgG4. Collectively, their functionalities involve; neutralization of microbes and toxins, opsonization and phagocytosis of microbes and ADCC **(Figure *2*)**. Neutralization and phagocytosis help clearance of the antigen from the extracellular environment. ADCC, on the other hand is critical for the clearance and destruction of infected or cancerous cells that express antigens on their cell surface.

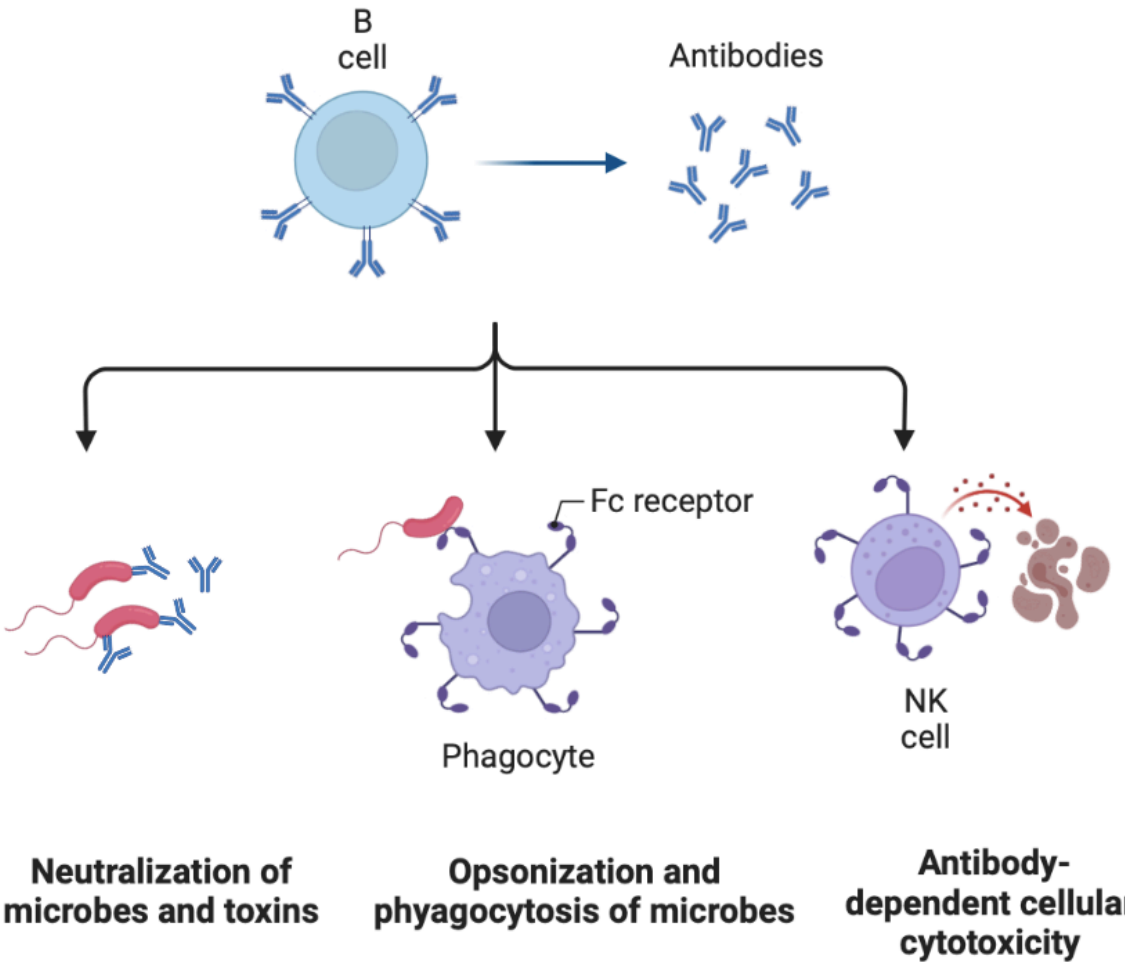


Figure 2 Functionality of antibodies. Antibodies are responsible for the following functionalities: neutralization of microbes and toxins, opsonization and phagocytosis of microbes and antibody-dependent cellular cytotoxicity (ADCC). This figure is prepared using BioRender.

Among these IgG subtypes, IgG2 antibodies have been shown to induce highest ADCC both in infections such as influenza[4] and metastatic melanoma models[5]. Fc portion of IgG2 antibody is recognized by the Fc receptors of immune cells such as natural killer cells and results in the destruction of the target cell. This is critical for the clearance of cells that are infected with viruses in case of viral infections.

Production of different types of antibodies are conveyed through the complex interactions of B cells and T helper (Th) cells. Th cells are specialized CD4 + T cells with distinct functionalities. They have different subtypes such as Th1 and Th2. As mentioned earlier, activated, and mature APCs interact with naïve T cells **(Figure 1)**. Co-stimulatory factors and release of different cytokines from APCs are decisive for Th cell differentiation. As a consequence of Th cell and B cell interaction, Th1 cells induce IgG2a production while Th2 cells induce IgG1 production from B cells. Induction of both Th1 and Th2 responses engage both humoral and cellular immunity to fight against infectious diseases and cancer.

In the context of immune system activation, the following two terms referred to as immunogenicity and antigenicity are important to distinguish. Immunogenicity is defined as the ability of an entity to induce humoral and cellular response. Antigenicity is a term defined as the ability of an antigen to be recognized by secreted antibodies or T cell receptors[6,7]. For example, in case of a dying cancer cell, immunogenicity is defined as the "cell", while antigenicity is defined by a specific tumor associated antigen present in that "cell". Most importantly, antigenicity alone is not sufficient to induce effective adaptive immunity[8,9]. This is because antigenicity alone does not stimulate co-stimulatory receptors on APCs, which are necessary for proper activation of the adaptive immunity[10]. In fact, the absence of co-stimulation rather renders immune system

towards anergy and tolerance[11]. Co-stimulatory molecules are upregulated in APCs when these cells interact with their environment through the abundant expression of evolutionary conserved receptors called pattern recognition receptors (PRRs)[12]. For a long period of time, it was considered that these "patterns" refer only to "foreign entities" called, pathogen associated molecular patterns (PAMPs) as the immune system was thought to strictly discriminate self from non-self. In 1994, Polly Matzinger proposed the "Danger Theory"[13], suggesting that detection is not about self or non-self rather to detect to protect from danger. This model supports that, damaged/dying cells from the host organism release molecules that can activate immune cells. Now, it is accepted that majority of these molecules share the same pathways for activating immune cells similar to "foreign entities". Today, these molecules are referred to as danger/damage associated molecular patterns (DAMPs) and cell death modalities involving, secretion, release or surface localization of DAMPs are referred to as immunogenic cell death (ICD).

1.2. Immunogenic Cell Death and Damage Associated Molecular Patterns

Death is the eventual biological outcome for living organisms. Substantial effort has been made so far to elucidate the mechanisms of cell death and for a long period of time, cell death was viewed under two categories: regulated apoptosis and unregulated necrosis. Recent advances revealed that there are multiple different cell death modalities triggered through different signaling pathways[14]. Necrosis originally thought to be unregulated, have been identified to involve different regulated forms; necroptosis, pyroptosis and ferroptosis, all naturally occur within the body. These are non-apoptotic cell death modalities, and they are regulated. Signaling

pathways and triggering mechanisms of these cell death modalities are explained elsewhere in detail[15,16]. However, the eventual outcome of all of them is the release of DAMPs.

Normally, DAMPs are contained within the cells, however, upon membrane damage they are released to the extracellular matrix or localized to the cell surface. They interact with local immune cells and can have immunomodulatory roles. Additionally, it is necessary to point out that DAMPs also interact with local non-immune cells such as epithelial cells, fibroblasts and endothelial cells, and take part in regulating inflammation[12].

Diverse set of molecules have been classified as DAMPs including but not limited to; high-mobility group box protein-1 (HMGB-1), ATP, Calreticulin (CRT), heat shock protein-70 (HSP70), HSP90 and IL-1 family cytokines. Each of these DAMPs are capable of activating immune cells through different receptor interactions[17] **(Table 1)**.

Table 1 DAMPs, detection methods, receptor interactions and resulting immune functionalities.

DAMPs	**Detection Method**	**Receptor Interactions**	**Immune Functions**	**Ref**
ATP	Luminescence (luciferin/luciferase assay)	$P2X_7$, $P2Y_2$	- NLRP3 inflammasome activation and IL-1β release from DCs and neutrophils - Recruitment of myeloid cells, serving as “find-me” signal for macrophages	[18–22]
HMGB-1	Immunofluorescence, western blot, ELISA, mass spectrometry	TLR-2, TLR-4, RAGE	- Induction of macrophage pyroptosis through RAGE - Processing and presentation of tumor antigens by DCs - Migration, maturation, and activation of DCs	[23–30]

CRT	Immunofluorescence, flow cytometry, mass spectrometry	LRP-1 (CD91)	- Surface localization (ecto-CRT) initiates phagocytosis of tumor cells by DCs and macrophages	[30–32]
HSP70, HSP90	Immunofluorescence, western blot, ELISA, mass spectrometry	CD14	- Cytokine production from human monocytes - Translocation of chaperoned antigens for cross presentation by DCs	[30,33–35]
mtDNA	Real-time PCR	TLR9	- Degraded mtDNA activates astrocytes to release IL-6, MCP-1, TNF-α and IL-1β,	[36–38]
DNA	Fluorimetric dyes, PCR	TLR-9, RAGE	- DNA-HMGB-1 complex induces type I IFNs and activate plasmacytoid DCs	[39]
IL-1 family cytokines: IL-1α, IL-1β, IL-18, Il-33	ELISA, western blot	IL-1R, IL-18Ra, IL-33R	- IL-1α, IL-1β and IL-33 potentiates alums adjuvancy - IL-18 induces Th1 response through inducing IFNγ	[40–43]

TLRs, Toll-like receptors; HSPs, heat shock protein; NLRP3, NLR (Nod-like receptor) family pyrin domain containing 3; ILs, interleukins; mtDNA, mitochondrial DNA; CDs, cluster of differentiations; HMGB-1, high mobility group box-1; RAGE, receptor for advanced glycation end products; TNF-α, tumor necrosis factor alpha; IFNs, interferons; LRP-1, low density lipoprotein receptor-related protein 1; DCs, dendritic cells; DAMPs, damage-associated molecular patterns; MCP-1, monocyte chemoattractant protein-1; ELISA, enzyme-linked immunosorbent assay; CRT, CRT.

1.2.1. HMGB-1

HMGB-1 is a constitutively expressed protein found in nucleus and released upon ICD[44]. Its role in ICD predominantly conveys through its interaction with TLR-4 receptor on immune cells.

During chemotherapy and radiotherapy HMGB-1-TLR4 interaction has been shown to be vital for the induction of antigen-specific T cell immunity[29]. TLR-4 agonists are able to restore the protective immunity in the absence of HMGB-1 during chemotherapeutic (oxaliplatin) induced ICD[45]. Comparably, knock down of *tlr4* gene completely abolished the protective effects of oxaliplatin in prophylactic vaccination model[46]. This activation is predominantly related with the migration, maturation, and activation DCs. Clinically, mutation in *tlr4* allele is correlated to higher metastasis rate in breast cancer patients[47] and reduced disease-free and overall survival in head and neck squamous cell carcinoma patients[48]. Similarly, in oxaliplatin treated colorectal cancer patients, loss of function in *tlr4* allele reduced progression free and overall survival[46]. HMGB-1 also interacts with receptor for advanced glycation end products (RAGE). Endocytosis of HMGB-1 through RAGE induced pyroptosis (caspase-1 dependent pathway) in macrophages[24]. However, expression of RAGE receptor is low in majority of tissues except lung tissue.

1.2.2. ATP

Stressed or dying cells release ATP into the extracellular environment[49]. Multiple chemotherapeutic drugs have been shown to induce ATP release and this effect was reported to be concentration dependent[50]. Extracellularly, ATP acts through purinergic receptors $P2X_7$ and $P2Y_2$ and contributes to the immunogenicity of dying cells. It induces inflammasome (NLRP3 pathway) formation in DCs[20] and neutrophils[19] resulting in the secretion of IL-1β.

Blocking purinergic receptor $P2X_7$ with oxiATP (antagonist) abolished the protective capacity of ferroptotic cells in a prophylactic vaccination model[51]. However, in another prophylactic vaccination model with hypericin-photodynamic therapy (ICD inducer) authors showed that, using Apyrase (an enzyme degrading ATP) or oxiATP during initial vaccination failed to reduce

anti-tumor immunity, however combination of Apyrase and oxiATP significantly reduced the anti-tumor immunity[52]. These results highlight the importance of DAMP-receptor interactions for engaging anti-tumor immunity but at the same time point towards yet-to-be-defined DAMPs that might be acting synergistically.

1.2.3. CRT

CRT (CRT) is an endoplasmic reticulum (ER) protein serving as an "eat me" signal upon surface localization (ecto-CRT) during ICD and increases the immunogenicity of tumor cells[32]. Translocation of CRT to plasma membrane conveys through ER stress response. This response is accompanied by the phosphorylation of eukaryote initiation factor 2 alpha at serine 51 (eIF2$\alpha^{(S51)}$)[53], a protein functions in response to cell stress. Later it was shown that eIF2α phosphorylation is a hallmark of ICD[54] and sole ER stress marker required for the surface localization of CRT[54]. A knock-in mutation preventing eIF2$\alpha^{(S51A)}$ phosphorylation abolished surface localization of CRT upon mitoxantrone and oxaliplatin treatment[55]. On the other hand, in photodynamic therapy CRT surface localization was dispensable of eIF2α phosphorylation[56]. Therefore, it should be stated that the molecular mechanism governing these processes remains to be fully explored and different techniques conveys through different mechanism to induce ICD.

1.2.4. Heat Shock Proteins

Heat shock proteins (HSPs) have been studied extensively for their role as DAMPs. They are conserved proteins and are the most abundant intracellular proteins in cells[57]. They are released upon necrosis and are capable to engage inflammatory signaling through NFkB pathway in DCs[58]. Bortezomib (a chemotherapeutic drug) was shown to induce anti-tumor immunity via cell surface

exposure of HSP90 on tumor cells, which was abolished in the presence of geldanamycin (HSP90 inhibitor)[59]. Additionally, HSP90 was shown to act as a chaperone for extracellular antigens and leading to DC cross presentation[34]. Additionally, other members of HSPs like HSP70 was shown to act as a cytokine and stimulate cytokine production from human monocytes[33].

1.2.5. Interleukin-1 family cytokines

IL-1 family refers to a set of cytokines including IL-1α, IL-1β, IL-18, Il-33, IL-36α, Il-36β and IL-36γ. These cytokines are released upon necrosis (unregulated and regulated forms)[60–62]. Members of IL-1 family are not secreted via ER-Golgi pathway but rather released upon necrosis. They play immunomodulatory roles when released into the extracellular environment. In vaccination settings, IL-33 has been shown to act as an adjuvant and increase the levels of IL-5, MCP-1, MIP-1a and MIP-1b similar to alum[40]. IL-1 family cytokines was shown to dictate the inflammatory phenotype, Induction of Th1, Th2 and Th17 phenotype in helper T cells was shown with IL-18, IL-33 and IL-1, respectively[63]. In fact, the efficacy of alum to induce strong adaptive immunity was linked to the release of IL-33[64].

However, these cytokines such as IL-1β, is found as pro-IL-1β and needs to be cleaved for release upon necrosis. Two-signal model for IL-1β release shows that initial stimulator, “signal one”, such as LPS leads to the upregulation of pro-IL-1β, however “signal two” such as ATP or Nigericin is required to initiate necrosis promoting the release of IL-1β[62]. However, simple necrosis would not lead to IL-1β secretion, its cleavage from pro-IL-1β is induced and therefore, IL-1β has also been classified as an inducible DAMP (iDAMP)[65]. This class of DAMPs represent the generation of a DAMP due to a modification such as post-translational modification or cleavage determined by the stress inducing stimuli. Activation of TLR receptors through PAMPs is similar to the activation

pathway of IL-1 receptors for an inflammatory outcome, both involving NFkB activation[66]. In fact, blocking of IL-1 receptor signaling abolished the inflammatory response in sterile settings[67].

1.3. DAMPs activate immune cells

As mentioned above, several different DAMPs have been characterized and studied for their role in activating immune cells. These released mediators from dying cells engage multiple different immune cells including but not limited to DCs, neutrophils and macrophages. Functionalities such as phagocytosis, antigen presentation and promotion of inflammation are eventual outcomes of these activations (**Figure 3**). **Table 1** presents the list of individual DAMPs, their receptor interactions, and their contribution to immunogenicity. It is vital to note that the eventual outcome of ICD is not dependent on a single DAMP but rather a combinatorial/synergistic activity. Silencing or using antibodies against HMGB-1[46] and CRT [32] show that the immunogenicity of cancer cells hence "protective capacity" reduces, however, does not abolish completely.

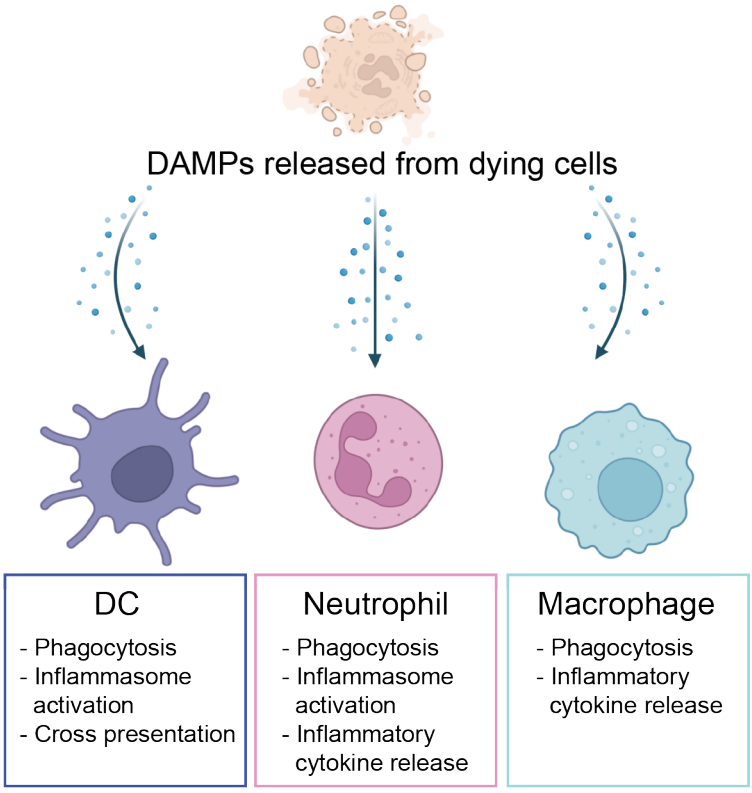


Figure 3 DAMPs activate immune cells. This figure is prepared using BioRender.

In another study, silencing of HMGB-1 did not affect the maturation of DCs and only partially abolished the anti-tumor immunity[68]. One study showed that HMGB-1, galectin-3 and S100A8/A9 (recombinant DAMPs) increase the proliferation of fibroblasts, while administration of these DAMPs individually had no effect, suggesting synergistic effects of DAMPs[69]. Mitochondrial formyl peptides are known to activate neutrophils. A synthetic peptide simulating bacterial challenge called N-formyl-Met-Leu-Phe (fMLF) was used in combination with mitochondrial DNA (mitochondrial DAMP) and secretion of IL-8 was analyzed from neutrophils. While individual peptide or mtDNA did not induce a significant release, when used together their synergistic effects significantly increased IL-8 secretion[70]. Similarly, in an influenza vaccination model, Vono et al, showed that MF59 adjuvant mechanism conveys through the extracellular ATP release from

muscle cells, which cannot be replicated by ATP administration alone, suggesting the role of other molecules[71].

1.4. ICD and DAMP Release Inducers

There are multiple techniques that induce ICD and DAMP release. These involve chemotherapeutics, physical therapies such as radiation therapy and photothermal therapy and antimicrobial peptides. Each technique has been proven to be successful in terms of ICD induction and DAMP release, however, there are different factors limiting their activities such as differences in cell type, accessibility of the tumor and applicability to different settings such as vaccination against viral infections[72,73].

1.4.1. Chemotherapeutics

Mitoxantrone, oxaliplatin and doxorubicin are widely studied chemotherapeutics for their mechanism for ICD induction and DAMPs release. Mitoxantrone has been shown to induce CRT surface localization and release of HMGB-1 and ATP. Its immunogenicity induction has been studied in different settings resulting in; higher phagocytosis of cancer cells by DCs[74], induction of CD8+ T cell activation in in vitro co-culture system[75] and protective capacity in ICD-based prophylactic vaccination models[76]. Similarly, oxaliplatin and doxorubicin has been shown to induce protective immunity in prophylactic vaccination models through DAMPs[46,77]. However, immunogenicity of chemotherapeutics is highly dependent on their concentrations. Increasing their concentrations does not necessarily correlate with higher DAMP release and immunogenicity, in fact has been shown to reduce the amount of released DAMPs for mitoxantrone, oxaliplatin and doxorubicin[46,75]. Ability to induce DAMP release for chemotherapeutics is also cell line dependent. Transfer of tumor conditioned medium after

mitomycin C treatment was stimulatory for DCs only some of the bladder cancer cell lines[73]. Similarly, etoposide treated B16-OVA and MC-38-OVA cells showed very different activation profiles of OVA specific CD8 + T cells[75]. These data suggest that the ICD and DAMP release inducing capacity of chemotherapeutics are not just dependent on concentration but also affected by the cell type as well. Changes due to cell type are caused by differential expression of certain proteins which ultimately effects the cell death modality. For example, pyroptosis is a regulated necrosis resulting in membrane damage and release of DAMPs. One of the proteins responsible for the execution of pyroptosis (a regulated necrosis) is gasdermin E (GSDME). Cleavage of GSDME by caspase-3 liberates N terminus leading to membrane pore formation[78]. In fact recently it was shown that CTLs and NK cells kill their target cancer cell through this mechanism and increase tumor suppression[79]. Therefore, drugs that can induce such cell death modality potentially offers increased anti-tumor immunity. However, GSDME is expressed as low levels in most cancer cells[80] due to methylation induced epigenetic silencing[81]. Absence of GSDME turns the cell death modality into non-ICD apoptosis. Lobaplatin, a drug that can induce pyroptosis in GSDME expressing cells has been shown to induce iDAMP IL-1β release. However, silencing of GSDME turns the pathway into apoptosis, abolishing the release of iDAMPs[42]. These data illustrate the limitations in terms of cell type for ICD inducing small drugs.

In addition, cell death induced by some other chemotherapeutics are non-ICD. Two major examples of this category are gemcitabine and cisplatin. Gemcitabine was shown to release inhibitory DAMP prostaglandin E2 and was not protective in prophylactic vaccination model[30]. Another study showed that gemcitabine was only immunogenic with HIF-1a inhibition and was not protective otherwise[82]. Cisplatin is another non-ICD inducer[83], with very low to none

protective capacity in prophylactic vaccination models[30,46]. Similar to gemcitabine, cisplatin also induces the release of prostaglandin E2[84] and fails to engage CRT surface localization and therefore, not protective[85].

1.4.2. Physical therapies

In addition to chemotherapeutics, physical therapies such as radiation therapy, and photothermal therapy has been shown to induce ICD and DAMP release as well. Radiation therapy induces cell death through damaging double strand DNA and has been shown to induce DAMP release such as HMGB-1, ATP, HSPs and CRT surface exposure[86,87]. It has been used for more than 50% of cancer patients with curative intent[88]. ICD and DAMP release induced by radiation therapy depends on the type and dose of irradiation as well as post-irradiation time. In fact, different doses of radiation therapy induces different cell death modalities; apoptosis and necrosis, in low and high dose, respectively[89].

Three types of radiation (photon, proton and carbon-ion) were tested for the surface exposure of CRT and was shown to be different depending on type and dose[90]. In fact, range, and dose of the therapy effects biological outcomes significantly. Utilizing higher doses of radiation (>15 Gy) increases number of regulatory T cells[91], which in return suppresses anti-tumor immunity. Moreover, multifractionated and single dose of radiation was shown to induce different DAMP release profiles in human prostate cancer cell lines[92]. In correlation with this study, multifractionated or single dose of radiation was shown to change the infiltration of antigen-specific effector cells[93]

Photothermal therapy (PTT) aims to selectively induce cancer cell ablation. Variety of nanoparticles (organic and inorganic) have been utilized for PTT[94]. This system has been shown

to induce tumor cell death and release of DAMPs as well as tumor associated antigens. However, thermal dose or thermal window eventually dictates the immunogenicity induced by PTT. Prussian blue nanoparticle mediated PTT showed higher levels of ATP, HMGB-1 and CRT between 63.3-66.4 °C, while higher and lower temperatures resulted in non-ICD[95]. It was discussed by Hu et al.,[94] that PTT alone is not sufficient to protect against metastasis and recurrence. In fact another study showed that gold nanoshell-enabled PTT of a single tumor delays the growth of contralateral B16-OVA tumors, however remains ineffective for less immunogenic B16-F10 tumors[96]. Same study also showed that PTT induced the generation of myeloid-derived suppressor cells leading to metastasis, however combination with adoptive T cell therapy increased the efficacy against both the primary and metastatic tumor[96]. Another strategy is to combine PTT and immunotherapy. PTT combined with glycated chitosan (GC) showed tumor regression if 75% of mice through increase DAMP release upon PTT and infiltration of APCs[97].

1.4.3. Antimicrobial peptides

Antimicrobial peptides (AMPs) are found in the host defense mechanism displaying activity against bacteria, viruses and fungi[98]. Several AMPs have been discovered and currently more than a thousand AMPs are present (natural or synthetic). Majority of AMPs share structural similarities in terms of containing hydrophobic and cationic amino acids (high amounts of lysine and arginine). AMPs interact with the negatively charged membrane through electrostatic interactions and multiple different mechanisms have been proposed for their hemolytic activity and discussed detailly elsewhere[99]. Strikingly, AMPs activity are not limited to microbes but extend to cancer cells. They bind to the phospholipid phosphatidylserines on the outer leaflet of cancer cell plasma membranes[100]. Several natural and engineered AMPs has been shown to act

as anti-cancer peptides. Majority of these AMPs either induce apoptosis[101–104] or membrane permeabilization[104,105], however only a handful has been shown to induce ICD. LTX-315 is one of the peptides inducing ICD and has been studied extensively. It induces the release of ATP, HMGB-1 and CRT exposure[106,107] and its mechanism of action is through mitochondrial outer membrane permeabilization. In B16 melanoma model LTX-315 showed tumor regression in 30/37 of the animals used in the study and was protective in 15/25 of the animals upon rechallenge[108]. The mechanism of action was later shown to be dependent on the expression of BAX and BAK proteins[109]. However, some cancer types downregulate the expression of these molecules such as breast cancer[110]. When used in a triple negative breast cancer model, LTX-315 had no protective effects upon intratumoral injection 0/8 and was partially protective in combination with doxorubicin[111]. Similarly, LTX-401 was shown to induce ICD and DAMP release from B16 melanoma cells and induced survival in 9/11 mice[112]. LTX-401 was also shown to be inducing protective effects (multiple injections) through ICD in fibrosarcoma tumor model; however, single intratumoral injection was not effective for reducing the tumor volume[113].

Development of readily available vaccines is essential to combat life-threatening infections. Recently, a bovine AMP called Bactenecin 5 was used as an adjuvant in a mycobacterial antigen vaccination model. Even though it induced the activation of macrophages, it failed to induce antigen-specific antibody production[114]. Another strategy combined the 11-mer AMP KLKL$_5$KLK with CpG-ODN and adjuvant called IC31. This adjuvant increased the production of antigen specific antibodies faster than only antigen group[115], however the protective capacity was similar to only antigen group. AMPs have potential to be utilized for different applications in the context of ICD including tumor treatment and adjuvant design for vaccination platforms. However,

current efforts have aforementioned limitations and require modifications that would increase their effectivity for increased immunological responses.

Table 2 ICD and DAMP release inducing agents and their potential limitations.

ICD and DAMP release inducing agent	**Potential limitations**	**Ref**
Chemotherapeutics	• Concentration dependent changes in DAMP release • Only a select few have been shown to induce bone fide ICD • Cancer cell type dependent immunological outcome • Release of inhibitor DAMPs	30,46,73,83,116
Physical therapies	Radiation • Type and dose dependent changes in DAMP release • Type and dose dependent changes in cell death modality • Type and dose dependent shift in anti-tumor immunity PTT • Temperature dependent changes in cell death modality • Temperature dependent changes in DAMP release • Low protection capacity when used alone	89–91,94–96
Antimicrobial peptides	• Induction of apoptosis and membrane permeabilization, however ICD has not been analyzed thoroughly for most AMPs • Not significant antibody production and protective capacity when used as adjuvants for vaccine development LTX 315 and LTX 410 • Protective effect depends on cancer type • Requires multiple injections • BAX and BAK expression dependent activity	101–105,109,113–115

1.4.4. Protein/Peptide aggregation

Aggregation of proteins/peptides such as Aβ, huntingtin and α-synuclein are common hallmarks of neurodegenerative diseases such as Alzheimer's, Huntington, and Parkinson diseases. Neuroinflammation is one of the consequences aggregations, which recently was linked to DAMPs. Damaged/dying cells activate local immune cells like astrocytes and microglia through release of DAMPs[117], elevating inflammation. One major example of DAMPs that is associated with aggregation in these disease conditions is mitochondrial DNA (mtDNA). Degraded mtDNA activates astrocytes to release IL-6, monocyte chemotactic protein-1, TNF-α and IL-1β, all of which increase inflammation[36]. Cerebrospinal fluid analyses also indicate the presence of mtDNA[118]. Moreover, administration of mtDNA or its degradation products lead to increased inflammation and Alzheimer's disease like phenotype in the hippocampus of C57BL/6 mice[119]. Another DAMP found in cerebrospinal fluid is HMGB-1[120]. As mentioned before, one of the receptors HMGB-1 interacts is TLR-4 (Table 1) and loss of function in *tlr4* has been shown to reduce the inflammatory profile induced by Ab aggregation[121].

Ab peptides are produced through the proteolytic cleavage of amyloid precursor protein and aggregate to induce cell death once cleaved. Additionally, it engages cell stress; such as ER stress marker and ICD marker: phosphorylation of eIF2α[54]. Ab aggregation induces eIF2α phosphorylation in human neuroblastoma cells[122]. Strikingly, histological analyses from Alzheimer's patients indicate increased phosphorylation of eIF2α[123]. While multiple mechanisms are under investigation regarding cell death mechanism induced by Ab aggregation[124], the biological outcome points towards the involvement of DAMPs for the progression of neurodegenerative disorders. One potential mechanism for aggregation induced cell death and

DAMP release is through sensing extracellular stimuli. The plasma membrane involves in sensing external stimuli and adapting to changes through intracellular signaling. One of the major pathways responding against a variety of external stimuli is the Hippo pathway. Recently it was shown that Ab42-mediated neurodegeneration involves the activation of the Hippo pathway, and upregulation of Hippo signaling increases neurodegeneration[125]. One of the central proteins within the Hippo pathway is yes-associated protein (YAP). YAP is a transcription factor found in the nucleus in its active form and when translocate to cytoplasm it gets inactivated. More specifically, phosphorylation of YAP at serine residue (S127) inhibits its activity and leads to its cytoplasmic retention[126] and degradation[127]. Aggregation/accumulation of Ab42 within the cytoplasm leads to neuronal necrosis and this has been correlated with a reduction in nuclear YAP levels, moreover this process was shown to occur in the early stages of AD in a mouse model[120]. This process is not solely in AD but present in other neurodegenerative disorders as well. Post-mortem cortex analysis of HD revealed reduction in nuclear YAP levels and increased phosphorylation[128].

The role of DAMPs in the context of aggregation-based progression of neurodegenerative diseases inevitably suggest the role of different cell death modalities that might be involved. Specifically, ICD modalities like necroptosis, pyroptosis and ferroptosis have been shown to be important throughout the progression of diseases[129]. Neuronal loss in AD was correlated to the phosphorylation of RIPK1, RIPK3 and MLKL[130], hallmarks of necroptosis. In fact, inhibition of necroptosis with necrosulfonamide reversed spatial memory and learning deficits in rat model of AD[131]. Role of necroptosis in different stages of AD remains to be elucidated, however, targeting necroptosis and its signaling mechanism offers a promising strategy for AD pathogenesis[132].

Another regulated necrosis modality is pyroptosis. In addition to DAMPs, Ab itself has been shown to induce NLRP1-mediated pyroptosis in neurons. Resulting inflammation increases the progression cognitive impairments which is reversed in NLRP1 or caspase-1 deficient mice[133]. Similarly, NALP3 inflammasome was also shown to be triggered upon Ab phagocytosis mediated lysosomal damage in microglia[134]. In another study, it was shown that Ab oligomers, not monomers or fibrils, engage pyroptosis through NLRP3 inflammasome for the secretion of IL-1β[135]. Iron was found to be elevated in AD patients compared to controls[136] and ferroptosis is an iron dependent regulated necrosis. One of the characteristics of this cell death modality is lipid peroxidation and high amounts of free iron was shown to initiate cell death in neurons, astrocytes and Schwann cells[137]. In fact the relation of iron accumulation and AD was proposed in 1960s[138]. Later it was shown that aging increases the free iron and contributes to Ab plaque formation[139] and through misfolding of Ab[140]. It was recently shown that Inhibition of ferroptosis AD mouse model improved neurodegeneration[141]. These studies highlight that there is growing evidence that cell death modalities and progression of neurodegenerative disorders are tightly correlated. Therefore, understanding how aggregation of proteins lead to cell death and consequences of cell death is a promising field which have potential to offer new strategies and therapeutic alternatives. More importantly, understanding that proteins aggregate and induce different cell death modalities involving ICD have tremendous application potentials for developing effective vaccines and fight against cancer. As explained before, ICD and DAMP release engage immune system, suggesting a potential path to use the idea of creating local aggregation for new treatment strategies.

However, utilization of peptides such as Ab for therapeutic purposes has multiple drawbacks. One major concern is their synthesis. Both Ab 1-40 and Ab 1-42 has been referred to as "difficult peptides" to synthesize through solid-phase peptide synthesis due to their aggregation[142]. Other issues include but not limited to; achieving high purity and unwanted aggregation within the solution during characterization experiments[143]. From a biological outcome perspective, one major drawback of using Ab as a therapeutic tool to induce ICD and DAMP release is the formation of antibodies against Ab. A study using Ab 1-15 and 1-40/42 showed that antibodies are produced against Ab and these antibodies had epitopes within Ab 1-15[144]. Therefore, utilization of Ab for developing new vaccines against infectious diseases or different cancer types would present additional challenges given that repetitive utilization would likely be inhibited by the antibodies formed against it.

1.4.5. Peptide Aggregation Model to Induce ICD and DAMP release

To overcome the limitations of aggregating peptides but to leverage their functionality. We designed a platform called CoOP[145]. This platform is based the utilization of two oppositely charged peptides for a controlled and local aggregation to induce ICD and DAMP release. We identified a peptide pair (EFFIIE and KFFIIK) called [II] peptide and utilized this technology for ICD and DAMP release for the development of vaccines and tumor treatment strategy. [II] peptide tool induces controllable ICD and DAMP release which overcomes the limitations of chemotherapeutics and physical therapies, which are often limited for their therapeutic window[90,95].

The first chapter of this thesis is focused on the background information on ICD and DAMP release. Activation of immune system is explained and roles of individual cells on stimulating

proper activation. ICD is explained and individual DAMPs and their role in activating immune cells have been detailly explained. Different techniques used to induce ICD and DAMP release are discussed including their advantages and limitations. Naturally aggregating peptides and their role in ICD induction and DAMP release were discussed along with their limitation in terms of synthesis and biological utilization for immunotherapy applications. Moreover, this chapter emphasizes the necessity of designing new materials for improved ICD and DAMP release to overcome the limitations of aforementioned techniques.

The second chapter of this thesis is focused on the utilization of [II] peptide aggregation for cell death and DAMP release. We showed that [II] peptide induces ICD and DAMP release in multiple different cell types. We analyzed the signaling mechanism and identified that [II] peptide induces secondary GSDME mediated pyroptosis (a regulated necrotic cell death modality). Lastly, leveraging the capability of [II] peptide to induce DAMP release, we used it as an adjuvant and developed a quadrivalent influenza hemagglutinin vaccine. [II] peptide increased the production antigen specific IgG1 and IgG2a antibodies. Due to the ability of [II] peptide to induce immune response through ICD and DAMP release, we named this platform as “Peptide Aggregation Induced Immunogenic Rupture” (PAIIR).

The third chapter of this thesis is focused on the modulation of [II] peptide aggregation to control cell membrane damage and immunogenicity of dying cells. We showed that albumin can be utilized to change [II] peptide aggregation ultimately influencing cell membrane damage. Individual positively and negatively charged components of [II] peptide localize on cell membranes and induce cell stress, analyzed through Hippo signaling pathway and endoplasmic reticulum signaling pathway. Immunogenicity of dying cells change as the cells continue to die.

We treated breast cancer cells with different [II] aggregation profiles and studied the immunogenicity of dying cells in a breast cancer prophylactic vaccination model.

The fourth chapter of this thesis is focused on the utilization of [II] peptide aggregation in a 3-dimensional (3D) spheroid model and the comparison of DAMP release with chemotherapeutic drugs. We first introduced a 3D spheroid model, which can be formed in different shapes and sizes. Next, we established that spheroids are resistant to chemotherapeutic drugs compared to their monolayer counterparts. Utilizing this information, we used spheroid model to study the capability of ICD and DAMP release induction by [II] peptide. We compared [II] peptide with commonly used chemotherapeutics mitoxantrone and cisplatin and showed that [II] peptide is superior in terms of DAMP release and immune cell activation.

Chapter 2: Peptide Aggregation Induced Immunogenic Rupture (PAIIR)

This section is adapted from the following publication:

Gunay, Gokhan, Seren Hamsici, Gillian A. Lang, Mark L. Lang, Susan Kovats, and Handan Acar. "Peptide Aggregation Induced Immunogenic Rupture (PAIIR)." *Advanced Science* (2022): 2105868.

2.1. Introduction

As a result of cell membrane damage or stress, cells release damage-associated molecular patterns (DAMPs) and die through immunogenic cell death (ICD), which has powerful immune system enhancing effects. Several infectious pathogens and cancers deploy strategies to limit the emission of DAMPs and escape immunosurveillance[146]. Inducing and controlling localized ICD in the presence of an antigen has a significant potential for therapeutic and protective immunity. Released DAMPs with immunostimulatory effects show "adjuvant-like" properties and engage antigen-presenting cells (APCs) to stimulate a robust, long-lasting immunity. In cancer treatment, inducing ICD and DAMP release with chemotherapeutics and photothermal therapy improves the antitumoral effect[147,148]. Similarly, engaging DAMP release enhances the antigen-specific immunity in vaccination strategies[149]. Despite this potential, the current ICD-inducing technologies are limited because they are effective only in specific applications and demonstrate off-target toxicity[150,151]. Therefore, there is an emerging clinical need for a tool that can induce controlled ICD and is effective across different cell types to increase the efficacy of current immunotherapy treatments.

Vaccination is critical for preventing the spread of respiratory viruses like influenza. However, current influenza vaccines have limited efficacy and cannot provide long-lasting and universal

protection due to the high mutation rate in HA antigens[152–154]. Induction of a strong cellular immunity against more conserved antigens of influenza is critical for universal protection[155]. However, vaccination with the influenza HA protein combined with the majority of the commercially available adjuvants have limited long-lasting universal protection[156].

Adjuvants induce antigen-specific antibodies to either tag the antigens on pathogens or infected cells for attack by effector immune cells (as in type-1 cellular response correlated to Th1) or neutralize antigen-carrying entities (as in type-2 humoral response linked to the CD4+ T cells called T helper 2, Th2)[149,157]. Most common adjuvants enhance type-2 response via Th2 and produce neutralizing antibodies, immunoglobulin G1 (IgG1). A typical Th1 response to a viral infection is characterized by recruitment of cytotoxic T lymphocytes (CTL), macrophages and NK cells, and is associated with IgG2a or IgG2c formation in mice. Particularly IgG2a production is driven by IFNγ whereas IgG1 occurs through IL-4[158]. Indeed, the expression of these antibody type is used to identify the type of immune responses in mice[159].

Naturally existing cell membrane-disrupting proteins (or peptides) often generate stress and DAMP-release through aggregation, such as perforin, gasdermins, or Aβ[160,161]. Induced membrane damage subsequently releases natural adjuvants called DAMPs, such as ATP, DNA, high-mobility group box 1 (HMGB-1), and heat shock protein 90 (HSP90)[1,162]. APCs recognize DAMPs through their pattern recognition receptors (PRRs) and become activated[163], generating non-infectious local inflammation and enhancing their ability to internalize and present antigens to activate the adaptive immune response synergistically[164]. For example, oil-in-water emulsion MF59 induced ATP release from muscle cells through intramuscular vaccination, and degradation of extracellular ATP reduced hemagglutinin (HA)-specific antibody formation when mice

immunized with HA-influenza antigens[71]. However, ATP injection alone was insufficient to induce a strong response, suggesting a synergistic effect that relies on other released DAMPs[71]. In a recent study, plasmid-encoded HMGB-1 increased the immunogenicity of a DNA vaccine, thus enhancing a specific immune response to the influenza nucleoprotein and HA proteins, and improving the survival of mice against lethal mucosal heterosubtypic influenza challenge[165]. HSP90 enhances the cross-presentation of antigens by APCs[166]. However, recombinant DAMPs have been ineffective adjuvants[167]. Therefore, technologies that induce the release of DAMPs collectively for synergistic effects are an emerging frontier in immunotherapy.

To induce such DAMP-release with a peptide that targets a specific cell membrane receptor has limitations; peptide will not be effective on the cells without the receptor or cell can mutate to reduce the expression of that receptor to gain resistance against the peptide. Therefore, rather than targeting a particular protein, in this study, we utilized the CoOP strategy to design a peptide sequence that can aggregate strong enough in the cellular environment to induce similar ICD functionality[145].

Nanomaterials built by self-assembling peptides have broad application areas in medicine. Discovery of peptide sequences that assemble into nanostructures with desired properties and functions in a biological environment is a major challenge for the field. Editing the sequence of a protein that naturally assembles in the body can accelerate the discovery of various sequences, yet the harvested properties rule their functionalities. Establishing the application of a new peptide material based on its characterized properties is a common strategy[168]. Here we applied a unique approach; instead of mimicking a naturally existing protein or peptide sequence, we aimed to mimic their function and activity with a new tool that induces ICD via CoOP strategy.

We designed peptide sequences for mimicking this activity. CoOP strategy is based on a framework (i.e., the diphenylalanine (FF) domain and terminal charges) that defines the peptide-peptide orientation and thus initiates the interactions of the peptides. However, the forces that affect the kinetics of the assembly and the properties of the final product are provided by the two amino acids of the substitution domain [XX] (we use the standard single-letter amino-acid codes throughout this work, with the CoOP pairs denoted in square brackets: [ ]). Our CoOP strategy provides a quantitative correlations between changes in the amino acid sequence of the framework and the properties of the assembly[145]. Hence, CoOP represents a uniquely powerful strategy to create small peptides with controllable aggregation profiles that can be used to design peptide-aggregation-induced immunogenic rupture (PAIIR) of the cell membrane and subsequent ICD.

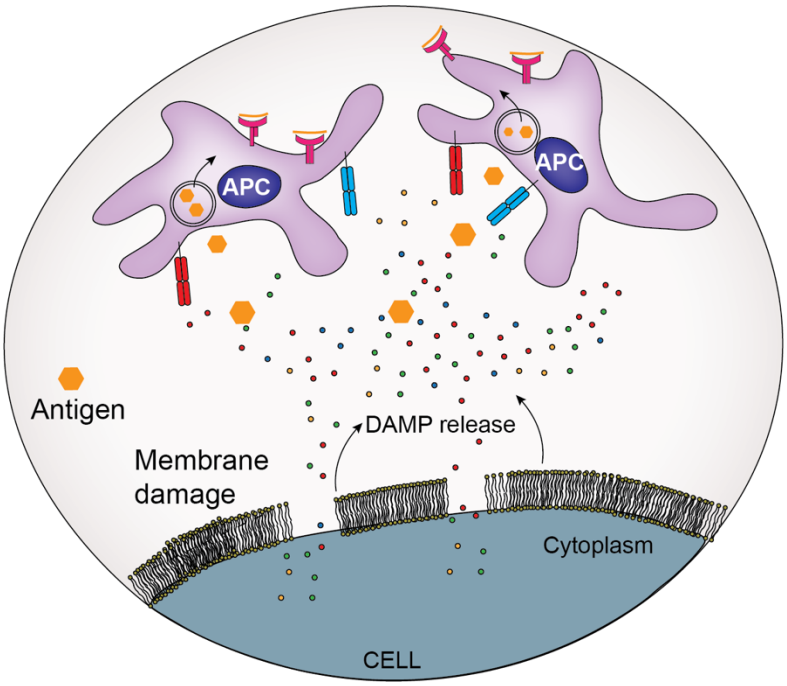


Figure 4 Cell membrane damage leads to the release of DAMPs. These local DAMPs activate antigen-presenting cells for the uptake, processing, and presentation of antigens.

Here, we hypothesize that PAIIR on cells can be utilized as a vaccine adjuvant. We showed the ICD mechanism induced by PAIIR, along with the released DAMPs. We developed an influenza vaccine and studied the immune response by mixing our new peptide tool with influenza HA proteins (**Figure 4**). We demonstrate the use of the CoOP strategy to design peptide sequences with the desired aggregation properties to compose PAIIR. We identify the mechanism of programmed ICD and demonstrate DAMP release induced by our designed peptides in multiple cell types. Upon co-administration, PAIIR enhances HA-specific IgG1 and IgG2 formation significantly compared to immunization with HA alone. Therefore, it is likely that PAIIR broadens the humoral immunity in mice. More importantly, we show that the designed peptide did not generate any specific antibody against itself. These results highlight PAIIR as a promising new tool

that can readily be injected, providing a simple, efficient, and safe method for enhancing immune response in vaccine applications.

2.2. Results and Discussion

2.2.1. Designing Peptides as ICD Inducing Tools

Engineering the fine-tuned cellular aggregation of peptides requires well-characterized intermolecular interactions[169,170]. Understanding these interactions allows the rational design of peptides to encompass desired properties, such as aggregation on the cell that induces stress for inducing ICD and cell membrane rupturing for DAMP release. We utilized the CoOP strategy to design peptides with strong enough affinity to aggregate in the cellular environment. The local charges in this design promote electrostatic interactions between two oppositely charged amino acids; the anionic carboxylate of Glutamic acid (E) and the cationic ammonium from Lysine (K) (**Figure 5A**) The deliberately short, charged design enables the internalization of CoOP-based peptides into cells[171]. Design studies on multidomain peptides revealed the importance of hydrophobic amino acid localization in the core of the structures[172]. In particular, the interplay between the backbone hydrogen bonding and hydrophobic interactions among amino acid side-chains is crucial to the formation of fibrillar structures[173]. Therefore, to change the aggregation kinetics, we studied the hydrophobic amino acids in the substitution domain ("[XX]"), with increasing hydrophobicity indices; [AA] < [VV] < [WW] < [LL] < [II] (**Figure 5A**).

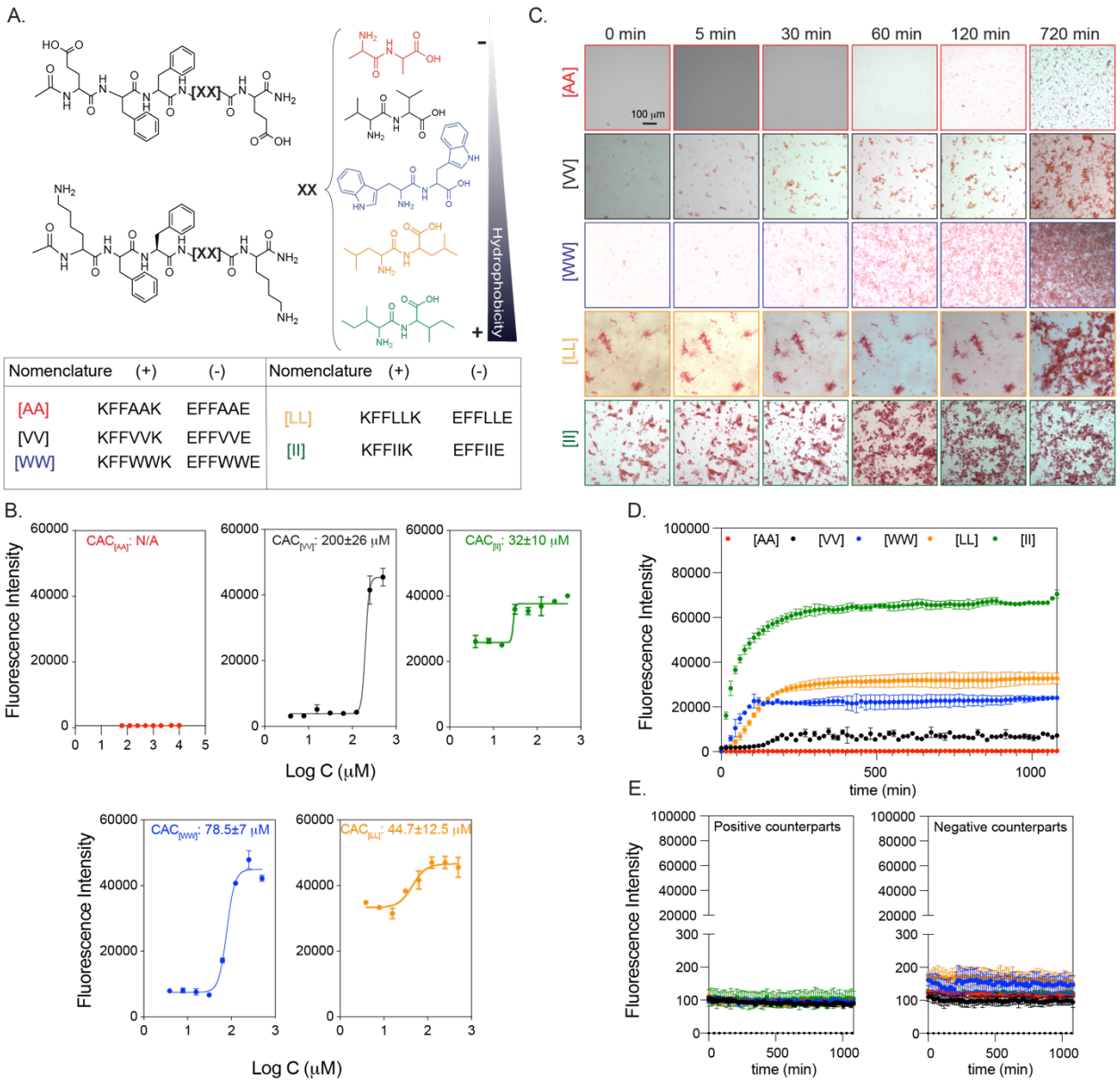


Figure 5 Peptide groups and aggregation kinetics. (A) CoOP groups and individual counterparts were used in this study. (B) CAC of co-assembled peptides with DPH. (C) Macroscopic CoOP aggregates incubated with Congo Red. (D) Determination of aggregation kinetics of CoOPs and (E) individual counterparts by ThT assay. Data are representative of three experiments.

Characterization assays were performed in 1XPBS to mimic the salt concentration in the physiological conditions. The critical aggregation concentrations (CAC), i.e., the minimum

concentration needed for co-assembly of the peptides, are measured with DPH ((1,6-diphenyl-1,3,5-hexatriene)), which becomes fluorescent when located in aggregates with hydrophobic cores[174]. The CAC values of [VV]=200±26 mM [WW]=78.5±7 mM [LL]=44.7±12.5 mM and [II]=32±10 mM followed the same trend as the hydrophobicity of the amino acids at their core **(Figure 5B).** The identified CAC values were correlated to our previous study[145]. No fluorescence was observed for [AA] even at 10 mM indicating no aggregation; therefore, this situation represents an excellent control for studying the effects of peptide aggregation, as the same concentration of peptides with similar sequences and charges will remain free components in solution.

The aggregation kinetics of the peptide pairs were measured with Congo Red and Thioflavin T (ThT) assays. Congo Red staining has been used to identify amyloid fibrils in vitro and tissue sections, emitting red light due to the binding of b-sheet rich domains, leading to a redshift in its absorbance peak from 490 to 512 nm[175]. We monitored the fluorescence of Congo red for 720 min (12 h) (**Figure 5C**) at 0.5 mM peptide concentration. [AA] precipitation appeared after 720 min; these are not likely to be ordered aggregates with hydrophobic cores because no DPH fluorescence was observed at this concentration. [II] aggregated instantaneously (0 min), while [LL] aggregates were deposited initially and became stable until 720 min. [WW] and [VV] did not show any initial aggregates but deposited after 30 min and 120 min, respectively. Despite the ease of visualization with red light, Congo Red is not as sensitive as ThT in understanding ordered structures since fluorescence methods (rather than absorption) are preferred for high-sensitivity detection[176]. Therefore, we use Congo Red as a visualization method, with ThT used for quantitative temporal measurements of oppositely charged pairs and each counterpart

individually for 1200 min (20 h). To determine the time needed for equilibrium assembly of CoOPs, we applied curve fitting to the ThT analysis (**Figure 5D**). [AA] did not assemble and thus did not show any fluorescence in ThT. For the remaining peptide pairs, the time to reach equilibrium assembly was calculated as [VV] (660 min) > [WW] (675 min) > [LL] (630 min) > [II] (510 min). Individual counterparts did not produce any fluorescence signal (**Figure 5E**). We observed that the like-charged groups alone did not aggregate, highlighting the importance of electrostatic attractions in the aggregation process (**Figure 5D**). Among the studied peptides, [II] showed the fastest aggregation and the highest fluorescence intensity, indicating that [II] has the highest affinity to each other, and these peptides are stacked in a more well-ordered structure than the other CoOPs. The TEM images of the aggregates showed one-dimensional structures (**Figure 6**). The use of the FF group in the CoOP sequence was for enhancing the one-dimensional aggregation; thus, the observed structures were expected. These results indicate that control over peptide aggregation is achieved by changing the hydrophobicity of amino acids in the substitution domain

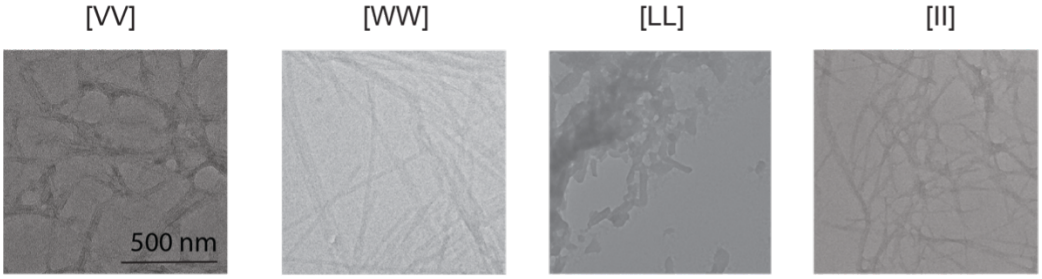


Figure 6 TEM images of [VV], [WW], [LL] and [II] peptides. Scale bar: 500 nm.

2.2.2. Cell Viability

We used the human ovarian cancer cell line OVCAR-8 as our initial model to identify the effect of the peptides on cells. All cell culture experiments were performed in an RPMI cell culture medium with 10% FBS. At 0.5 mM (i.e., above the overall CAC), the individual peptides mixed on the cells by promptly adding the first negative, then positive counterparts. The viability of the cells was measured for 6h through live-dead imaging (**Figure 7A**) Among the peptide groups studied, [AA], [VV], and [LL] did not affect cell viability in the measured time frame (**Figure 7A**). Only [WW] and [II] caused cell death compared to the control group. Because the peptides, if aggregate, form one-dimensional structures, the shape of the aggregates is not likely to be effective on the action of the peptides. [II] has the lowest CAC and highest ordered aggregation (**Figure 5B, C and D**). Additionally, the equilibrium time of [II] aggregations was the shortest among the tried groups (Table 1). These all indicate that [II] peptides have the highest affinity to each other, which creates aggregations strong and fast enough to induce cell death.

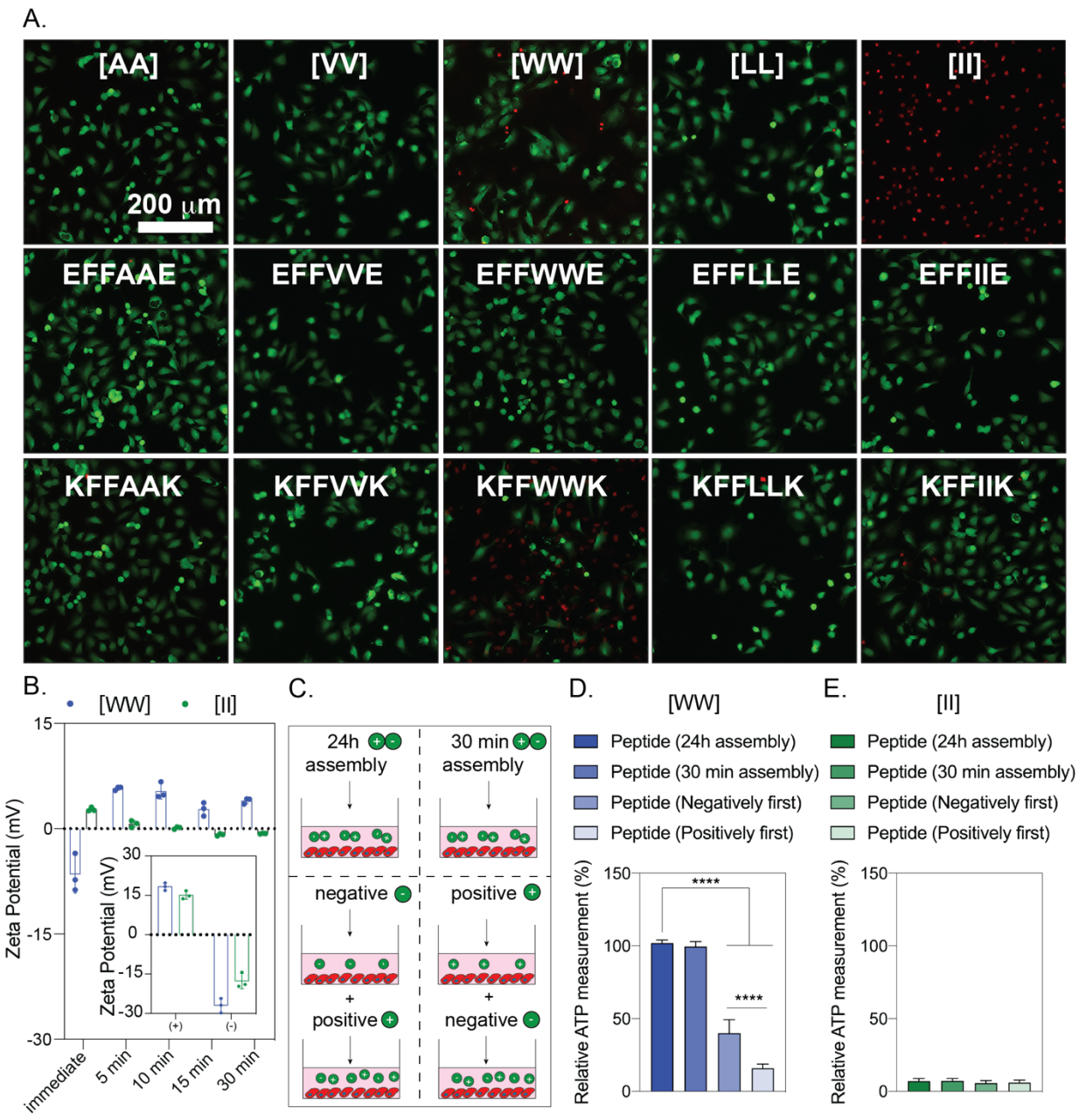


Figure 7 Cytotoxicity of peptides to OVCAR-8 cells. Negative peptides were added to the cells, followed by corresponding positive peptides. (A) Live-dead images of OVCAR-8 cells treated with peptide combinations and corresponding individual counterparts at 6h (peptide concentration is 0.5 mM) (B) Zeta potential of individual and combined peptides. (C) Illustration of peptide preparation for [WW] and [II]. The effect of peptide preparation on cell viability for [WW] (D) and

[II] (E). The scale bar is 200 μm. Data are representative of at least three experiments. Statistical analysis via one-way ANOVA test, data are mean ± SD, ****p<0.0001.

To understand the effect of peptide aggregates versus peptides alone on the cell death identified with [WW] and [II], we performed a live/dead assay with individual peptides at 0.5 mM after 6h (**Figure 7A**). Despite the dramatic cell death observed with the [II] mixture at this concentration, the individual [II] peptides did not induce cell death. Similarly, the negative [WW] (EFFWWE) peptide alone did not show any cell death, yet the positive [WW] (KFFWWK) peptide induced the cell death (as indicated by red-stained cells). Positive charged peptides containing W are promiscuous residues for membrane damaging peptides, possibly because of W's ``anchoring'' role; W is abundant in membrane proteins, particularly near the lipid–water interface[177,178]. Furthermore, as analyzed by zeta-potential, individual peptides showed the expected overall charges at pH 7.0 ((pKa of ($-COO^-$) of E is 4.25 and ($-NH^{3+}$) of K is 10.53) (**Figure 7B**). In an aqueous solution, the [II] aggregates acquire a neutral charge in 5 min, while [WW] showed a slight positive charge after 30 min, possibly due to incomplete assembly (**Figure 7B**).

Given the effects of individual [II] and [WW] on cell viability, we examined the order of addition of the peptide counterparts; first positive and then negative peptide, and vice versa (**Figure 7C**). The addition of KFFWWK first induced significantly higher cell death (****p<0.0001) compared to the initial addition of negative peptide, indicating that the cell death is due to the positive charge of KFFWWK (**Figure 7D**). Yet, any order change did not affect the membrane damage activity levels for [II] (**Figure 7E**). Moreover, mixing the peptides for 30 min or 24h before addition to the cells completely abolished the effect of [WW] (**Figure 7D**), indicating that the initial membrane damage was due to the positive charge of KFFWWK which was neutralized upon

mixing and aggregation with its counterpart (**Figure 7B**). Nevertheless, the pre-mixing did not alter the effect of [II] under these conditions (**Figure 7E**), highlighting that [II] is the only peptide pair among those studied that induces cell death through the aggregation of its charged counterparts. Although these charges help peptides find each other even in low concentrations, the electrostatic interactions do not contribute to the stability or thermodynamic assembly of the peptides, which happens only through the hydrophobic amino acids in the core of the sequence[145]. Our results show that increasing the hydrophobicity of the amino acid decreases the aggregation time, which has a direct effect on cell membrane damage. Isoleucine is the most hydrophobic canonical amino acid, and [II] peptides have the highest affinity among the studied pairs and showed the lowest CAC in the shortest aggregation equilibrium time (**Figure 5**)The affinity among [II] creates strong aggregates to induce ICD, which is the functionality that we aimed to mimic.

Synthetic peptides derived from natural proteins induce ICD through perturbation of both cell and mitochondrial membranes[179–181]. However, these peptides target Bcl-2 family proteins to create mitochondrial damage[109,182]. The oncogenic mutations in the Bcl-2 proteins and known drug resistance against therapeutics targeting them, diminishes the effectiveness of these peptides[183,184].

2.2.3. Cell Membrane rupture Through Peptide Assembly

The aggregation-induced membrane damage activity was only observed with [II]; we analyzed how it induces cell death. We used propidium iodide (PI) to understand cell membrane damage, a dye that does not permeate intact cell membranes[185]. ***Figure 8*** shows cells treated with three concentrations of [II]: 0.25 mM 0.5 mM and 1 mM for 1, 6, and 24h. Increasing the concentration

to 1 mM resulted in faster membrane damage, while decreasing the concentration to 0.25 mM (although still higher than the [II] CAC of 38 mM did not have sufficient aggregation to trigger membrane damage in this time frame. The time and concentration dependence membrane damage activity of [II] is likely to result from faster aggregation in higher concentrations. These results show that [II] induced cell death can be controlled through time and concentration. Flow cytometry results of PI uptake were correlated with the imaging analysis showing >80% cell death at 6h for 0.5 and 1 mM [II] peptide treated cells (**Figure 9A and B**). To understand the lowest [II] peptide concentration that can induce membrane damage, we treated the cells with 0.1-0.2-0.3-0.4 and 0.5mM [II] peptides. For 6 and 24h the lowest concentration resulting in membrane damage was 0.4 mM (**Figure 10**).

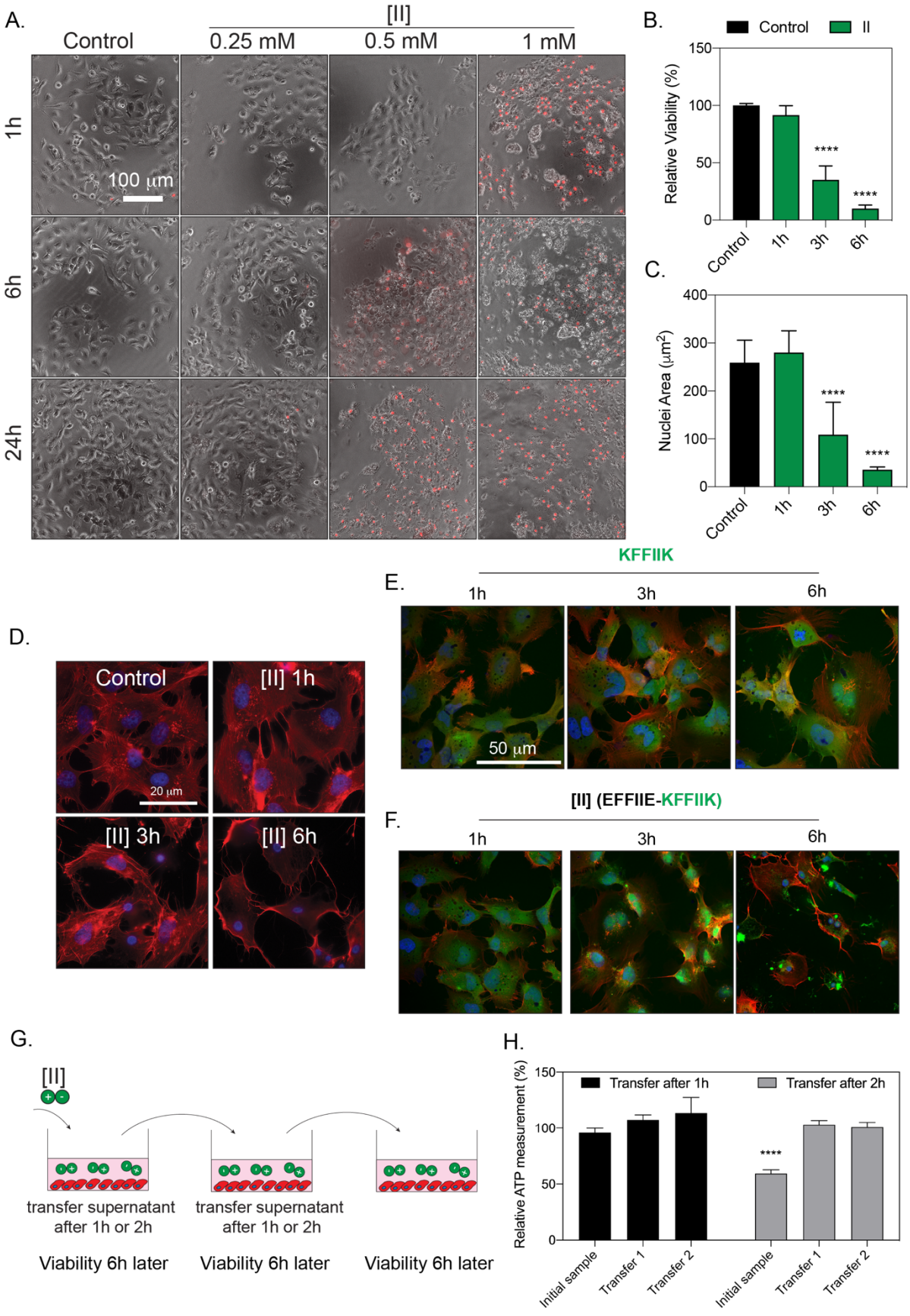

A.
[II]
Control
0.25 mM
0.5 mM
1 mM
1h
6h
24h
100 µm
B.
Control
II
Relative Viability (%)
150
100
50
0
****
****
Control
1h
3h
6h
C.
Nuclei Area (µm²)
400
300
200
100
0
****
****
Control
1h
3h
6h
D.
Control
[II] 1h
[II] 3h
[II] 6h
20 µm
E.
KFFIIK
1h
3h
6h
50 µm
F.
[II] (EFFIIE-KFFIIK)
1h
3h
6h
G.
[II]
transfer supernatant after 1h or 2h
transfer supernatant after 1h or 2h
Viability 6h later
Viability 6h later
Viability 6h later
H.
Relative ATP measurement (%)
150
100
50
0
Transfer after 1h
Transfer after 2h
****
Initial sample
Transfer 1
Transfer 2
Initial sample
Transfer 1
Transfer 2

Figure 8 [II] induces membrane rupture. (A) Time and concentration-dependent cell membrane damage of [II] were analyzed through PI uptake (scale bar is 100 μm). (B) Time-dependent viability measurement and (C) time-dependent nuclear size analysis. (D) Actin cytoskeleton staining of [II] treated OVCAR-8 cells at 1,3 and 6h, scale bar is 20 μm. (E) Internalization of FITC-KFFIIK and (F) FITC-[II] for 1, 3 and 6h, scale bar is 100 μm. (G) Experimental plan of [II] transfer and viability experiment. (H) Effect of [II] transfer on cell viability at 6h. Data are representative of at least three experiments. Statistical analysis was done with one-way ANOVA test. Data are mean ± SD, ****$p<0.0001$.

The confocal images analyses of 0.5 mM [II], which induces >85% of death in 6h (**Figure 8B**) showed cell swelling and nuclear condensation; hallmarks of necrotic cell death (**Figure 8C and D**)[186]. Aggregation was visualized by labeling the positive charged [II] (KFFIIK) peptide with FITC (green fluorescent). We monitored the internalization and aggregation of KFFIIK through fluorescence microscopy.

KFFIIK alone was internalized into the cells starting at 1h (**Figure 8E**), and cellular morphology did not change over time as KFFIIK alone does not cause cell death. When KFFIIK was introduced with its negatively charged counterpart, EFFIIE, the peptide-aggregation (more localized green KFFIIK) was apparent around and within the cells starting at 3h (**Figure 8F**). The peptide-aggregation induced nuclear area shrinking and loss of integrity of the cells (observed through the absence of actin fibers), indicating [II] aggregation-induced cell membrane damage and death.

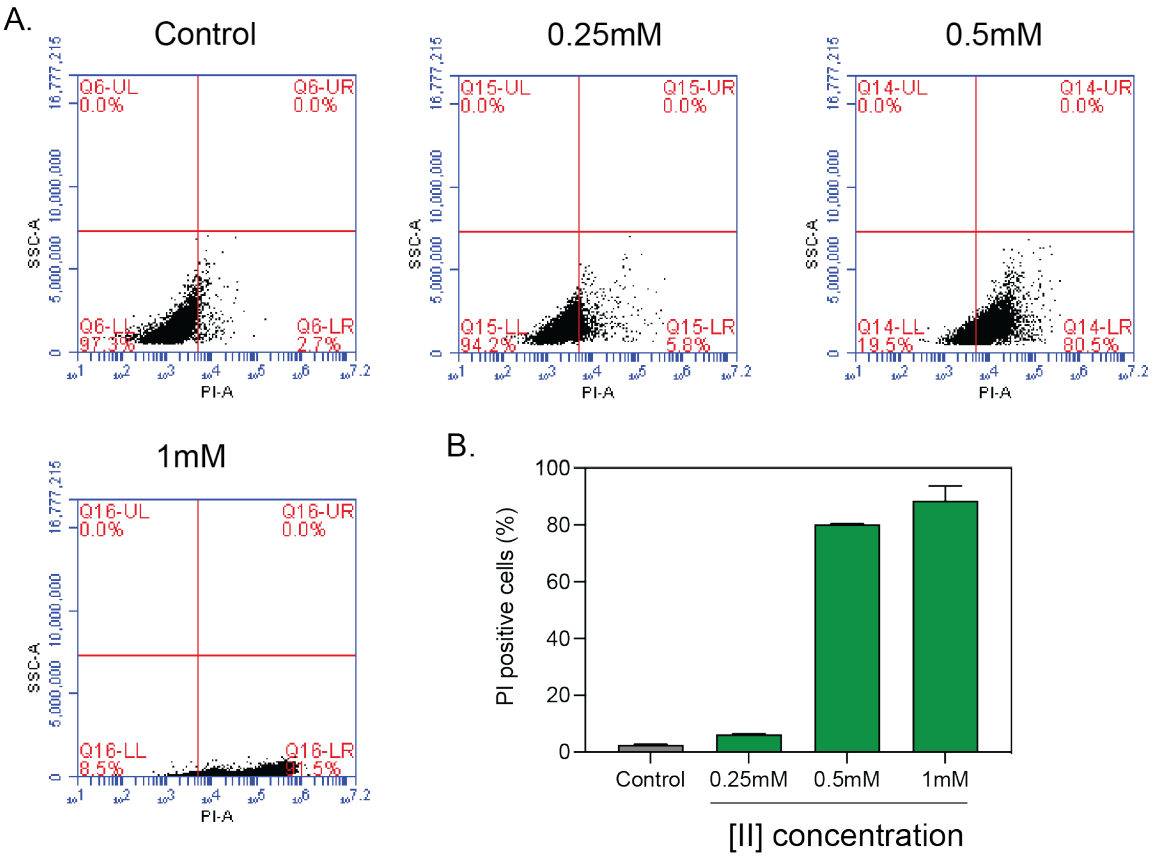


Figure 9 Propidium iodide (PI) uptake analysis by using flow cytometry. Representative histograms of untreated cells and cells treated with 0.25-0.5 and 1 mM [II] peptide for 6h (A). Percent (PI) positive cells at 6h.

Observing cell death beyond the desired area (i.e., off-site cytotoxicity) is a major obstacle for existing therapeutic applications. To estimate the off-site cytotoxicity of our approach, we incubated cells with 0.5 mM [II] for 1h or 2h, followed by the transfer of supernatant into another well with fresh cells, and measured viability after 6h (**Figure 8G**). We observed the membrane damage activity only in the initial sample after 2h (**Figure 8H**) suggesting that at this concentration, [II] does not induce cell membrane damage in 1h (in line with the viability results **Figure 8B**)Also, subsequent transfer of the supernatant of cells incubated with [II] for 1h did not

induce cell membrane damage, possibly due to aggregation having started within the cells and thus insufficient [II] transfer to the next well.

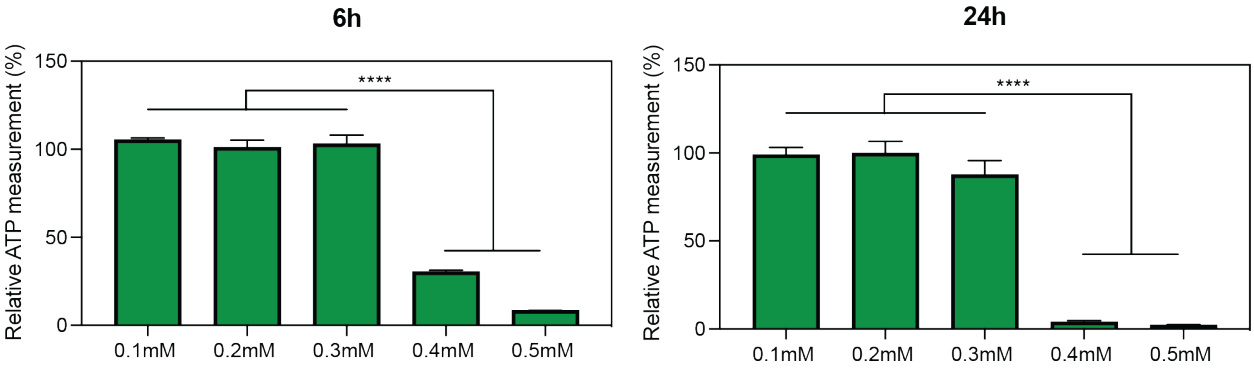


Figure 10 6h and 24h cell viability measurements of OVCAR-8 cells treated with 0.1, 0.2, 0.3, 0.4 and 0.5 mM [II] peptide. Statistical analysis was done by one-way analysis of variance (ANOVA) with Tukey's multiple-comparison test. Data shown are mean ± SD, ****p<0.0001. n=3 replicates.

2.2.4. [II] Aggregation-Induced Cell Death is Immunogenic

DAMP release through cell membrane rupture is a hallmark of ICD. We measured the release of lactate dehydrogenase (LDH), a cytoplasmic enzyme released into the extracellular matrix upon membrane damage[187]. LDH release became significant 3h after incubation with [II] (**Figure 11A**) in agreement with the reduction of cell viability (**Figure 11B**). As expected, significant DAMP release followed the cell membrane damage, such as the presence of extracellular ATP (****p<0.0001) after 3h (**Figure 11B**), correlated to the LDH release data. However, the amount of extracellular ATP is depleted in 6h due to cell death > 85% (i.e., few live cells remain to release ATP upon ICD) and rapid extracellular hydrolysis of ATP[188]. Similarly, the release of other DAMPs (specifically HMGB-1 and HSP90) was also detected in the extracellular environment of [II]

treated cells at 6h via western blotting (**Figure 11C**). Our DAMP release profile results highlight that the observed cell death is immunogenic and induced by [II] peptide pair aggregation. In other words, peptide-aggregation induced immune rupture (PAIIR) is demonstrated with the [II] pair.

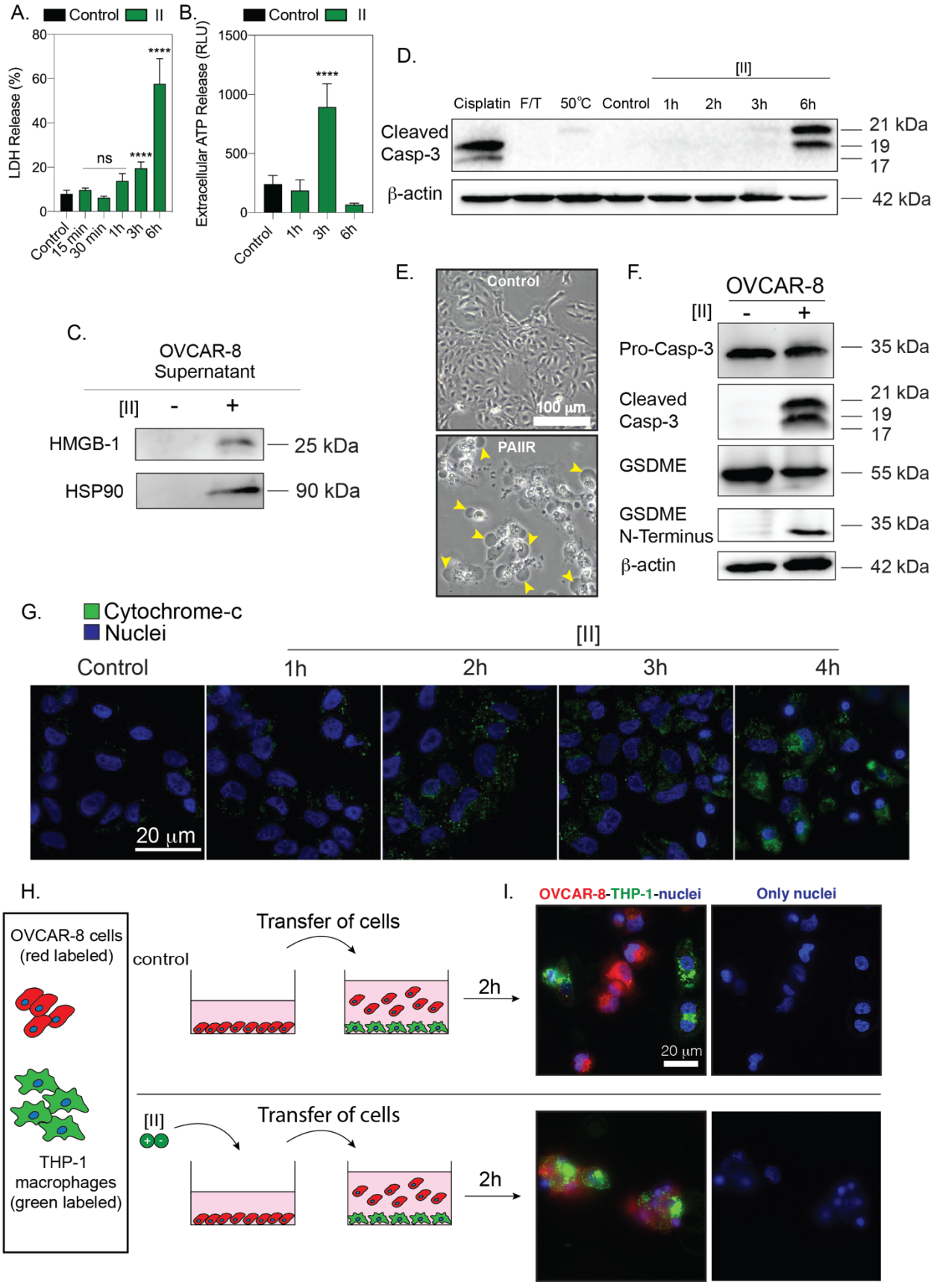

A.
Control
II
LDH Release (%)
ns
****
Control
15 min
30 min
1h
3h
6h
B.
Extracellular ATP Release (RLU)
Control
1h
3h
6h
C.
OVCAR-8
Supernatant
[II]
HMGB-1
25 kDa
HSP90
90 kDa
D.
[II]
Cisplatin
F/T
50℃
Control
1h
2h
3h
6h
Cleaved
Casp-3
β-actin
21 kDa
19
17
42 kDa
E.
Control
100 μm
PAIIR
F.
OVCAR-8
[II]
Pro-Casp-3
35 kDa
Cleaved
Casp-3
21 kDa
19
17
GSDME
55 kDa
GSDME
N-Terminus
35 kDa
β-actin
42 kDa
G.
Cytochrome-c
Nuclei
[II]
Control
1h
2h
3h
4h
20 μm
H.
OVCAR-8 cells
(red labeled)
THP-1
macrophages
(green labeled)
control
Transfer of cells
2h
[II]
Transfer of cells
2h
I.
OVCAR-8-THP-1-nuclei
Only nuclei
20 μm

Figure 11 [II] induces DAMP release and secondary pyroptosis. (A) Time-dependent LDH release. (B) Time-dependent extracellular ATP release. (C) Western blot analysis of HMGB-1 and HSP90 release at 6h. (D) Caspase-3 cleavage after treatment with Cisplatin, F/T, heat treatment and 1-2-3 and 6h of [II] treatment. (E) Phase-contrast images of control and [II] treated OVCAR-8 cells at 6h, yellow arrows indicate bubbles emerging from pyroptotic cells. (F) Caspase-3 and GSDME cleavage of OVCAR-8 cells with and without treatment with [II]. (G) Time-dependent cytochrome c release into the cytoplasm from OVCAR-8 cells. The scale bar is 100 μm. (H) Schematic illustration of the phagocytosis assay. (I) Phagocytosis of OVCAR-8 cells by THP-1 differentiated macrophages after 6h of [II] and control treatment. Data are representative of at least three experiments. Statistical analysis via one-way ANOVA test, data are mean ± SD, ****$p<0.0001$.

Regulated cell death via an inducer is concentration and time-dependent and therefore controllable. On the other hand, unregulated cell death cannot be controlled to the same extent as it mainly results from mechanical forces or temperature. The unregulated cell death releases an instantaneous burst of DAMPs, while the DAMP release from regulated cell death is prolonged. Therefore, regulated ICD is desired for a controlled immune response. Regulated necrotic cell deaths are caspase-dependent[14,189]. To identify whether [II]-induced cell death is regulated, we analyzed the cleavage of caspase-3, a known mediator of apoptosis, and GSDME mediated pyroptosis (regulated necrosis)[147,190]. We compared the caspase-3 cleavage among different cell death modalities; we used cisplatin - a known apoptosis inducer in the OVCAR-8 cell line[191]. We also used heat treatment to induce multiple cell death modalities, including necrosis, apoptosis, and necroptosis[192]. Additionally, we applied a freeze/thaw (F/T) method, a common technique to induce unregulated necrosis[193]. **Figure 11D** shows western blotting of caspase-3

cleavage upon these treatments. Cisplatin showed caspase-3 cleavage, which is expected in apoptotic cell death. Conversely, F/T did not show any caspase-3 cleavage. Observation of cleaved caspase-3 in [II] induced cell death indicates regulated necrosis (e.g., GSDME mediated pyroptosis)[194]. Indeed, pyroptosis can be identified via cleavage of caspase-3 and GSDME and a ballooning morphology of the cell membrane[42]. As cell membrane damage is already identified, we examined the morphological features of [II] treated cells and observed ballooning of the plasma membrane (**Figure 11E**), yellow arrows).

At the molecular level, cleavage of caspase-3 activates GSDME cleavage, then the N-termini of the cleaved GSDME oligomerize and induces membrane pore formation[162]. Western blot analysis showed that OVCAR-8 cells express GSDME and treatment with [II] results in its cleavage at 6h (**Figure 11F**). These results show that [II] treated cells have the morphological and molecular features of GSDME-mediated pyroptosis, a regulated ICD.

The majority of caspase activation within mammalian cells is initiated through cytochrome c, a protein normally found in mitochondria[195]. Released cytochrome c initiates the activation of caspase-3[196] and the downstream pathway of cytochrome c release is not dependent on the functions of BAX or BAK proteins[182]. Furthermore, cytoplasmic cytochrome c release has been shown to lead to the induction of GSDME-mediated pyroptosis in cells that express GSDME[42]. To understand the origin of caspase-3 cleavage upon [II] treatment, we stained cytoplasmic cytochrome c to analyze mitochondrial damage as shown before[197].

Time-dependent imaging showed that cytochrome c levels increased over time in the cytoplasm of OVCAR-8 cells (**Figure 11G**), specifically at 4h, explaining the abundance of cleaved caspase-3 at 6h (**Figure 11D**). These results show the general mechanism of PAIIR; [II] peptide directly

damages the cell membrane, as the LDH release was observed in the first 3h of the incubation along with the ATP release (**Figure 11A and B**), yet the caspase 3 cleavage was abundant after 3h (**Figure 11D**). [II] peptide induces plasma and mitochondrial membrane damage, leading to cytochrome c release into the cytoplasm; this release activates caspase-3 cleavage, and initiates GSDME-mediated pyroptosis.

ICD and DAMP release is known to enhance the phagocytosis of APCs[193]. We checked whether [II] treated cells are phagocytosed by macrophages. THP-1 differentiated macrophages are commonly utilized for in vitro phagocytosis experiments[198]. We treated red-labeled OVCAR-8 cells for 6h with [II] and co-cultured them with green-labeled THP-1 macrophages for 2h. We observed phagocytosis of [II] treated cells by the macrophages, yet control cells were not phagocytosed (**Figure 11I**).

2.2.5. Peptide Assembly Induced ICD in Different Cell Types

Induction of pyroptosis through raptinal (small drug) was shown to convert to apoptosis in the absence of GSDME, which is immunologically silent[79]. To identify whether [II] induced ICD requires GSDME expression, we tested various cell lines with different GSDME expression profiles; B16F10 and Panc02 cells lines showed no GSDME expression, while 3T3 fibroblasts had low expression levels compared to OVCAR-8 (**Figure 12A**). Incubation of 0.5 mM [II] showed a similar cell membrane rupture effect with these cell lines, as indicated by PI uptake (**Figure 12B**). [II] initiated the extracellular release of DAMPs; HMGB-1 and HSP90 in 6h (**Figure 12C**). Bubbling cell membrane structures were not observed in the cells that lacked GSDME (**Figure 12A**), suggesting that pyroptosis did not occur. These results show that [II] induced ICD is not dependent on GSDME, although it also has a GSDME-regulated secondary mechanism.

Expression of GSDME was linked to anti-tumor immunity and tumor suppression[79]. However, GSDME is expressed at low levels in most cancer types[80] due to epigenetic silencing through methylation[81].

One of the cell types we analyzed was fibroblasts, an abundant cell type in the subcutaneous layer[199]. After subcutaneous vaccination, the stimulation of DAMP release from fibroblasts would act as natural adjuvants. Therefore, we quantified the [II] induced ICD of 3T3 fibroblasts with time-dependent cell death and LDH release (**Figure 12D, E and F**), and the effect of [II] on fibroblasts was similar to that on OVCAR8.

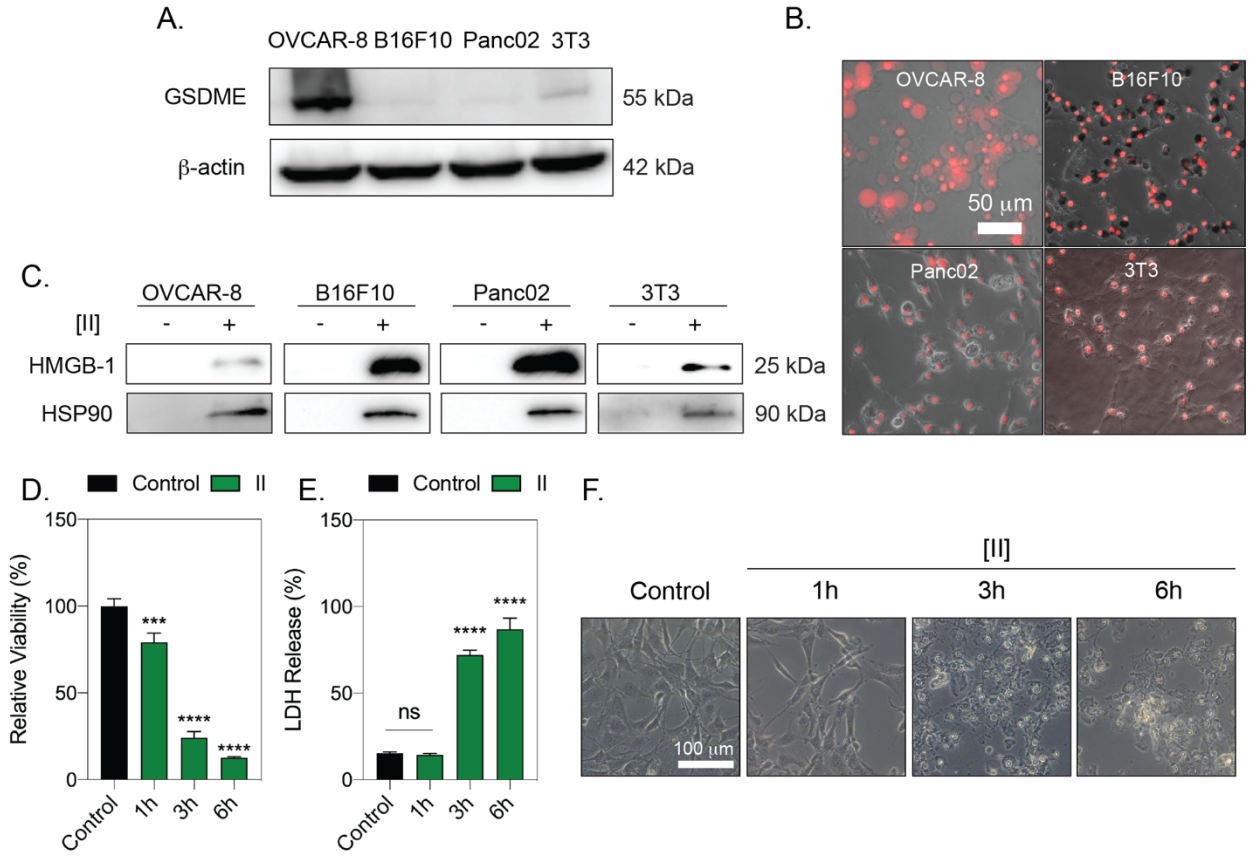


Figure 12 [II] induced membrane rupture and DAMP release is not cell type specific. (A) GSDME analysis of OVCAR-8, B16F10, Panc02 and 3T3 cells. (B) PI uptake at 6h of [II] treatment on cells. (C) HMGB-1 and HSP90 release to the supernatant (SN) at 6h. (D) Time dependent viability

measurement. (E) Time-dependent LDH release. (F) Phase-contrast images of [II] treated fibroblasts at 1, 3 and 6h. Data are representative of at least three experiments. Statistical analysis was done by one-way ANOVA test, data shown are mean ± SD, ****p<0.0001, ***p<0.001.

Observation of ICD in various cell lines makes PAIIR an excellent adjuvant candidate. Although the mechanisms of clinically available adjuvants have not been entirely elucidated, the local cell death induction is a known part of their mechanism[149]. DAMP release from local healthy cells has been shown to be the mechanism of action for commonly utilized adjuvants. MF59 stimulates ATP release from muscle cells[71] while Alum has been shown to stimulate IL-33 from alveolar epithelial cells[64].

2.2.6. [II] Induced Immune Response Enhances the Specific Antibody Formation Against Influenza Antigens

We tested the hypothesis that the DAMP release caused by [II], in the presence of HA antigen, can enhance the antibody responses to influenza HA (**Figure 13A**). Balb/c mice were immunized with PBS vehicle, recombinant HA, [II], or HA + [II]. After 60 days, mice received booster vaccines identical to the initial vaccine dose. Mice were bled at two-time time points after the primary immunization (days 14 and 28) and once after the booster vaccine (day 75). HA-specific IgG1 could not be detected following administration of PBS vehicle or [II] alone (**Figure 13B**). HA-specific IgG1 was detected and increased with time since the primary immunization and was increased over 10 fold by the booster vaccine. At each of these time points, the addition of [II] in the formulation caused a 2-4 fold and significant increase in HA-specific IgG1 titers. A similar pattern was observed for the less abundant IgG2a subclass, where [II] HA exerted a strong and

significant adjuvant effect on the HA-specific IgG2a titer (**Figure 13C**). Although the overall IgG response remained IgG1-dominated, by day 28, [II] had increased HA-specific IgG2a titers 7.3 fold and 12.4 fold by day 75. Consistent with the observation that [II] alone did not induce HA-specific IgG1 or IgG2a responses, ELISA plates were also coated with [II] (**Figure 13D**). Moreover, injection of [II] did not induce any noticeable pain in the mice throughout the vaccination.

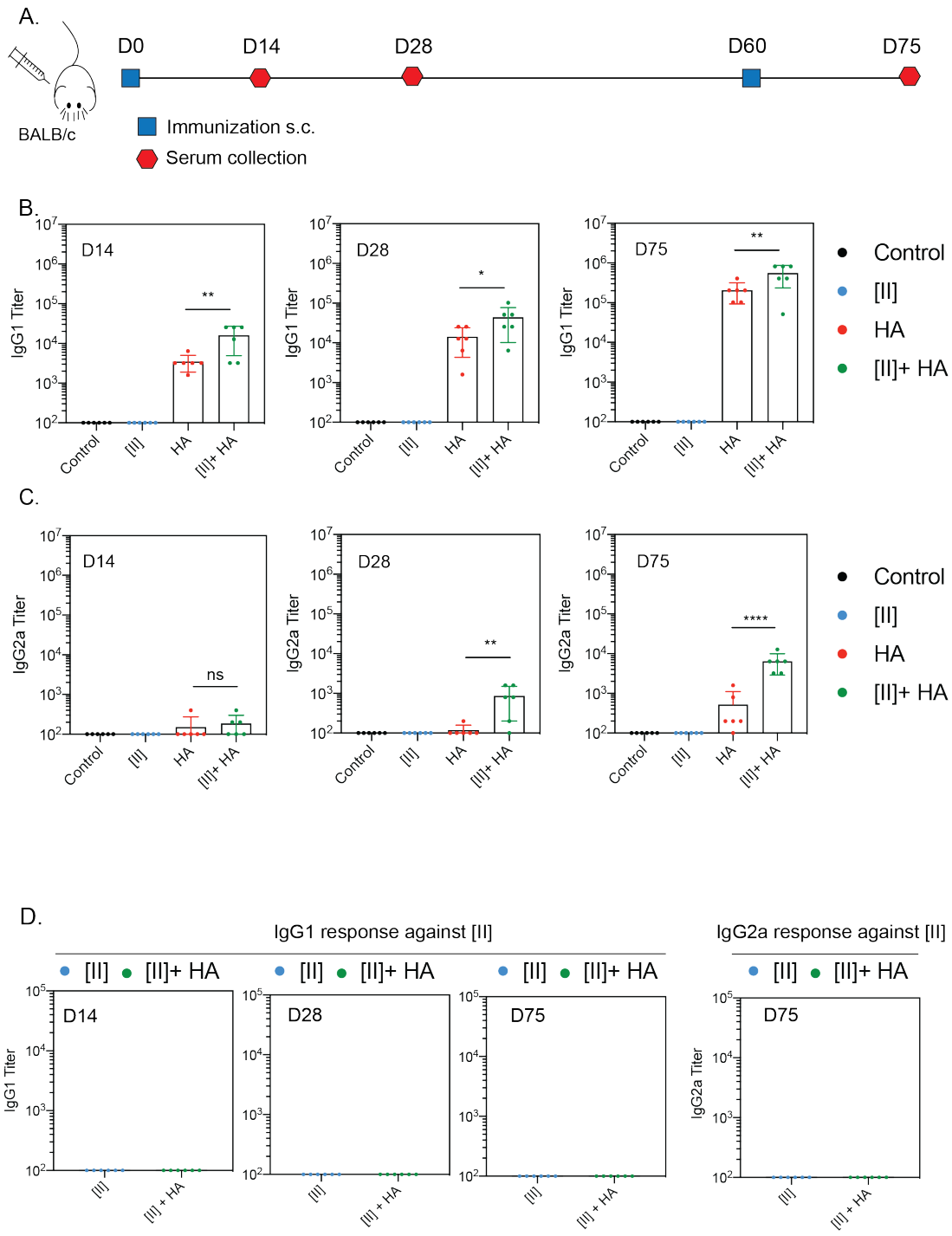


Figure 13 PAIIR induces influenza-antigen specific antibody formation. (A) Timeline and the plan of the vaccination study: BALB/c mice were vaccinated at D0 followed by a booster at D60, serum was collected at D14, 28 and 75. (B) Antigen-specific serum IgG1 titers at D14, 28 and 75. (C)

Serum IgG2a titers at D14, 28 and 75. (D) Serum IgG1 and IgG2a titers against [II] peptide at D14, D28 and D75. Statistical analysis was done by one-way analysis of variance (ANOVA) with Tukey's multiple-comparison test, data shown are mean ± SD ****p<0.0001, **p<0.01, *p<0.1 n=6 mice.

The skin where the [II] injection was performed subcutaneously did not show any external signs of inflammation (**Figure 14**). Notably, [II]-specific IgG1 and IgG2a could not be detected. These results, therefore, demonstrate that [II]-induced ICD and DAMP-release in the body can create an adjuvant effect when injected with HA. In the previous studies, IgG2a formation in mice was shown to generate higher cross-protection (heterosubtypic) against lethal challenge with different influenza virus strains[157,200,201]. Given the need for a universal influenza vaccine, any adjuvant that can boost the IgG2a response could contribute to achieving that goal. A challenge study using different influenza strains, including the heterosubtypic cross-protection and comparison of the clinical adjuvants are the next steps for PAIIR to explore its protective properties.

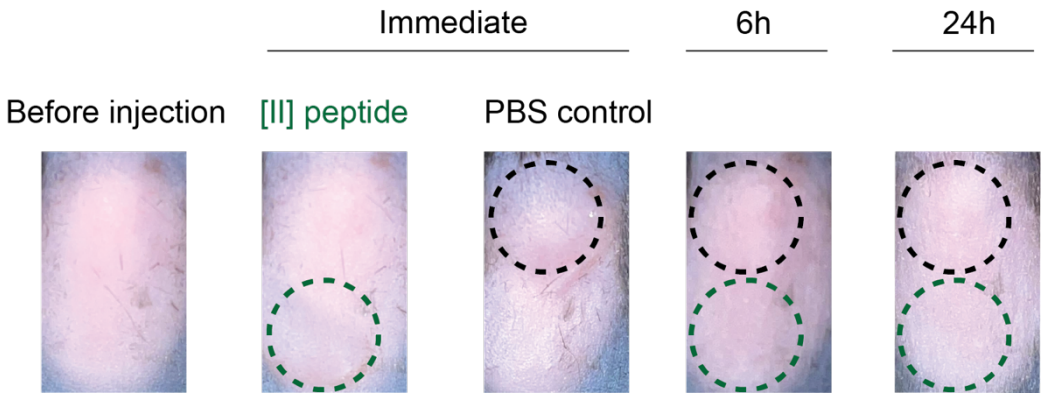


Figure 14 Effect of [II] peptide injection on skin. [II] peptide and PBS control were injected, and skin was monitored immediately after injection followed by 6 and 24h.

The lack of a [II]-specific IgG response is informative. Professional APCs express the Major Histocompatibility Complex (MHC) class II. Loading of MHC molecules with self and foreign antigen-derived peptides governs immunological tolerance and the immune response to pathogens, respectively. The peptide-binding groove of MHC-II accommodates peptides of 13-25 amino acids[202]. The B cell antigen receptor (BCR) recognizes linear and conformational epitopes consisting of peptide sequences or other macromolecules. Because [II] is a peptide-based adjuvant, the possibility of MHC-II presentation or recognition by the BCR was considered. Our results showing no antibody response against [II] itself indicate that it is unlikely that the hexameric [II] peptide can bind MHC-II or be recognized by the BCR.

2.3. Conclusions

Interest in peptide-based materials has flourished in health, energy, materials science, and national security[169]. By advancing the discovery of peptide domains with unique intermolecular interactions, the design of peptides with desired properties in appropriate conditions can be achievable. Inspired by the mechanism of natural membrane rupturing proteins that aggregate and induce ICD, in this study, we designed a new peptide-based tool, [II], via the CoOP strategy. Understanding and controlling ICD is an essential tool that plays a paramount role in advancing cancer immunotherapy and vaccine development. We demonstrated the controlled ICD mechanism of [II] in vitro with various cell lines and observed broadened IgG profiles: IgG1 and IgG2a in mice vaccinated with the [II] and influenza HA subunit. Peptide-aggregate induced immune rupture (PAIIR) via [II] pairs ("pa[II]r") has tremendous potential to advance healthcare and basic science applications based on immune system modulation.

2.4. Experimental Section

2.4.1. Statistical Analysis

Pre-processing of data did not include outlier exclusion. Data were analyzed by using GraphPad Prism Version 9.3.1. Figure preparation was done by using Adobe Illustrator 2021. **Figure 7**D and E, **Figure 8**B and H and **Figure 12**D were normalized to the mean of untreated control. **Figure 11**A and **Figure 12**E were normalized to the mean of Triton-X treated condition for LDH release (Maximum LDH release). At least three biological replicates were performed for in vitro studies, and n=6 per group was performed for the vaccination study. All data are presented as mean ± standard deviation (SD). Statistical analysis was done by one-way analysis of variance (ANOVA) with Tukey's multiple-comparison test. **** $p<0.0001$, *** $p<0.001$, ** $p<0.01$, * $p<0.1$.

2.4.2. Materials

9-fluorenylmethoxycarbonyl (Fmoc) protected amino acids, [4-[a-(2',4'-dimethoxyphenyl) Fmoc aminomethyl] phenoxy] acetamidonorleucyl-MBHA resin (Rink amide MBHA resin), Oxyma, N,N'-Diisopropylcarbodiimide (DIC), Trifluoroacetic acid (TFA), piperidine, dimethylformamide (DMF), dichloromethane (DCM) were purchased from Gyros Protein Technologies. Triisopropylsilane, Acetic anhydride, Congo Red dye and pyrene were purchased from Sigma-Aldrich. Deionized water (resistance of 18.2 MΩ.cm) was used during the experiments.

2.4.3. Cell Culture and Reagents

Epithelial ovarian cancer cell line OVCAR-8 (NCI-Vial Designation 0507715), B16-F10, Panc02, 3T3 and THP-1 cell lines were cultured in a humidified incubator at 37 ºC supplied with 5% CO_2. B16-F10 and Panc02 cell lines were gifts from Dr. Wei R. Chen, University of Oklahoma. THP-1 cell line was gift from Dr. Stefan Wilhelm, University of Oklahoma.

OVCAR-8, THP-1, Panc02 cells a were cultured in Roswell Park Memorial Institute (RPMI) media (SIGMA R8758) and B16F10 and 3T3 cells were cultured in Dulbecco's Modified Eagle Medium (DMEM) (Sigma, D6429), supplemented with 10% FBS (Hyclone SH30910.03) and 1% antibiotics; penicillin (100 U/mL), and streptomycin (100 mg/mL) (Thermo Fisher 15240062) according to the manufacturer's instructions. T75 flasks (TPP 90076) were used to culture cells and cells were passaged upon 85% confluency by using trypsin (Sigma 59418C). The media was changed every 2 days.

2.4.4. Synthesis and Characterization of FF Peptides

FF peptides (KFFAAK, EFFAAE, KFFWWK, EFFWWE, KFFIIK, and EFFIIE) were purchased from Biomatik (Biomatik Corporation, Canada) with higher than 95\% purity. EFFVVE, EFFLLE, KFFVVK and EFFVVE peptides were synthesized via solid-phase peptide synthesis with PreludeX automatic peptide synthesizer (Protein Technologies, Inc., Tucson, AZ). Peptides were prepared on a 0.2 scale by repeated amino acid couplings using Fmoc protected amino acid (3 eq.), DIC (7.5 eq.) and Oxyma (7.5 eq.). BHA Rink Amide resin was used as solid support to construct the peptides. Fmoc protected amino acids except the final residue were removed through treatment with 20% piperidine/DMF solution for 10 min (twice) at 50 °C. Cleavage of the peptides from resin and deprotection of acid labile protected amino acids were carried out with a mixture of TFA/TIS/water in a ratio of 95:2.5:2.5 for 2.5 h. Excess TFA and organic solvents were removed by solvent evaporator and the remaining peptide was precipitated using diethyl ether at −20 °C overnight. The centrifuged white peptide residue was dissolved in water and frozen at -80 °C overnight, and then lyophilized (Labconco Freezone, 12 L) for one or two days. Peptides were purified with preparative HPLC (Agilent 1260) and identified by Shimadzu LCMS-2020. Agilent

ZORBAX 300 SB-C18 (9.4 x 250 mm) and Alltech Pro-sphere HP C4 300A 5u (250 mm x 4.6 mm) with a mobile phase of water/acetonitrile mixture (0.1% am-monium hydroxide) used for negatively charged peptides; water/acetonitrile mixture (0.1% formic acid) was used for positively charged peptides. All peptides were tested with a purity >95%. HPLC run started with 100% water for 3 min, followed by a gradient increase in acetonitrile from 0% to 60% over 30 min, followed by 100% acetonitrile for 3 min, and finally 100% water for 3 min. The flow rate is 1.5 mL/min, and the injection volume is 10 mL.

2.4.5. Peptide Aggregation Analysis

DPH assay was performed to understand the CAC. Peptides (except [AA]) were prepared in PBS starting from a concentration of 500 μM to 3.9 μM with serial dilution. [AA] was prepared from 10 mM to 15.6 mM to check the aggregation behavior even in higher concentrations. First, negatively charged peptide (48 μL) was put to the black 96 well- plate, then 4 μL (from 4 mM in PBS) DPH was added, and finally, positively charged peptide (48 μL) was added to each well. The solutions were incubated at 37 °C for an hour. After the incubation, fluorescence intensity was collected immediately with Ex:360±40 nm, Em: 460±40 nm with BioTek Neo2SM microplate reader. We performed a Congo Red assay to visualize aggregations deposited on the well plate. Peptides having 0.5 mM concentration and equal volume (48 mL each) were prepared in PBS. Then first, negatively charged peptide was put to 96 well-plate. Congo red having a final concentration of 20 mM (4 mL), was added, followed by the addition of a positively charged peptide (48 μL each). Brightfield images were taken immediately with Keyence bz-x710 microscope at defined time points. Finally, ThT assay was performed for aggregation kinetics analysis. Peptides were prepared with the same method as the Congo Red assay, but the total

peptide volume was adjusted to 196 μL. Final ThT concentration in peptide solution is 10 mM. Fluorescence measurements were taken immediately after putting positively charged peptide with Ex: 440±10 nm, Em: 480±10 nm.

2.4.6. TEM Analysis

Peptide samples were prepared from 10 mM stock solutions (incubated for 24h) of co-assembled samples to 0.02 mM with water. Then, 10 mL of diluted peptide samples were dropped onto the TEM grid (Ted Pella, Catalog number:01813-F) and incubated for 10 min. Then, samples were taken with a pipette, negatively stained with 2\% uranyl acetate and imaged using JEOL 2010F Field Emission Transmission Electron Microscope.

2.4.7. Peptide Treatment and Viability Experiments

Positively and negatively charged self-assembling peptides were mixed 30 min prior to experiment except where otherwise stated. The viability of the cell lines was measured by using CellTiter-Glo 2.0 Reagent (Promega G9248). The luminescent signal was measured in accordance with the manufacturer's instructions. Measurements were carried out with BioTek Neo2SM microplate reader and relative viability was calculated. Live-Dead assay was carried out using Viability/Cytotoxicity Assay kit (BIOTIUM 30002). After peptide treatment, cells were treated with calcein and ethidium homodimer in accordance with the manufacturer's instructions. Fluorescent images were taken by using Keyence bz-x710 microscope.

2.4.8. Induction of Different Cell Death Modalities

OVCAR-8 cells were treated with 50 μM cisplatin for 24h to induce apoptosis. T75 flask containing OVCAR-8 cells were incubated in a 50 °C water bath for 10 minutes followed by a 24h recovery

period for heat-induced cytotoxicity. Three cycles of 3 min liquid nitrogen followed by 5 min of 37 °C incubation is used to induce F/T.

2.4.9. Protein Extraction and Quantification

Lysate proteins: RIPA lysis and extraction buffer (Thermo Fisher Scientific 89900) supplemented with halt protease & phosphatase inhibitor cocktail (Thermo Fisher Scientific 78440) is used to obtain lysate proteins.

Supernatant proteins: Acetone precipitation is used for supernatant protein isolation. Briefly, ice-cold acetone was added to supernatants (4:1, v:v), incubated at -20 °C for 60 min and centrifuged at 10,000 g for 10 min. Acetone was removed and RIPA buffer was used to resuspend the proteins. Cell lysates were incubated for 15 min on ice and centrifuged at 14,000 g for 15 min at 4 °C, and supernatants were collected according to the manufacturer's instructions. BCA protein assay kit (Thermo Fisher Scientific 23225) was used to quantify protein concentrations by measuring the absorbance at 562 nm in accordance with the manufacturer's instructions.

2.4.10. Immunoblotting Reagents

Acrylamide/Bis-acrylamide, 30% solution (Sigma A3699), 1.5 M Tris-HCl, pH 8.8 (Teknova T1588), Tris HCl Buffer 0.5 M solution, sterile pH 6.8 (Bio Basic SD8122), Ammonium persulfate (Sigma A3678), UltraPure 10% SDS (Invitrogen 15553-027), TEMED (Thermo Fisher Scientific 17919), Dithiothreitol (DTT) (BIO-RAD 1610610) Tris Base (Fisher Bioreagents BP152), Glycine (Fisher Bioreagents BP381), 4x Laemmli sample buffer (BIO-RAD 1610747), TWEEN 20 (Sigma P9416), Mini Trans-Blot filter paper (BIO-RAD 1703932), Nitrocellulose Membranes 0.45 μm (BIO-RAD 1620115), Western Blotting Luminol Reagent (Santa Cruz sc-2048). Antibodies; cleaved caspase-3 (Cell Signaling, 9664S), caspase-3 (Santa Cruz, sc-7272). GSDME (Abcam, ab215191), β-actin-

HRP (Santa Cruz, sc-47778), HMGB-1-HRP (BioLegend, 651411), HSP90 (Santa Cruz, sc-13119), Goat anti-Rabbit IgG Secondary Antibody (Thermo Fisher Scientific, 31460), Goat anti-Mouse IgG (Thermo Fisher Scientific, G-21040).

2.4.11. Procedure

Protein samples were diluted in Laemmli buffer and boiled for 5 min at 96 °C. Proteins were then separated by sodium dodecyl sulfate-polyacrylamide gel electrophoresis (SDS-PAGE) gels (8.5% and 15%) and transferred to nitrocellulose membranes. After transfer, the membranes were blocked in 5% milk in Tris Buffered Saline with 0.1% Tween 20 (TBST) or in 5% BSA for phosphorylated antibodies. Blots were then incubated with primary antibodies overnight. The next day blots were washed with TBST and incubated with HRP conjugated secondary antibodies. Lastly, western blotting luminol reagent solution was added on top of the membranes, and chemiluminescence signal was detected by Azure c600 Imaging Biosystems.

2.4.12. LDH Assay

LDH release is measured by Cytoscan-LDH Cytotoxicity Assay (Cat# 786-210). Briefly, media from treated and untreated cells were collected at indicated time points, mixed with reaction mixture, and incubated at room temperature. The reaction was stopped using stop solution, and absorbance was measured at 490 nm, and 680 nm. Triton-X treatment is used as a 100% LDH release positive control. Lastly, absorbance values at 680 nm (background signal) were subtracted from absorbance values at 490 nm and relative LDH release was calculated based on the positive control LDH release.

2.4.13. Flow Cytometry

Cells were treated with either 0.25-0.5 or 1 mM [II] peptide for 6h and then stained with propidium iodide (Invitrogen, V13242) and analyzed by using BD Accuri C6 flow cytometry. Representative plots in the supporting information show PI-positive populations. Percent (%) PI-positive populations were plotted.

2.4.14. Immunocytochemistry

Phalloidin staining: OVCAR-8 cells were seeded on glass coverslips in a 24 well plate. Cells were treated with [II] for 1-3 and 6h. After each treatment period, cells were washed with 1X PBS and fixed with 4% PFA for 20 min, then, stained for 30 min with Phalloidin-iFluor 555 (Abcam ab176756) in 1% BSA. After the staining coverslips were mounted in ProLong™ Glass Antifade Mountant with NucBlue™ Stain (Thermo Fisher P36981) and stored in the dark until imaging.

2.4.15. Cytochrome c Staining

OVCAR-8 cells were seeded on glass coverslips in a 24 well plate. Cells were treated with [II] for 1-2-3 and 4h. After each treatment period, cells were washed with 1X PBS and fixed with 4% PFA for 20 min. Then cell membranes were permeabilized by using Digitonin (0.002% in PBS) for 10 min on ice, blocked with 3% BSA in PBS, and stained with cytochrome-c antibody in 1% overnight. The next day, samples were washed 3 times with PBS and incubated for 1 h at room temperature with Donkey Anti-Mouse IgG NorthernLights™ NL493-conjugated Antibody (NL009) in 1% BSA. Wells washed with 1% BSA and coverslips were mounted in ProLong™ Glass Antifade Mountant with NucBlue™ Stain (Thermo Fisher P36981) and stored in the dark until imaging.

2.4.16. THP-1 Differentiation

THP-1 monocytes were differentiated in the presence of 200 ng/mL phorbol 12-myristate-13-acetate (PMA) for 2 days. Then macrophages were incubated in serum-free RPMI medium for one day prior to co-culture studies. Prior to the co-culture experiment, OVCAR-8 cells were labeled with CellTracker Red CMTPX (Invitrogen, C34552) and THP-1 differentiated macrophages were labeled with Wheat Germ Agglutinin (WGA-488) (Biotium, 29022-1). 0.5 mM [II] treated or untreated cells were transferred onto differentiated and 24h rested macrophages in a ratio of 1:1. Briefly 20.000 treated or untreated OVCAR-8 cells were transferred to 20.000 THP-1 differentiated macrophages and co-cultured for 2h. Then, samples were fixed with 4% PFA, washed with PBS and mounted in ProLongTM Glass Antifade Mountant with NucBlueTM Stain (Thermo Fisher Scientific, P36981) and stored in the dark until imaging.

2.4.17. Ethics

The study was carried out accordingly with the recommendations of Guide for the Care and Use of Laboratory Animals from the National Institute of Health. Animal procedures were approved by the OU Health Sciences Center (OUHSC) Institutional Animal Care and Use Committee (protocol number 20-059-CHI).

2.4.18. Immunization and Sera Collection

Balb/c mice (n=6) were immunized subcutaneously with 5 mg of HA antigens, 0.5 mM [II] and their combination. Booster was done at D60, and sera were collected at D14, D28 and D75. 4 different influenza antigens; Recombinant HA protein from fluA/Brisbane/59/2007 (H1N1) (NR-28607), HA from influenza A/New Caledonia/20/99 (H1N1) (NR-48873), HA Protein from flu Virus A/St. Petersburg/100/2011 (H1N1) (NR-34588) and Recombinant HA protein from flu

A/California/04/2009 (H1N1) (NR-15749) were obtained from BEI Resources. Peptides are mixed for 30 min as explained in the manuscript and mixed with the antigens at room temperature to formulate the vaccines before immunizations.

2.4.19. ELISA

To measure antigen-specific antibody responses, enzyme-linked immunosorbent assay (ELISA) Nunc MaxiSorp™ flat-bottom plates (Invitrogen 44-2404-21) were coated with 2.5 mg/mL with the mixture of four antigens in phosphate coating buffer (0.1 M Na2HPO4 in deionized water, pH 9.0) overnight at 4 °C. Next day, plates were blocked with 1% bovine serum albumin in phosphate buffered saline-Tween (1X PBS, 0.05% Tween) for 2h at room temperature. Plates were then washed 4x with PBS-T and incubated overnight at 4 °C with serially diluted sera collected from mice in PBS-T. The next day, wells were washed 4x with PBS-T and incubated for 1h at room temperature either with HRP-IgG1 (SouthernBiotech 1070-05) (1:4,000) or HRP-IgG2a (SouthernBiotech 1080-05) (1:4000). Wells were subsequently washed 4x with PBS-T and developed with 2,2'-azinobis (3-ethylbenzthiazolinesulfonic acid) (ABTS) (VWR 95059-146) substrate for 5 min at room temperature. At the end of the incubation, the reaction was stopped with 10% SDS solution. Absorbance was measured at 405 nm to determine endpoint antibody titers.

Chapter 3: Controllable Peptide Aggregation Induced Immunogenic Cell Death

This section is adapted from the following publication:

Seren Hamsici, Gokhan Gunay, Handan Acar, "Controllable membrane damage by tunable peptide aggregation with albumin." *AIChE Journal* (2022): e17893

3.1. Introduction

Most proteins and peptides (if not all) aggregate into amyloids, cross β -sheet fibrillar structures linked to numerous diseases, such as Alzheimer's and Parkinson's[203,204]. In Alzheimer's disease, although for many decades the accumulation of amyloid plaques was associated with the pathology of the disease, increasing evidence suggests that the misfolded protein aggregates, oligomers, are soluble and form in the process of fibrillization, are the leading cause of the toxicity[205–208]. Part of their toxicity process occurs through the interactions of oligomers of Aβ or α-synuclein with the lipid membranes of cells, which initiates damage[209,210]. The membrane damage often induces immunogenic cell death and inflammation[120,211,212]. The aggregation and oligomer formation process is complex because of the convoluted conditions in the body. The dynamic conditions create transient heterogeneous misfolding of oligomers and make the molecular level of understanding, quantifying, and correlating the aggregation mechanism and toxicity; thus the development of target drug can be challenging[208,213]. Therefore, a minimalist and simplified synthetic model that mimics the structure, aggregation, and function of amyloids can serve as a powerful tool for studying their aggregation mechanism.

The molecular events that occur during the formation of small aggregations of proteins and peptides (lag phase) are in a complex environment. Studies with the extracted proteins in an

isolated system may not provide an adequate understanding of the pathophysiology of the disease. Yet, studies in biological fluids create huge complexity. Indeed, the amyloidogenic proteins' kinetics and free energy landscape in the initial aggregation phase are largely unknown and have been studied with variations of new experimental and computational approaches[214–217]. A combination of these methodologies establishes strategies for a more accurate understanding of the aggregation process. Such a combination can be possible with molecular tools that have similar behaviors and biological functions in experimental conditions as amyloid-like proteins and are simple enough for computational simulations[145].

CoOP is a minimalist strategy enabling the study of intermolecular interactions' role in peptide aggregation[145]. CoOPs are designed to assemble into amyloid fibrils. Among the studied peptide sequences, the oppositely charged pair, KFFIIK and EFFIIE (the pair will be shown hereafter as [II]) led to the most ordered amyloid-like β-sheet assembly. On the cell membrane, [II] peptide aggregation causes immunogenic rupture (PAIIR), which starts immunogenic cell death (ICD) and results in the release of damage-associated molecular patterns (DAMPs), which act as an immunostimulatory agent[218]. PAIIR induces secondary pyroptosis, a programmed ICD, and a common feature of amyloid-inducing cell death as in Alzheimer's and Parkinson's diseases[129,219]. PAIIR is a simplified peptide-based tool designed to mimic the function instead of the sequence of a protein; thus, there is no natural ortholog of [II].

Albumin is abundant in the human body, flexible, and mostly hydrophobic; thus, it has a high non-specific binding capacity[220]. It is known that albumin impedes the fibrillization of amyloids and increases the soluble misfolded oligomers of higher toxicity[221–223]. Akin to amyloid, co-aggregation with albumin creates a soluble oligomeric form of [II] that is more toxic than its

fibril form. This study shows control over the aggregation kinetics and mechanism of [II] via albumin. The simplicity of [II] outlines the detailed characterization of aggregates and their interactions with the lipid membranes. The lipid membrane interaction is shown with liposomes and fluorescent tagged peptides. The soluble form of peptides misfolded with albumin integrates into the lipid membrane of liposomes, while the ordered fibril structures do not. The kinetics of the aggregations are studied with spectroscopic methods with fluorescent probes. The morphology of misfolded oligomeric to ordered fibrillar structures is analyzed by dynamic light scattering (DLS) and atomic force microscopy (AFM). The oligomeric form of [II] misfolded with albumin results in membrane damage and cellular cytotoxicity, whereas the fibrillar [II] without albumin does not. This pattern parallels membrane localization and is also observed in cellular cytotoxicity. By delaying the formation of thermodynamically favorable ordered fibrils via albumin or simply introducing the counterparts in different time points, the soluble free peptides can localize into the membrane before they come together. Lastly, the mechanical cell stress induced by [II] is identified through the phosphorylation of yes-associated protein (YAP) and eukaryotic initiation factor 2 alpha (eIF2α), similar to the mechanism of Aβ cytotoxicity. Importantly, we identified these stress markers in the cells treated with misfolded oligomers, not with ordered amyloid fibrillar form of [II]. Overall, [II] offers a simplistic tool for investigating the effects of physical and biological processes in experiments to understand the aggregation mechanism and function of pathological proteins with amyloid-like structures.

3.2. Results and Discussion

3.2.1. [II] aggregation kinetics depend on albumin concentration

The oligomeric form of [II] with increasing amounts of albumin was visualized through AFM imaging. Lowering the amount of albumin resulted in increased fibrillar structures, while increasing the amount of albumin to 0.2% and 2% resulted in the formation of oligomer like structures (**Figure 15**).

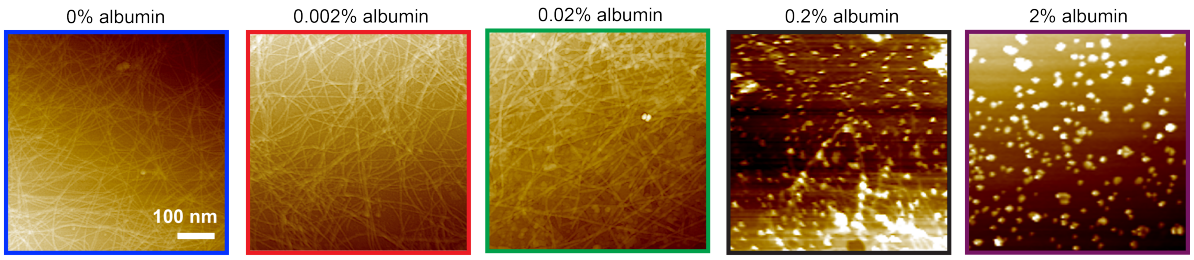


Figure 15 Aggregation kinetics depend on albumin concentration. AFM images of [II]-albumin structures (Scale bar = 100 nm).

3.2.2. [II] aggregation induces cell stress

The cell plasma membrane senses external stimuli to adapt to changes through intracellular signaling. One pathway responding against various external stimuli such as mechanical stress is the Hippo pathway. Aβ 1-42- mediated neurodegeneration involves the activation of the Hippo pathway[125]. One of the central proteins within the Hippo pathway is YAP. YAP is a transcription factor found in the nucleus in active form and gets inactivated when translocated to the cytoplasm. We treated the cells to analyze the effect of [II] aggregation on YAP localization. At the early time points, 30 min, YAP localized in the cytoplasm (**Figure 16**A). More specifically, cytoplasmic localization of YAP is mediated by its phosphorylation (Serine 127 (S127)), leading to its inactivation[126] and degradation[127]. Upon administration of [II] with 0.2 w% albumin, YAP phosphorylation in the cytoplasm can be observed green at 30 min and 1h **(Figure**

16B, Figure 17**)**. However, after 1h, phosphorylated YAP in the cytoplasm starts to degrade, which is parallel with YAP localization to the cytoplasm at early time points (30 min). Western blot results also confirmed the phosphorylation of YAP and degradation **(Figure 16C)**. Together these results show that [II] aggregation is inducing cytoplasmic localization of YAP through its phosphorylation, thus related to the mechanical stress on the cell membrane.

eIF2α is another factor integrated into the stress response to external stimuli. Under cell stress, eIF2α gets phosphorylated and initiates the activation of genes responsible for stress response. Phosphorylation of eIF2α is a consistent marker in various neurodegenerative diseases,[224] including AD[225]. Histological analysis on AD patients showed elevated phosphorylation of eIF2α[123]. Moreover, in in vitro studies, Aβ 1-42 was shown to induce eIF2α phosphorylation in human neuroblastoma cells[122]. We analyzed eIF2α phosphorylation for 0.5mM [II] in 0.2w% albumin and 0.5mM [II] in 0% albumin (non-membrane damaging condition). [II] aggregation-induced eIF2α phosphorylation at 1h **(Figure 16C)** followed by rapid degradation due to proteasome activity reported previously[226].

Phosphorylation of eIF2α and its downstream effect on CRT cell surface localization are identified as hallmarks of ICD[54]. Cell membrane-localized CRT contributes to the immunogenicity of dying cancer cells, serving as an "eat me" signal to facilitate phagocytosis[22,86]. We previously showed that [II] aggregation-induced cell death is ICD through the release of DAMPs in multiple cell lines[218]. Given that eIF2α phosphorylation results in CRT surface localization, we identified the localization of CRT within the cells incubated with [II]. CRT was observed only intracellularly in control cells and cells treated with 0.5mM [II] in 0% albumin. However, CRT localized to the cell membrane starting at 2h in cells treated with 0.5mM [II] in 0.2 w% albumin **(Figure 16D,**

Figure 18). Moreover, membrane CRT fluorescent intensity was increased upon [II] aggregation **(Figure 19)**. These results show that [II] aggregation-induced cell death involves the phosphorylation of eIF2α, followed by CRT surface localization, indicating that the observed ICD is due to the stress on the cell membrane with [II] aggregation.

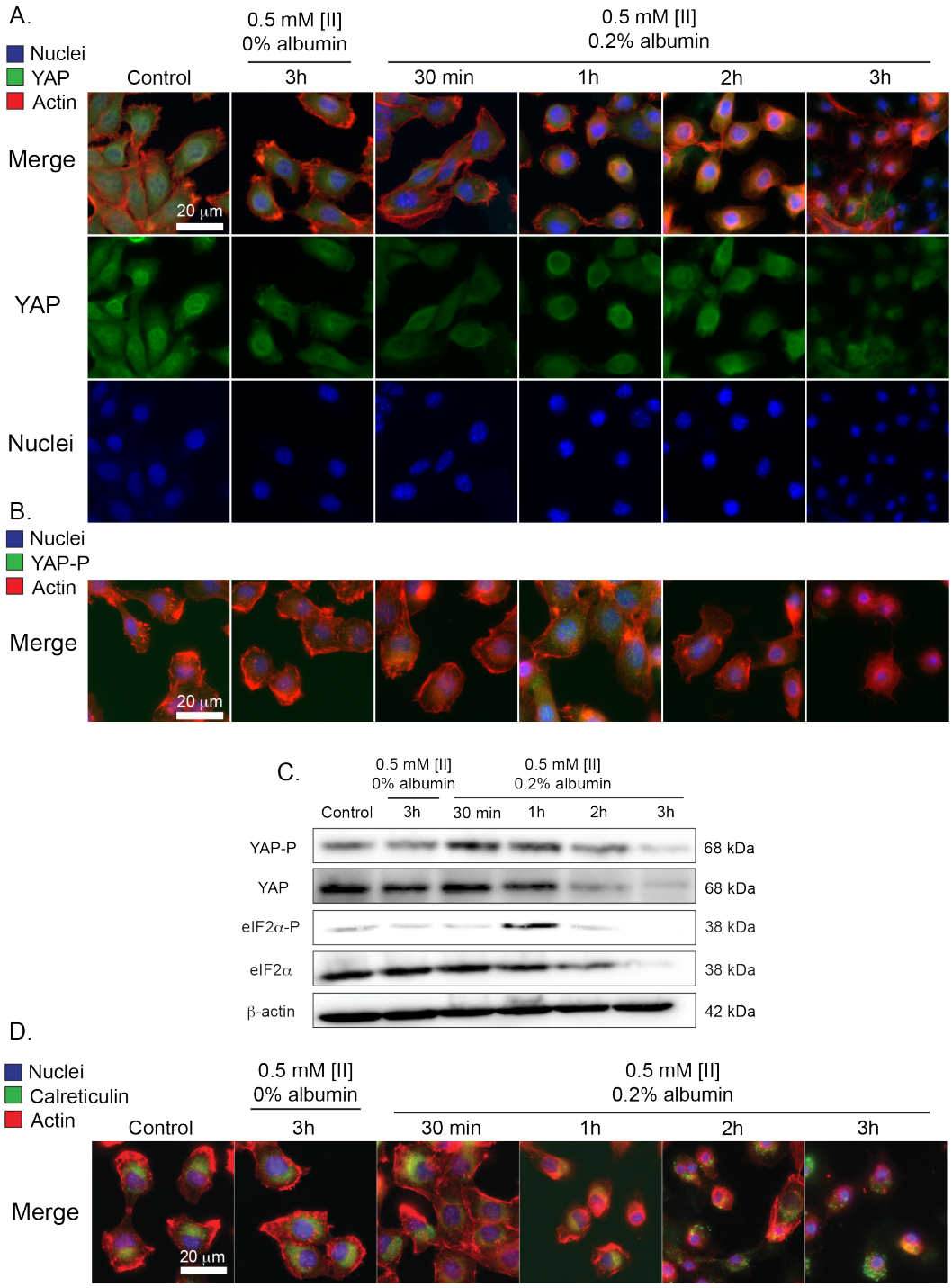


Figure 16 [II] aggregation on the cell membrane induces cell stress (A) Immunocytochemistry of YAP localization (YAP = green, Actin = red, Nuclei = blue) (B) and phosphorylation based on aggregation (YAP-P = green). (C) Western blot analysis of YAP, YAP phosphorylation, eIF2α, and eIF2α phosphorylation in different time points, β -actin was used as an internal loading control.

(D) Immunocytochemistry of CRT cell surface localization (CRT = green, Actin = red, Nuclei = blue). Scale bars = 20 µm

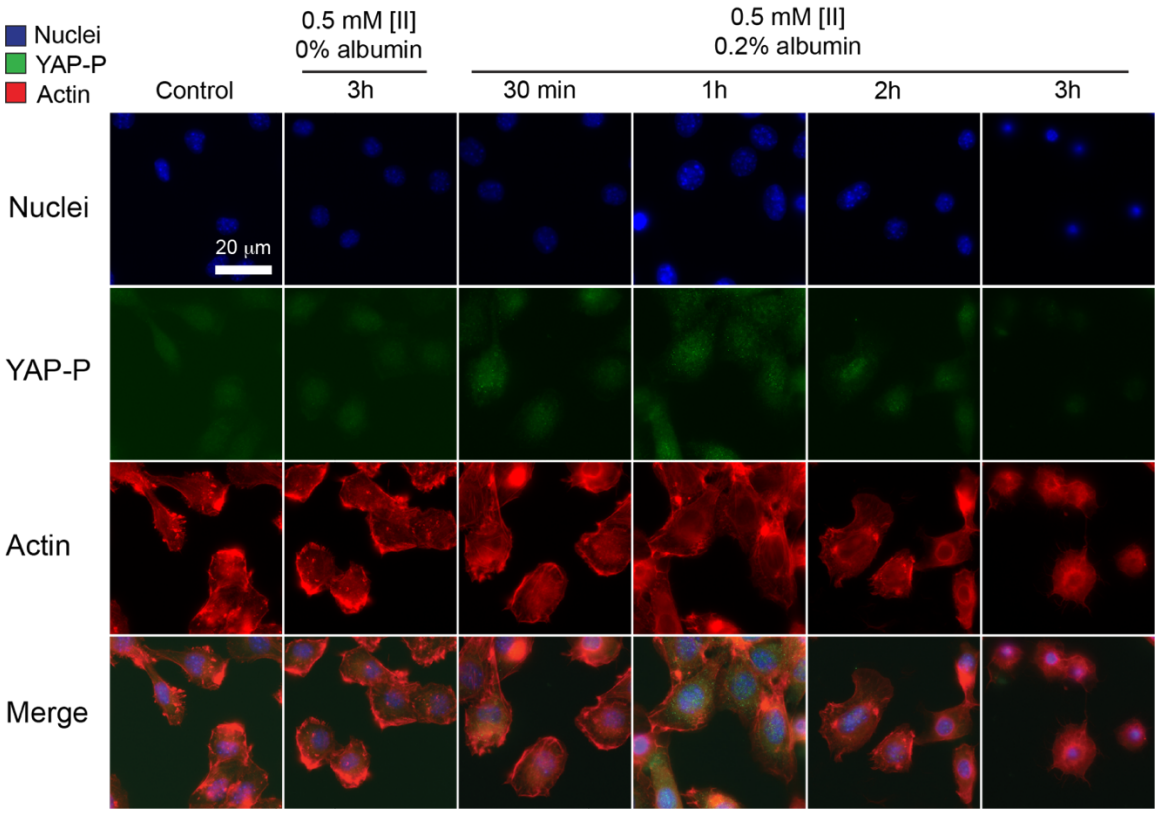


Figure 17 [II] aggregation on YAP phosphorylation localization. Immunocytochemistry of CRT cell surface localization (YAP phosphorylation = green, Actin = red, Nuclei = blue). Scale bar = 20 µm

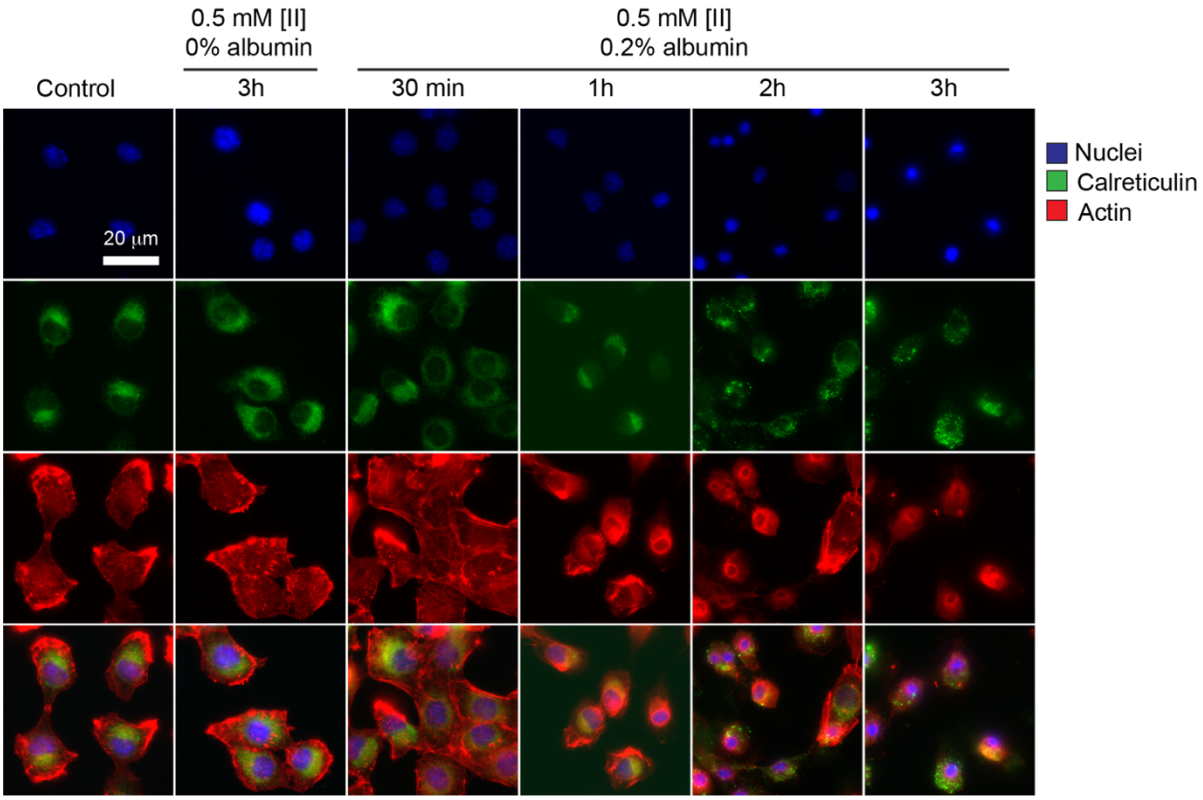


Figure 18 [II] aggregation on CRT localization. Immunocytochemistry of CRT cell surface localization (CRT = green, Actin = red, Nuclei = blue). Scale bar = 20 µm

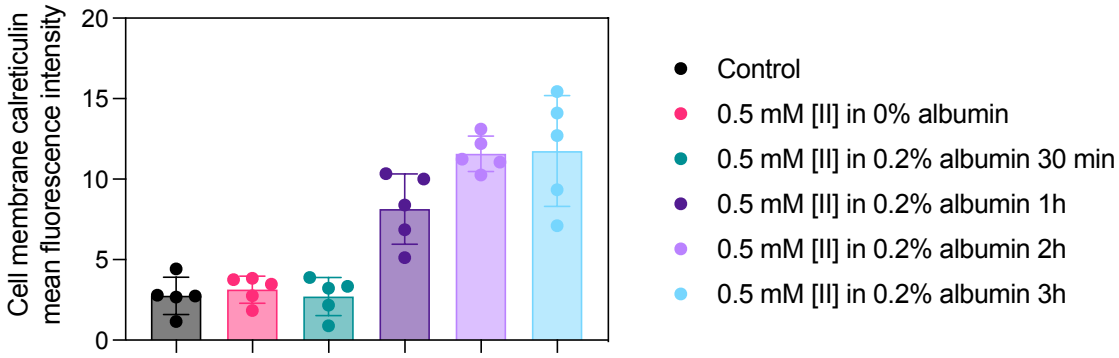


Figure 19 Quantification on CRT intensity on the cell membrane. Five random cells were selected and analyzed through ImageJ by measuring mean fluorescence intensity.

3.2.3. [II] aggregation induced ICD can be modulated

Control of [II] aggregation through albumin leads to different structures like fibrils or oligomer-like structures (**Figure 15**). Moreover, oligomer-like structures induce cell stress and display CRT outer membrane localization, a hallmark of ICD (**Figure 18**). To understand the effect of different aggregation profiles on cell membrane damage and ICD, we tested HEK293T cells with [II] peptide prepared in varying concentrations of albumin and measured the membrane damage at different time points. Increase in oligomer-like structures increased the release of LDH to the extracellular environment, indicating higher membrane damage (**Figure 20**A). As, oligomer-like structures increase, cell membrane damage increases as well, while fibrillar structures had minimal to no cell membrane damage (**Figure 20**B).

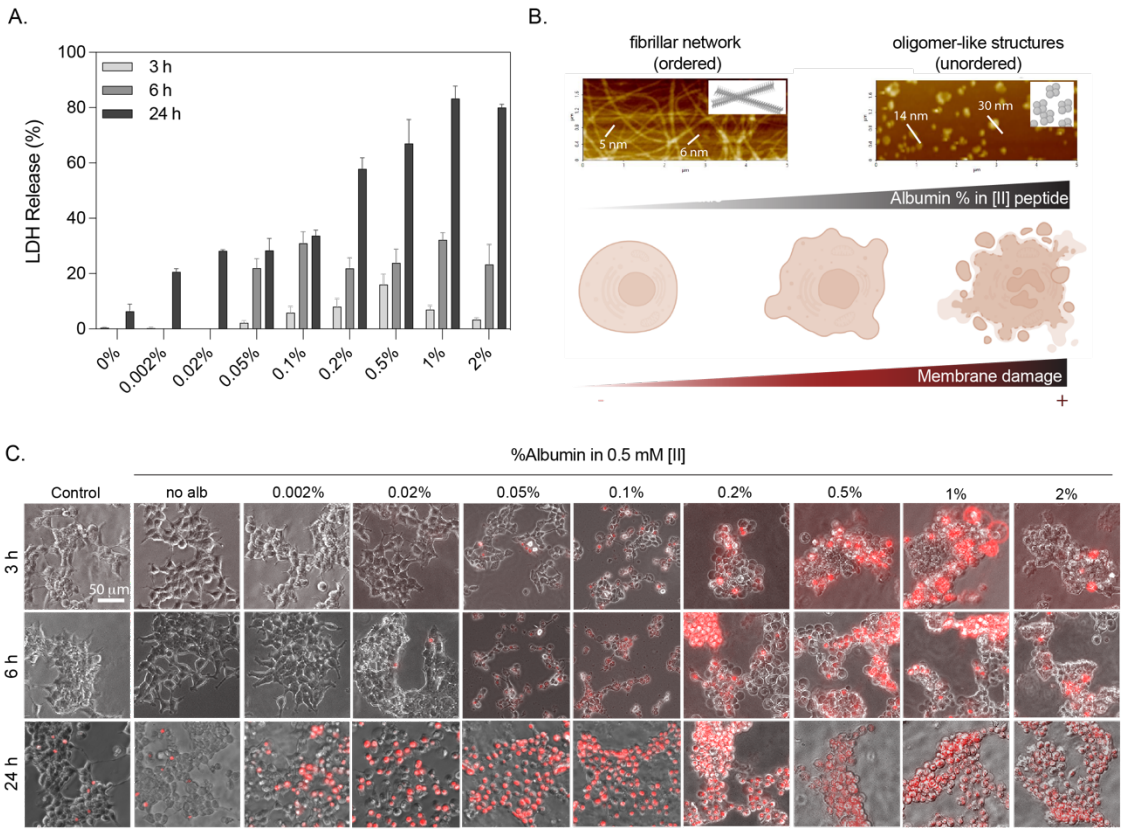


Figure 20 Cell membrane damage can be modulated through control of [II] peptide aggregation. (A) LDH release of cells treated with 0.5 mM [II] peptide prepared in indicated albumin %s for 3, 6 and 24h. (B) Schematic illustration showing the effect of fibrillar and oligomer-like structures on the membrane damage. (C) Propidium iodide uptake of cells treated with 0.5 mM [II] peptide prepared in indicated albumin %s for 3, 6 and 24h. The scale bar is 50 µm.

Propidium iodide uptake analysis also showed that, as the oligomer-like structures increase, cell membrane increases (**Figure 20**C). These results clearly demonstrate that changing the aggregation profile of [II] peptide alters the membrane damage. Additionally, regardless of the aggregation status, the eventual cellular outcome is membrane damage for different [II] oligomer-like structures.

3.2.4. [II] aggregation induced ICD induces protective immunity

Different stages of dying cells alter the protective capacity of prophylactic vaccines[51]. Given that [II] aggregation induces different cell membrane damage, we cultured EMT6 breast cancer cells with 0.5 mM [II] peptide prepared in 0.02%, 0.2% and 2% of albumin and transferred tumor-conditioned medium onto bone marrow derived DCs (BMDCs). We hypothesized that as the cell death progresses in the presence of oligomer-like structures, DAMPs will be differentially release and activate BMDC at different time points. We analyzed the activation of BMDCs by checking IL-1β release at 24h (**Figure 21**A). BMDC activation in terms of IL-1β release was significantly higher when the supernatant of EMT6 cells treated with 0.5 mM [II] in 0.2% albumin at 3h and 0.5 mM [II] in 2% albumin at 1.5h (**Figure 21**B). IL-1β release is critical for the formation of protective anti-tumor immunity[20] and given these two conditions activate the BMDCs the most, we designed a prophylactic vaccination model in which the mice were vaccinated with dying cells followed by challenge with live EMT6 cells (**Figure 21**E). Prior to injection, we analyzed the viability of dying cells and found that treatment with 0.5 mM [II] peptide in 0.2% for 3h and in 2% for 1.5h resulted in similar cell death, analyzed by propidium iodide uptake and intracellular ATP measurement (**Figure 21**C and D). Control mice, which were vaccinated with only PBS had palpable tumor as early as day 5 and by day 7 all the mice in the control group had tumors. By day 10, 4 mice from 0.5 mM [II] in 2% MSA treated EMT6 cells had tumor, while one mouse had complete protection (20%) throughout the study. Complete protection was 40% when the vaccination was carried out with EMT6 cells treated with 0.5 mM [II] in 0.2% MSA (**Figure 21**F).

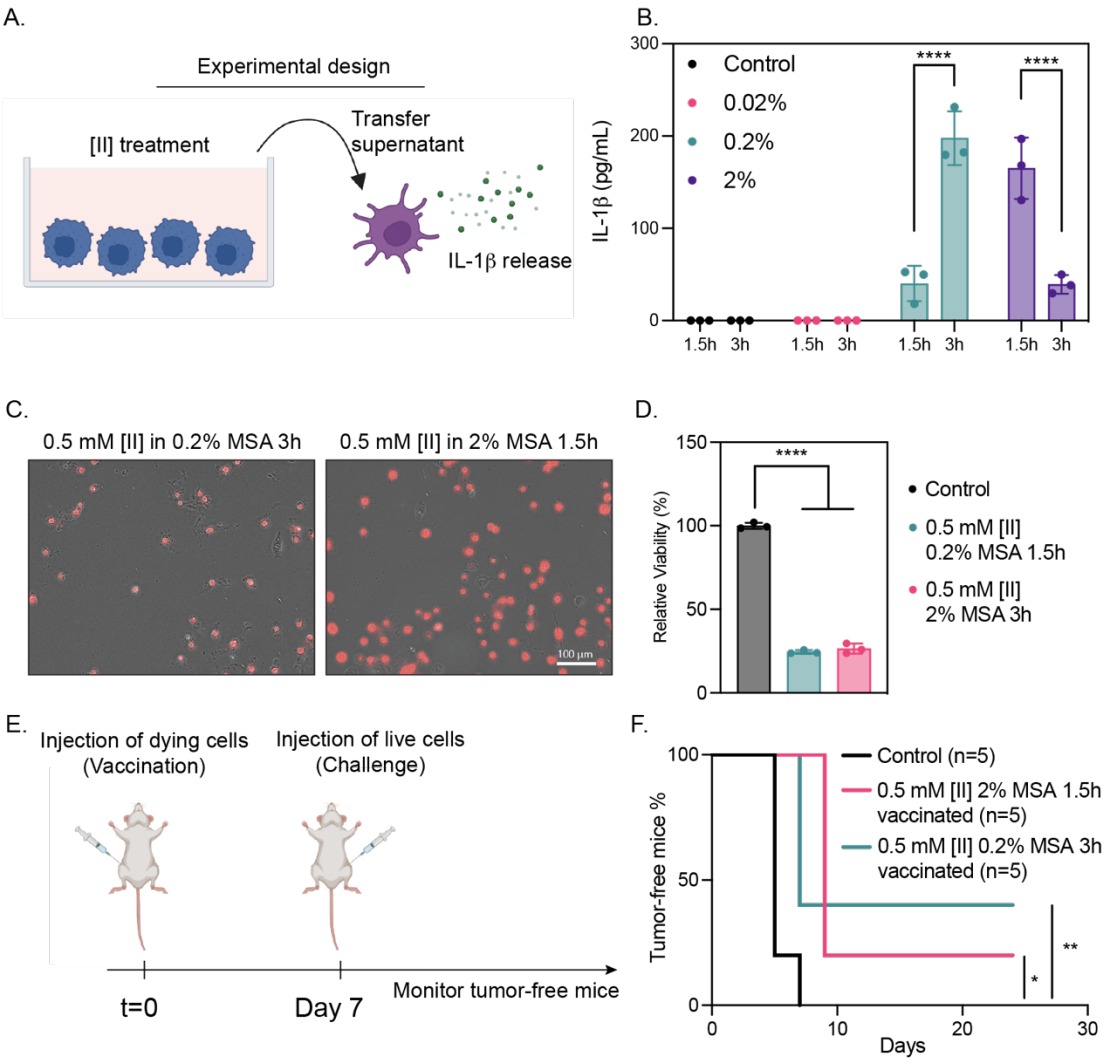


Figure 21 [II] peptide aggregation induced cell death stages effect immunogenicity. Experimental design involving the treatment of EMT6 cells for 1.5 and 3h with 0.5 mM [II] peptide prepared in 0.02%, 0.2% and 2% albumin, transfer of supernatant onto BMDCs and analysis of IL-1β release 24h later (A). Release of IL-1β from BMDCs at 24h (B). Propidium iodide (C) and ATP analysis (D) of dying cells prior to injection. Experimental design for prophylactic vaccination (E). Tumor-free mice survival graph (F) This figure is prepared using BioRender.

These results indicate that dying cells through [II] treatment is potentially protective against live challenge. Modulation of aggregation using albumin, results in different cell death profiles which ultimately changes the protective capacity of the vaccine.

3.3. Conclusions

Here we show that [II] aggregation induces cell membrane damage and engages cell stress markers as in a variety of neurodegenerative disorders. Furthermore, we showed that this aggregation can be controlled by using albumin. [II] aggregation-induced the phosphorylation of eIF2α and CRT surface localization, which highlighted ICD. The modulation of peptide aggregation presented here, allows us to control cell membrane damage and offers us to modulate immunogenic cell death. Additionally, different [II] aggregation profiles enabled different levels of protection in a breast cancer prophylactic vaccination model.

Protein and peptide aggregation is a phenomenon that can be seen in both pathogenic conditions and during developmental stages of amyloid proteins. Oligomeric species form transiently during the aggregation process and not only act as essential intermediates but also represent major pathogenic agents in disorders. However, the transient and complex structures and aggregates of oligomers create confusing results and challenge in drug development. In this study, we showed an engineered peptide complex via CoOP strategy as a synthetic and simple tool to study the amyloid aggregation mechanism into ordered assemblies (fibrils) and disordered aggregates (oligomers) with the presence of albumin, and correlate it to its toxicity. Importantly, we showed that, albumin can control the aggregation kinetics of [II], which induce mechanical

stress on the cells and ICD. The immune response against ICD is potent. Controlling ICD means control over the immune response and progress of amyloidosis-related diseases.

Overall, [II] offers a unique engineered platform to study aggregation kinetics of amyloidosis. The simplicity of [II] as an engineered tool allowed the detailed characterization of disorganized structures to fibril aggregation kinetics and the effects of each step on cell. Studies with [II] can serve to establish clear and direct results for drug development with amyloidosis.

3.4. Experimental section

3.4.1. Peptide Synthesis

KFFIIK and EFFIIE peptides were synthesized via solid phase peptide synthesis with PreludeX automatic peptide synthesizer (Protein Technologies, Inc., Tucson, AZ). They were prepared on a 0.25 scale by repeated amino acid couplings using Fmoc protected amino acid (3 eq. 1mL), DIC (7.5 eq. 1mL) and Oxyma (7.5 eq. 1mL). MBHA Rink Amide resin (High-Loaded, Gyros Protein Technologies) was used as solid support to construct the peptides. Fmoc protected amino acids (Gyros Protein Technologies) were removed through treatment with 20% piperidine/DMF solution for 45 min (three times for 15 min) at 80°C. All the peptide conjugation was performed for 2h at 80°C and acetylated with a treatment with 10% acetonitrile/DMF solution for 15 min twice. Cleavage of the peptides from resin and deprotection of acid labile protected amino acids were carried out with a mixture of TFA/ TIS/ water in a ratio of 95:2.5:2.5 for 3 h at room temperature. Excess TFA and organic solvents were removed by evaporation and the remaining peptide was precipitated using diethyl ether at 80°C by using 1:4 volume ratio and stayed overnight. After precipitation, peptides in ether solutions were centrifuged at 8000 rpm for 15 min. Peptide precipitates were collected and ether was removed. The centrifuged white peptide

precipitate was dissolved in either (0.1% formic acid in water for KFFIIK peptide) or (0.1% ammonium hydroxide in water for EFFIIE peptide). Peptides were purified with preparative HPLC (Agilent 1260) with Agilent ZORBAX 300 SB-C18 (9.4 x 250 mm) column with a mobile phase of water/acetonitrile mixture (0.1% ammonium hydroxide) used for negatively charged peptides; water/acetonitrile mixture (0.1% formic acid) was used for positively charged peptides. All peptides were tested with a purity >95%. HPLC run started with 100% water for 3 min, followed by a gradient increase in acetonitrile from 0% to 100% over 25 min, followed 100% acetonitrile for 3 min, and ended with 100% for 2 min. The flow rate is 2 mL/min and injection volumes are 10 µL.

3.4.2. Atomic Force Microscopy

Morphological characterization of [II] was performed with AFM (NX-10 Park Systems Corp) with a non-contact mode by using a cantilever probe (OMCL-AC160TS 5M). Peptide were prepared by either with albumin (0.002 w%, 0.02 w%, 0.2 w%, 2 w%) or without albumin (0 w%) in PBS. At first, 0.5 mM KFFIIK (50 µL) was prepared with or without albumin, and 0.5 mM EFFIIE (50 µL) was prepared with or without albumin in PBS. Then, two oppositely charged peptides were mixed and incubated overnight (~ 20h). For sample preparation, mixed samples were diluted to 0.1 mM with water, and 20 µL dropped onto a silicon wafer. Prepared samples were dried at room temperature and imaged with a 1 kHz scanning frequency. Data points were taken in a 256 x 256 grid over a 5 µm–by–5 µm area.

3.4.3. Cell Culture

EMT6 cells were cultured in Roswell Park Memorial Institute (RPMI) 1640 Medium, supplemented with 10% FBS (Hyclone SH30910.03) and 1% antibiotics; penicillin (100 U/mL), and streptomycin (100 µg/mL) (Thermo Fisher 15240062) according to the manufacturer's instructions. Cells were cultured in a humidified incubator at 37°C supplied with 5% CO2. T75 flasks (TPP 90076) were used for culturing and cells were passaged upon 85% confluency by using trypsin (Sigma 59418C). Cell culture media was changed every 2 days.

3.4.4. Peptide Preparation for in vitro Experiments

[II] peptides were prepared in either 0.2 w% albumin or 0 w% albumin for in vitro conditions. First, albumin was pre- pared as a stock solution in 2% (20 mg in 1 mL the RPMI medium). Then, was diluted 1:10 to reach 0.2w% in the RPMI medium. The prepared KFFIIK and EFFIIE stock peptides (10 mM in water) were diluted to 0.5 mM separately into 0.2w% albumin/medium. For 0w% albumin condition, KFFIIK and EFFIIE stock peptides 10 mM in water) were diluted to 0.5 mM separately into albumin/medium. For 96 well plate, each well consisted of 100 µL of peptide having 50 µL EFFIIE and 50 µL KFFIIK in either only RPMI medium (0 w% albumin) or 0.2 w% albumin in RPMI medium.

3.4.5. Immunoblotting, Reagents

Acrylamide/Bis-acrylamide, 30 w% solution (Sigma A3699), 1.5 M Tris-HCl, pH 8.8 (Teknova T1588), Tris HCl Buffer 0.5 M solution, sterile pH 6.8 (Bio Basic SD8122), Ammonium persulfate (Sigma A3678), UltraPure 10% SDS (Invitrogen 15553-027), TEMED (Thermo Fisher Scientific 17919), Dithiothreitol (DTT) (BIO-RAD 1610610) Tris Base (Fisher Bioreagents BP152), Glycine (Fisher Bioreagents BP381), 4x Laemmli sample buffer (BIO-RAD 1610747), TWEEN 20 (Sigma

P9416), Mini Trans-Blot filter paper (BIO-RAD 1703932), Nitrocellulose Membranes 0.45 µm (BIO-RAD 1620115), EveryBlot Blocking Buffer (BIO-RAD 12010020), Clarity Western ECL Substrate (BIO-RAD 170-5060).

3.4.6. Procedure

Protein isolation was carried out using RIPA lysis buffer, supplemented with Protease and Phosphatase inhibitor cocktail. Supernatants were collected after 10 min of centrifuge at 14000g and stored at -80 °C. Protein concentrations were determined by using BCA protein assay kit (Thermo Fisher Scientific 23225) by measuring the absorbance at 562 nm in accordance with the manufacturer's instructions. Samples were prepared in Laemmli buffer and boiled for 8 min at 96°C. Then, proteins were separated with sodium dodecyl sulfate-polyacrylamide gel electrophoresis (SDS-PAGE) gels (8.5 w% and 15 w%) and transferred to nitrocellulose membranes (45 µm). After transfer, the membranes were blocked EverBlot Blocking Buffer and washed with Tris Buffered Saline with 0.1% Tween 20 (TBST). Blots were incubated with Phospho-YAP (Ser127) (Cell Signaling 13008), YAP (Cell Signaling 4912), Phospho-eIF2α (S51) (Cell Signaling 9721), eIF2α (Cell Signaling 9722) overnight. The next day blots were washed and incubated with Goat anti rabbit secondary antibody (Invitrogen 31460) and imaged with Clarity Western ECL substrate (BIO RAD 170-5060). β-actin (Santa Cruz sc-47778 HRP) was used as an internal loading control. Blots were imaged by using Azure c600.

3.4.7. Immunocytochemistry

EMT6 cells were seeded on glass coverslips in a 24 well plate and incubated overnight for attachment. After indicated treatments, samples were washed with 1X PBS, and fixed with 4% PFA for 20 min. Then, Triton-X (0.5%) was used to permeabilize the cells for 20 min on shaker.

Samples were blocked with 3% BSA for 1h on shaker, washed 3 times with 1X PBS and incubated with the following antibodies Phospho-YAP (S127) (Cell Signaling 13008), YAP (Cell Signaling 4912) or CRT (Cell Signaling D3E6) overnight on shaker on ice. The next day samples were washed and incubated for 1h on shaker with DyLight™ 488 Donkey anti-rabbit IgG (minimal x-reactivity) Antibody (BioLegend 406404). After the incubation period, samples were washed and incubated with Flash Phalloidin™ Red 594 (BioLegend 424203) for 30 min on shaker. Lastly, samples were washed and mounted in ProLong™ Glass Antifade Mountant with NucBlue™ Stain (Thermo Fisher P36981) and stored in the dark until imaging.

3.4.8. LDH Release

LDH release was measured with Cytoscan-LDH Cytotoxicity Assay (Cat# 786-210). Briefly, collected supernatants were mixed with reaction mixture and incubated for 20 min at 37 °C. Reaction was stopped with stop solution and absorbance was measured at 490nm and 680nm. Triton-X treatment is used as a 100% LDH release control. 680 nm absorbance is used as the background signal and values were subtracted from 490nm absorbance values. Relative LDH release was quantified based on the positive control for LDH release (maximum LDH release through Triton-X treatment)

3.4.9. Propidium Iodide Staining

Propidium iodide (Thermo Fisher Scientific V13242) was used to stain the cells after treatment. Briefly, PI was added onto each well and images were captured with Keyence BZ-X710 microscope at indicated time points.

3.4.10. Bone Marrow-derived Dendritic Cell Generation

Bone marrow was harvested from the femurs and tibia of an 8-week-old BALB/c mouse. Bones were flushed with a cold medium 2 times and centrifuged twice at 1500 rpm for 5 min. Cells were incubated with 20 ng/mL GMCSF (BioLegend 576304) at a density of 2 x 10^6 cells for 8 days. On day 3, 20 ng/mL GMCSF in 10 mL is added and on day 6, 10 mL of cell solution was replaced with 10 mL fresh medium containing 20 ng/mL GMCSF. On day 8 loosely adhering BMDCs were collected through gentle pipetting.

3.4.11. Enzyme-Linked Immunosorbent Assay (ELISA)

BMDCs were co-cultured with the tumor conditioned mediums for 24h. BMDC media was collected and centrifuged at 500 g for 5 min at 4 °C and supernatants were collected for ELISA. Briefly, plates were coated with the capture antibody overnight. The next day plates were blocked and incubated with the supernatants. Then plates were incubated with the detection antibody followed by Avidin-HRP incubation. Plates were developed with TMB substrate solution. Absorbance was measured at 450 nm and 570 nm. 570 nm value was subtracted, and values were calculated based on the standard curve for IL-1β (BioLegend 432615).

3.4.12. Ethics

This study was carried out in accordance with the recommendations of Guide for the Care and Use of Laboratory Animals from National Institute of Health. Animal procedures were approved by the OU Health Sciences Center (OUHSC) Institutional Animal Care and Use Committee (protocol number R19-017A)

3.4.13. Prophylactic Vaccination Model

BALB/c mice (n=5) were vaccinated subcutaneously with PBS, 100.000 EMT6 cells treated with 0.5 mM [II] peptide in 2% MSA for 1.5h or 100.000 EMT6 cells treated with 0.5 mM [II] peptide in 0.2% MSA for 3h. 7 days later all mice were challenged with 50.000 EMT6 cells at the contralateral site subcutaneously. Formation of palpable tumor on both vaccination site and challenge site were recorded and presented as a survival graph indicating tumor-free mice.

Chapter 4: Tumor Spheroid Model to Study Peptide Aggregation Induced Immunogenic Cell Death

Introduction of this section is adapted from the following publication:

Kamatar, Advika, Gokhan Gunay, and Handan Acar. "Natural and synthetic biomaterials for engineering multicellular tumor spheroids." *Polymers* 12, no. 11 (2020): 2506.

4.1. Introduction

The lack of in vitro models that represent the native tumor microenvironment is a significant challenge for cancer research. Two-dimensional (2D) monolayer culture has long been the standard for in vitro cell-based studies. However, differences between 2D culture and the in vivo environment have led to poor translation of cancer research from in vitro to in vivo models, slowing the progress of the field. Recent advances in three-dimensional (3D) culture have improved the ability of in vitro culture to replicate in vivo conditions. Although 3D cultures still cannot achieve the complexity of the in vivo environment, they can still better replicate the cell–cell and cell–matrix interactions of solid tumors. Multicellular tumor spheroids (MCTS) are three-dimensional (3D) clusters of cells with tumor-like features such as oxygen gradients and drug resistance and represent an important translational tool for cancer research. Accordingly, natural and synthetic polymers, including collagen, hyaluronic acid, Matrigel®, polyethylene glycol (PEG), alginate and chitosan, have been used to form and study MCTS for improved clinical translatability. This review evaluates the current state of biomaterial based MCTS formation,

including advantages and disadvantages of the different biomaterials and their recent applications to the field of cancer research, with a focus on the past five years.

Lack of translation from the results of preclinical research to clinical trials has been a major problem in cancer research. 2D cell culture and mouse models have long been the standard for studies of cancer biology and drug screening and have greatly improved our understanding of cancer's complexities. However, 2D culture exposes cells to a rigid plastic surface on one side and to a liquid on the other as cells grow in a flat monolayer, altering the cytoskeleton and causing abnormality in cellular functions such as metabolism and protein expression [227]. Mouse models are more relevant than 2D culture to complex human biology and have greatly enhanced our understanding of tumor biology, but they suffer from high cost and resource requirements [228]. Ethical review boards encourage researchers to at least reduce or refine, if not entirely replace, their animal usage in order to harm as few animals as possible—a principle known as "the three Rs" [229]. Furthermore, mouse models do not completely reproduce the complexity of human physiology and metabolism, which may contribute to why less than 8% of medicinal compounds entering Phase I trials eventually make it to market as noted in a 2004 FDA report [230,231]. Alternatives to 2D culture and mouse models include clinical samples, but their use is limited by intratumoral heterogeneity and are governed by many federal regulations [232], making them low-throughput and difficult to routinely use.

Recent advances in 3D cell culture, such as cell culture in hydrogels that mimic the extracellular matrix, have attempted to bridge the gap between preclinical and clinical results. In particular, multicellular tumor spheroids (MCTS) have emerged as a promising *in vitro* model for cancer research because of their high throughput, low cost and increased physiological relevance

compared to 2D culture. MCTS are defined as 3D spherical clusters of malignant cells [233], and have been shown to mimic many features of solid tumors *in vivo*, such as cell-cell and cell-extracellular matrix interactions [234,235], increased drug resistance [236–238], cell polarity [239], and nutrient diffusion gradients [240].

Studies on MCTS began in the 1970s and 1980s, led by the efforts of R.M. Sutherland and colleagues [241,242]. In metastatic tumors, lack of vascularization leads to areas of necrosis of cells with nutrient deficiency, hypoxia, and acidity [242–244]. Tumors also exhibit layers of proliferating, quiescent (non-proliferating), and necrotic cells at progressively greater distances from blood vessels [242]. As we demonstrated in Figure 1, it is now well established that MCTS replicate these steep nutrient, oxygen and pH gradients and cell layers in those typically above 500μm in diameter **(Figure *22*)** [245]. Another hallmark of metastatic cancer is the epithelial-to-mesenchymal transition (EMT), in which epithelial cancer cells lose cell-cell adhesions such as E-cadherin, apical-basolateral polarity, and take on a mesenchymal phenotype to promote migration and invasion [239]. MCTS culture, as opposed to 2D culture, can induce this EMT [246] and affect the migratory profiles of MCTS [238], which is crucial in studies attempting to understand and prevent metastasis. In fact, in ovarian cancer, metastasis is proposed to occur through detachment of cells into the peritoneal cavity, where they aggregate into MCTS and create malignant ascites [239], further highlighting the direct relevance of the MCTS model to human cancer pathophysiology.

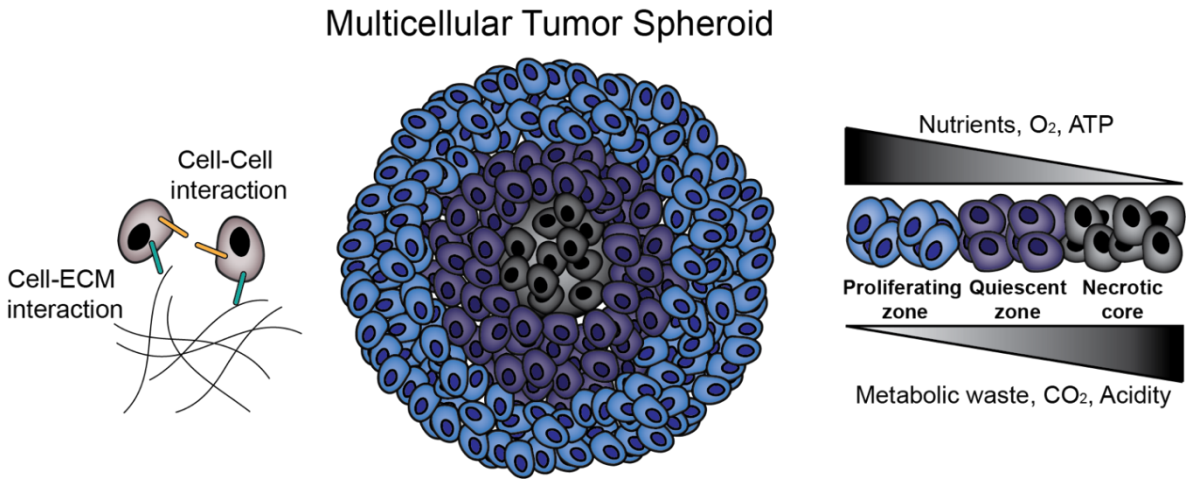


Figure 22 MCTS Biology. MCTS provide an in vitro platform for the investigation of cell-cell and cell-ECM interactions. Additionally, MCTS mimic in vivo solid tumors in terms of nutrient, oxygen and pH gradients and zone formation.

There are two broad strategies for preparation of MCTS as an *in vitro* model for drug screening and cancer biology investigation: matrix-free formation and matrix-dependent formation. Matrix-free MCTS formation techniques include culture via liquid overlay, hanging drop, rotating spinner flasks, and magnetic levitation [247,248]. Matrix-free techniques have been widely used due to their high throughput, high reproducibility, and relative ease of culture, but they do not include tumor extracellular matrix (ECM) during initial assembly, which provides important physicochemical cues in tumor development *in vivo* [249,250]. Matrix-dependent techniques, in contrast, involve the use of biomaterials to recreate these *in vivo* cell-ECM interactions. It should be noted that microfluidics has also been considered a promising strategy for MCTS formation and culture, and this technique often incorporates polymers that are discussed throughout this review. Engineering considerations for microfluidic MCTS formation have been extensively reviewed elsewhere [251], and will not be a focus here. The purpose of this review is to provide a

practical guide for choosing a technique for MCTS formation *in vitro*. Matrix-free and matrix-dependent techniques for MCTS formation are explained with an emphasis on biopolymer matrix-dependent techniques. Advantages and disadvantages of each biopolymer and their recent applications are explained

4.1.1. Matrix-free MCTS Formation

Matrix-free MCTS formation occurs through self-aggregation of cells. During this process, cells also produce certain components of ECM and organize their own 3D structure. This provides a good platform to study completely endogenous ECM. Matrix-free techniques include liquid overlay, hanging drop, spinner flask and magnetic levitation, as reviewed briefly below. Each technique is depicted in **Figure 2**. In addition, to the authors' knowledge there is no definition of when an aggregate becomes an MCTS, so many papers do not report the exact day that MCTS "formed," but rather monitor their culture over several days as they increase in compactness from initial seeding to a spherical body.

4.1.1.1. Liquid Overlay Technique

The liquid overlay technique (LOT), sometimes referred to as the ultra-low attachment (ULA) technique, is based on using non-adhesive plastic surfaces or functionalizing the surfaces of tissue culture well plates with non-adhesives (hydrophilic polymers) [247]. For example, poly (2-hydroxyethyl methacrylate) (HEMA) treated surfaces resulted in hepatocyte spheroid formation [252], and ATDC5 chondrocyte cells formed spheroids on polyethylene glycol (PEG) coated surfaces [253]. Elimination of cell-surface interactions allows increased cell-to-cell interaction and initiates MCTS formation **(Figure 23A)**. In addition to its low cost and relatively easy handling, one major advantage to using the LOT is that it provides post-processing directly in the plates where MCTS

are formed [235,254], making it very useful in high-throughput experiments [255]. Typical MCTS formation with this technique involves functionalizing the surface with either biomaterials or commercially available anti-adhesive solutions, followed by washing the surfaces and seeding cells. MCTS formation varies among cell types and should be optimized for different cell lines. Exchanging 50% of the culture media offers fresh medium for the MCTS while preventing the loss of MCTS due to accidental removal of the MCTS along with the medium.

LOT frequently uses microwells as a culture platform because they offer a defined structure for consistent, reproducible, and size-controllable MCTS formation. Several commercial products are available to generate MCTS in microwells via LOT, including Aggrewell™ plates (Stemcell™ Technologies) and Elplasia® plates (Corning®). These products free the researcher from tedious traditional microwell fabrication but lack the flexibility to change well structure or volume depending on the application. In response to these shortcomings, researchers have fabricated their own microwells using non-adhesive biomaterials with the goals of geometrical symmetry, sufficient well volume, low surface roughness, and low cost [256]. For example, microwell formation via CO_2 laser ablation of polystyrene has been shown to produce size controlled A549 lung cancer MCTS [256]. In addition to polystyrene, agarose is a very common non-adhesive biomaterial used to form microwells, and allows MCTS formation without any additional surface modification [257–259].

LOT is one of the most common matrix-free approaches and has enabled important progress in studies on cancer stem cell formation and chemoresistance. For example, the LOT was recently used to study the effect of size and shape of ovarian carcinoma MCTS on drug resistance to Cisplatin and Taxol, as well as migration capacity of different MCTS morphologies [238]. However,

not all cell lines are able to form MCTS via this technique, even within the same type of cancer. For example, while OVCAR8 and OVCAR3 cell lines formed compact and loose spheroids, respectively [238], the ovarian carcinoma line SKOV-3 did not form MCTS similar to those found in patient ascites, possibly due to the different cell surface receptors expressed on different cell lines [260]. Thus, LOT requires a well-researched choice in cell lines. Because of the ease of sample preparation and low cost, as well as having samples with ECM structures relevant to their physiological counterparts, LOT is one of the most reliable and commonly used technique for the cell lines that are known to form aggregates.

4.1.1.2. Hanging Drop Technique

The hanging drop technique requires no special equipment and relies on preparation of desired numbers of cells/drop and provides reproducible MCTS formation [261]. Cell suspension drops (15–30 mL) are placed onto the underside of the lid of a tissue culture plate **(Figure 23B)**. When inverted, surface tension keeps the drop intact and forces cells to localize at the bottom of the drop [247]. One disadvantage of this technique is that the MCTS have to be transferred prior to post processing [262]. Additionally, volumes used to culture MCTS are very small volumes (10–15 mL), so evaporation is a major problem [263]. A comparison between LOT and the hanging drop technique illustrated the ease of handling and monitoring when using LOT [264].

4.1.1.3. Spinner Flask Technique

The spinner flask technique allows cell to cell interaction by preventing the settling of the cells through continuous spinning [265], and leads to MCTS formation **(Figure 23C)**. For example, HepG2 hepatocellular carcinoma cell suspensions were seeded at 1×10^5 cells/mL into 500 mL siliconized spinner flasks and stirred at 60 rpm for 4–6 weeks. The resulting MCTS were 200–300 µm

diameter and were transferred into agarose-coated well plates for further processing [266]. In another study, rat liver hepatocytes were cultured at 5×10^5 cells/mL in a 250 mL spinner flask for 6 hours, resulting in 80% aggregate formation [267]. The speed of the continuously rotating flask is important to consider; low speeds might result in settling of the cells and high speeds might harm the cells due to shear stress. One advantage of using the spinner flask is the ability to produce large quantities of MCTS. However, during continuous spinning MCTS formation cannot be visualized [265], which is important in monitoring morphology and size.

4.1.1.4. Magnetic Levitation Technique

The magnetic levitation technique enables cells to form MCTS through applying magnetic field [248]. Prior to magnetic force application, cells of interest are loaded with magnetic nanoparticles and application of magnetic force to draw cells together facilitates cell-cell adhesion and subsequently MCTS formation **(Figure 23D)**. In addition to forming tumor models [268], it has also been used for adipose tissue [269] and bronchiole culture [270]. The magnetic levitation technique, in addition to MCTS formation, also offers MCTS fusion; astrocyte MCTS and glioblastoma MCTS were fused within 12 hours by using this technique [248]. Magnetic levitation offers a platform where MCTS are formed in a short period of time relative to other approaches (e.g. 24 hours for magnetic levitation compared to 7 days in Matrigel culture [268]), which allows faster imaging [271]. It must be considered that, even though magnetic nanoparticles have been shown not to affect cell behavior or an inflammatory response within 30-500 G magnetic field [248,270], a higher magnetic field (800-400 G) has been shown to affect cell behavior [272].

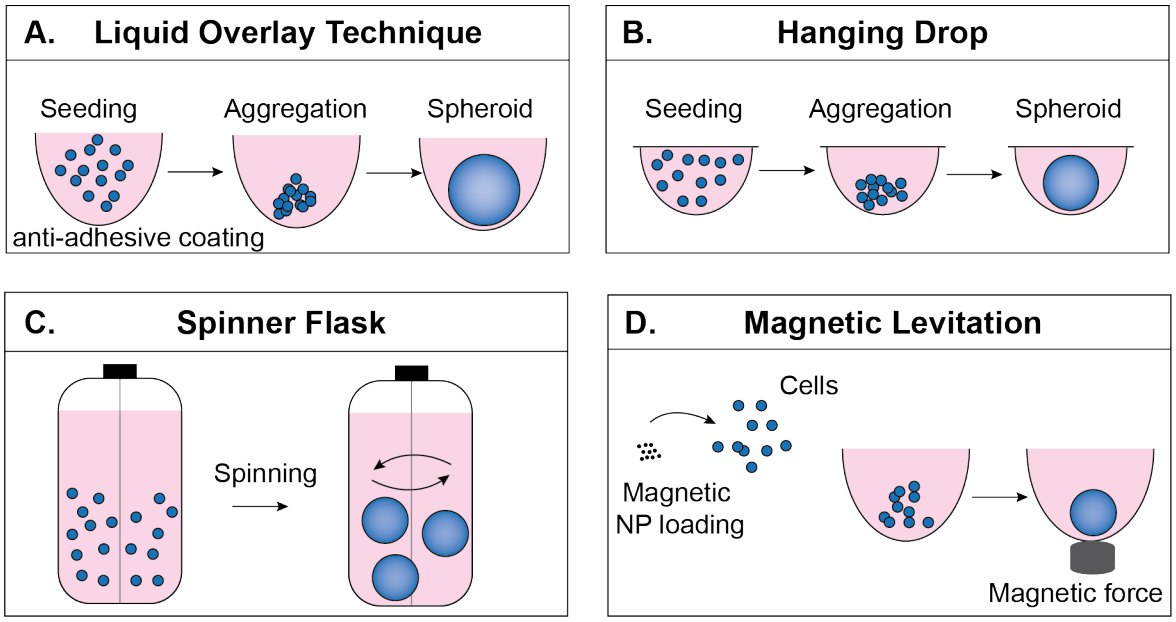


Figure 23 Matrix-free formation techniques. A) In the liquid overlay technique, cells are seeded onto a surface that prevents adhesion, encouraging cell-cell adhesion. B) In the hanging drop technique, cells are suspended in drops from the underside of a culture plate lid. C) In the spinner flask technique, rotational motion encourages cell-cell adhesion. D) In the magnetic levitation technique, cells take in magnetic nanoparticles and are aggregated by magnetic force.

4.2. The effects of size and shape of the ovarian cancer spheroids on the drug resistance and migration

This study is published, and citation key is the following:

Gunay, Gokhan, Hande A. Kirit, Advika Kamatar, Ofelya Baghdasaryan, Seren Hamsici, and Handan Acar. "The effects of size and shape of the ovarian cancer spheroids on the drug resistance and migration." *Gynecologic Oncology* 159, no. 2 (2020): 563-572.

4.2.1. Abstract

High fatality in ovarian cancer is attributed to metastasis, propagated by the release of multi-cellular aggregates/spheroids into the peritoneal cavity and their subsequent mesothelial invasion of peritoneal organs. Spheroids are therefore a common and clinically relevant in vitro model for ovarian cancer research. Spheroids in patients vary significantly in size and shape and display enhanced resistance to anti-cancer drugs compared to monolayers. However, there is no consensus on how spheroid size and shape affect drug resistance. Moreover, existing data regarding the influence of epithelial-to-mesenchymal transition (EMT) profile on spheroid shape and migration is inconclusive.

4.2.2. Introduction

Epithelial ovarian cancer (EOC) is the most lethal gynecological disorder. EOC makes up 90% of all ovarian cancer cases,[273] and is fatal to more than 70% of patients within 5 years of diagnosis[274]. High mortality rates are attributed to peritoneal metastasis during the advanced stages of the cancer through tumor tissue dissemination into the ascites either as single cells or multi-cellular aggregates/spheroids[275]. Regardless of the cancer type, malignant ascites are associated with poor prognosis[276], and observed in more than one third of EOC patients[275]. Collective detachment and spheroid formation within patient ascites potentiate resistance in cancer cells against anoikis[277] as well as anti-cancer drug treatments[278]. These spheroids within the ascites can attach and invade the other peritoneal organs through the mesothelial layer[279],[280]. Patient-derived spheroids exhibit a wide range of size[281] and morphology, such that spheroids can be observed both as loose aggregates and tight (compact) spherical aggregates even within the ascites of the

same patient[282]. However, experimental investigation of the specific effects of spheroid size and morphology on drug sensitivity is scarce.

Recognized as a key event during cancer progression[283], epithelial-to-mesenchymal transition (EMT) is the phenotypic switch of the tumor tissue from epithelial to mesenchymal (i.e., a decrease in cell-cell adhesion, leading to increased proliferation, motility and invasiveness)[284]. This transition is regulated by a number of transcription factors, and characterized by the downregulation of several epithelial markers and the upregulation of several mesenchymal markers[285]. E-cadherin is one such epithelial marker; it plays a key role in cell-cell adhesion as a transmembrane protein localized at the epithelial cell membranes[286,287] and strengthens cell-cell interactions in collaboration with cytoskeleton proteins[288] EOC is a complex disease and may originate either from the epithelial cells at the surface of ovaries or from those of the fallopian tubes[289] where E-cadherin regulates the epithelial cell behavior[288]. While E-cadherin is downregulated in EMT, vimentin (a mesenchymal intermediate filament cytoskeletal protein) is upregulated in EMT;[290] overexpression of vimentin is highly correlated with increased motility and invasive profile in cancer cells[291,292]. However, the EOC shows ambiguous EMT phenotype, in terms of expression levels of these markers and how these changes affect the tumor progression and invasiveness[293,294].

Recent advances in three-dimensional (3D) cell culture techniques have substantially reduced the gap between in vitro and in vivo[295] environments. 3D cultures offer *in-vivo*-like cell-to-extracellular matrix (ECM) and cell-to-cell interactions which cannot be achieved by traditional monolayer cell culture[295,296]. Because EOC disseminates mainly in the form of multi-cellular

aggregates/spheroids, spheroid formation has widely been used for in vitro tumor models to investigate ovarian cancer.

In this study, we examined two key EOC cell lines that form spheroids with morphologies and sizes similar to those observed in patients[297] using an ultra-low attachment technique. This approach therefore provides an accurate in vitro model of spheroids from patient-derived ascites, supported by the production of two distinct morphologies across various sizes: OVCAR-3 cells form loose aggregates, while OVCAR-8 cells form compact spheroids. Using this approach, we can therefore address the specific questions: 1) Is there a relationship between spheroid size/morphology and drug resistance in EOC spheroids? 2) Do different spheroid morphologies exhibit different expressions of EMT markers? 3) Are the levels of these markers correlated with the migration profiles of spheroids? The results of this study can, therefore, help to elucidate general rules for ovarian cancer studies based on 3D samples.

4.2.3. Materials & Methods

4.2.3.1. Cell Culture and Reagents

Epithelial ovarian cancer cell lines OVCAR-3 (ATCC # HTB-161), OVCAR-8 (NCI-Vial Designation 0507715) were cultured in humidified incubator at 37 °C supplied with 5% CO_2. Cell line authentication and mycoplasma testing was performed by University of Arizona, Genetics Core. OVCAR-3 and OVCAR-8 cells were cultured in Roswell Park Memorial Institute (RPMI) media (SIGMA R8758) supplemented with 10% FBS (Hyclone SH30910.03) and 1% antibiotics; penicillin (100 U/mL), and streptomycin (100 μg/mL) (Thermo Fisher 15240062) according to the manufacturer's instructions. T75 flask (TPP 90076) and T25 flask (TPP 90026) were used for

culturing the cells and cells were passaged by using trypsin (Sigma 59418C) upon 85% confluency. Media was changed every 2 days.

4.2.3.2. Spheroid Formation and Characterization

Spheroids initiated with 50-100-200 and 500 cells: AggreWell™ 400 plates (STEMCELL Technologies 34415) were used to form ovarian cancer spheroids. Briefly, wells were treated with 500 μl/well anti-adherence rinsing solution (STEMCELL Technologies 07010) and centrifuged for 5 min at 1300 *g*. Then rinsing solution was removed and wells were washed with 2 mL of basal medium. 1 mL of fresh media was added into the wells and 1 mL media containing the desired number of cells were added and the plate was immediately centrifuged for 3 min at 100 *g* to obtain homogeneous distribution into microwells. For all cell lines, spheroids were initiated with 50, 100, 200 and 500 cells and monitored over the course of 6 days. Media was changed every 2 days by slowly removing 1 mL of medium and addition of 1 mL fresh medium. Each well of AggreWell™ 400 plates (STEMCELL Technologies 34415) contains 1200 microwells, therefore, number of cells added in each well is calculated accordingly: We have added, $6\ x\ 10^4$ cells/well to initiate spheroids with 50 cells, $1.2\ x\ 10^5$ cells/well to initiate spheroids with 100 cells, $2.4\ x\ 10^5$ cells/well to initiate spheroids with 200 cells, $6\ x\ 10^5$ cells/well to initiate spheroids with 500 cells.

Spheroids initiated with 5000 cells: U-Bottom 96 well plates (CELLTREAT 229590) were used to form ovarian cancer spheroids. Briefly, wells were treated with 100 μL/well anti-adherence rinsing solution (STEMCELL Technologies 07010) and centrifuged for 5 min at 1300 *g*. Then rinsing solution was removed and wells were washed with 200 μl/well of basal medium. Then desired

cell numbers were added into wells in 200 μL/well and centrifuged for 3 min at 100 *g*. Media was changed every 2 days by slowly removing 100 μl/well of medium and addition of 100 μl/well fresh medium.

4.2.3.3. Characterization of Spheroids

Spheroids were imaged every 24 h and later analyzed for their area, diameter, circularity and solidity by using ImageJ as previously described:[264]

$$Circularity = \frac{(4\pi \times Area)}{Perimeter^2}$$

$$Solidity = \frac{Area}{Convex\ Area}$$

To ensure viability of spheroids at day 6, Live-Dead Assay (Thermo Fisher L3224) was assessed for all spheroid conditions. Spheroids were transferred into a 96 well plate and stained with Calcein-AM and ethidium homodimer solution according to the manufacturer's instructions. Spheroid images were taken by using fluorescent microscope (Olympus IX73 equipped with X-Cite 120 LEDmini, Olympus DP80 camera).

4.2.3.4. Drug Treatment and Viability Experiments

Spheroids initiated with 50-100-200 and 500 cells: Before drug treatment, spheroids were counted and seeded onto suspension culture 24 well plates (CELLSTAR 662 102). 100 spheroids/well were seeded accordingly with the following formula:

$$Total\ number\ of\ spheroids = Spheroid\ count \frac{(50\ \mu L)}{50\ \mu L}\ x\ Spheroid\ suspension\ (\mu L)$$

Spheroids were incubated for 30 min. Then, Taxol or Cisplatin were added in concentrations of 100 nM, 1 μM, 10 μM and 100 μM and incubated for 48 h at 37 °C and 5% CO_2. At the end of 48 h, images of the spheroids were taken, and viability was assessed using CellTiter-Glo 3D Cell Viability Assay (Promega G9681). Briefly, plates containing spheroids were equilibrated to room temperature for 30 min, then CellTiter-Glo 3D solution was added on top of the spheroids 1:1 (v/v) and placed on a shaker to induce efficient cell lysis for 5 min before incubation at room temperature for 20 min to stabilize the luminescent signal in accordance with the manufacturer's instructions. Luminescence measurement was carried out with BioTek Neo2SM microplate reader and relative viability was calculated for each spheroid group.

Spheroids initiated with 5000 cells: 100 μl of cell medium was removed, and 100 μl of drug solutions was added to each well and incubated for 48 h. At the end of 48 h CellTiter-Glo 3D assay was performed as described previously. Luminescence measurement was carried out with BioTek Neo2SM microplate reader microplate reader and relative viability was calculated for each spheroid group.

4.2.3.5. Immunocytochemistry

Monolayer cells: OVCAR-3 and OVCAR-8 cells were seeded on glass coverslips in 24 well plate in a density of 20.000 cells/well and incubated overnight for attachment.

Spheroids: OVCAR-3 and OVCAR-8 spheroids were prepared as mentioned before and placed on 24 well plates before staining.

Cells and spheroids were fixed in 4% PFA for 20 min and permeabilized by using 0.5% Triton-X on a shaker for 20 min. Cells and spheroids were then blocked in 3% BSA (Millipore-Sigma A9418) for 1 h at room temperature and stained overnight on a shaker in 1% BSA with Phalloidin-iFluor

555 (Abcam ab176756), E-cadherin (Santa Cruz sc-21791) and Vimentin (Santa Cruz sc-6260). Wells were washed the next day with 1% BSA and incubated for 1 h at room temperature with Donkey Anti-Mouse IgG NorthernLights™ NL493-conjugated Antibody (NL009) in 1% BSA. Wells washed with 1% BSA and coverslips were mounted in ProLong™ Glass Antifade Mountant with NucBlue™ Stain (Thermo Fisher P36981) and stored in dark until imaging.

Imaging was carried out with Leica SP8 Confocal Microscopy System with 63X immersion objective (1.40 NA OilWD 0.14mm HC PL APO) for monolayer cultures and with 40X dipping objective (0.80 NA water U-V-I WD 3.30 mm HCX APO L) for spheroids.

4.2.3.6. Protein Extraction and Quantification

RIPA lysis and extraction buffer (ThermoFisher Scientific 89900) supplemented with halt protease inhibitor (PI) cocktail (ThermoFisher Scientific 78430) is used to obtain protein lysates. Cells were collected by trypsinization, spheroids were collected from plates and washed with cold PBS lysed in freshly prepared RIPA and PI cocktail solution. Lysates were incubated for 15 min on ice and centrifuged at 14,000 *g* for 15 min at 4 °C according to the manufacturer's instructions. Supernatants were collected and quantified with BCA protein assay kit (ThermoFisher Scientific 23225) by measuring the absorbance at 562 nm in accordance with the manufacturer's instructions.

4.2.3.7. Immunoblotting

Reagents. Acrylamide/Bis-acrylamide, 30% solution (Sigma A3699), 1.5 M Tris-HCl, pH 8.8 (Teknova T1588), Tris HCl Buffer 0.5 M solution, sterile pH 6.8 (Bio Basic SD8122), Ammonium persulfate (Sigma A3678), UltraPure 10% SDS (Invitrogen 15553-027), TEMED (ThermoFisher Scientific 17919), Dithiothreitol (DTT) (BIO-RAD 1610610) Tris Base (Fisher Bioreagents BP152),

Glycine (Fisher Bioreagents BP381), 4x Laemmli sample buffer (BIO-RAD 1610747), TWEEN 20 (Sigma P9416), Mini Trans-Blot filter paper (BIO-RAD 1703932), Nitrocellulose Membranes 0.45 m (BIO-RAD 1620115), Western Blotting Luminol Reagent (Santa Cruz sc-2048)

Procedure. Protein samples were diluted in Laemmli buffer and boiled for 5 min at 96 °C. Proteins were then separated by sodium dodecyl sulfate-polyacrylamide gel electrophoresis (SDS-PAGE) gels (8.5%) and transferred to nitrocellulose membranes. After transfer, the membranes were blocked in 5% milk in Tris Buffered Saline with 0.1 % Tween 20 (TBST). Blots were then stained with E-cadherin (Santa Cruz sc-21791), Vimentin (Santa Cruz sc-6260) β-Actin (Santa Cruz sc-47778 HRP), SLUG (Santa Cruz sc-166476) and Vinculin (7F9) (Santa Cruz sc-73614) antibodies in 1% milk in TBST overnight at 4 °C. Membranes were washed the next day in TBST and probed with HRP Goat anti-mouse IgG (minimal x-reactivity) Antibody (BioLegend 405306), washed with TBST. Finally, western blotting luminol reagent solution was added on top of the membranes and chemiluminescence signal was detected by Azure c600 Imaging Biosystems.

4.2.3.8. Migration Assay

Monolayer

OVCAR-3 and OVCAR-8 cells were seeded in 6 well plates and cultured to confluency. Then, by using the tip of a 200 ml pipette tip wound area is formed, and the closure is monitored and quantified for 6, 24 and 48 h.

Spheroid

100 spheroids/well were added on 6 well plates and imaged at t=0 h. Spheroids were imaged again after 6, 24 and 48 h, and the area invaded by the spheroids after these times were quantified using ImageJ.

4.2.3.9. Statistical Analysis

All data was analyzed with GraphPad Prism Version 8.3.0. All data are presented as the means ± standard deviation. Statistical analysis was done by 2-way ANOVA test **** $p<0.0001$, *** $p<0.001$, ** $p<0.01$, * $p<0.1$.

4.2.4. Results

4.2.4.1. Expression of Epithelial-to-Mesenchymal Markers in Monolayers of EOC Cells

Initially, we grew the cells in a monolayer. To understand their cell morphology, we stained EOC cells for their F-actin filaments (red), a main cytoskeletal element. While both cell lines showed a strong presence of F-actin filaments, they were prominent at the membrane periphery in OVCAR-3 cells and distributed uniformly throughout the cytoplasm for OVCAR-8 cells **(Figure 24 left column)**. We then investigated the existence and levels of EMT markers E-cadherin and Vimentin in these monolayers. E-cadherin (green, center column) expression was very low at the cell membrane of OVCAR-3 cells and was not visible in OVCAR-8 cells **(Figure 24, center column)**. E-cadherin is known to interact with cytoskeletal proteins, explaining the observed accumulation of F-actin on the OVCAR-3 cell membrane[298]. Vimentin (green, right column) expression showed an opposite trend: while no Vimentin was observed in OVCAR-3 cells, intermediate filaments were present in the cytoplasm of OVCAR-8 cells **(Figure 24, right column)**. We confirmed these expression profiles with western blotting; however, E-cadherin level was too low to be detected by western blotting for OVCAR-3 cells **(Figure 24)**.

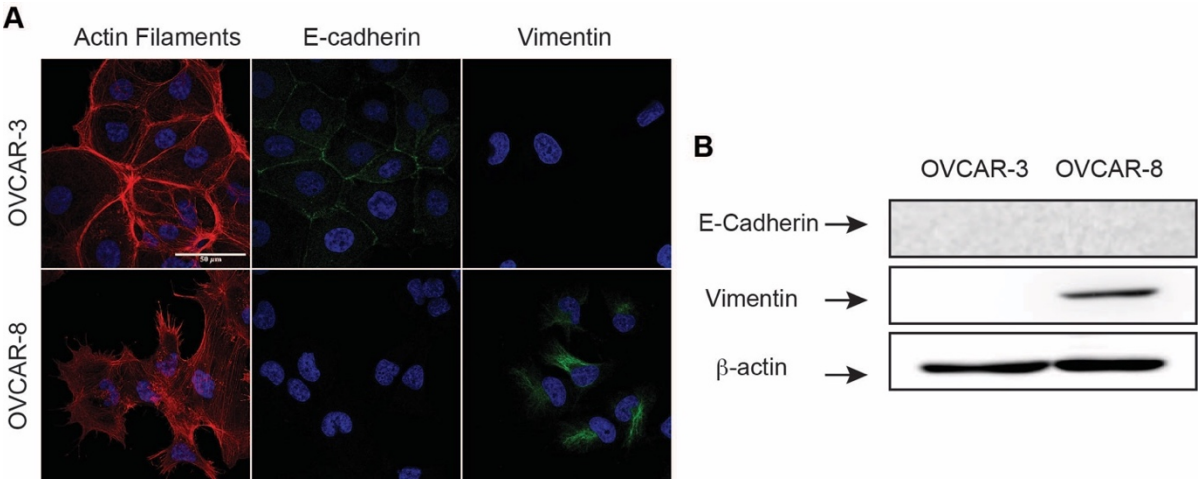


Figure 24. Analysis of EMT markers in OVCAR-3 and OVCAR-8 cell lines. (A) Confocal imaging of actin cytoskeleton (red, left column), E-cadherin (green, center column) and Vimentin (green, right column). Scale bar is 50 μm, and blue staining indicates DAPI (nuclei) in each image. (B) Western blotting of E-Cadherin and Vimentin; and housekeeping β-actin was included for total protein loading control. (C) Illustration of OVCAR-3 and OVCAR-8 in epithelial and mesenchymal phenotype spectrum.

Differences in E-cadherin expression in the patient derived tumors are well documented. E-cadherin expression is generally induced in well differentiated ovarian cancers[299,300]. Hayley et al. studied the functional characterization of several HGSOC cell lines and concluded that the HGSOC cell lines with the highest vimentin expression showed the lowest E-cadherin expression, and vice versa. It is known that the HGSOC cell lines exhibit a wide range of different characteristics, EMT

phenotype, and drug resistance. Such wide range is correlated with the characteristics of the disease in clinic[301].

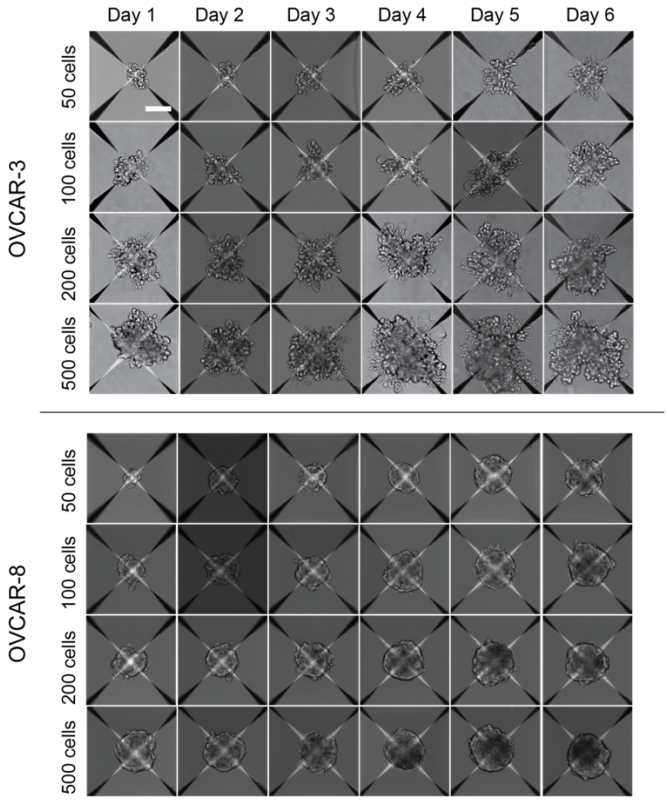


Figure 25 Spheroid formation of ovarian cancer cell lines. OVCAR-3, SKOV-3 and OVCAR-8 spheroids were initiated with 50, 100, 200 and 500 cells and monitored for 6 days every 24h Scale bar is 100 μm.

4.2.4.2. Spheroid Formation and Characterization

We started spheroids with different initial cell numbers to cover a physiologically relevant range over the course of 6 days **(Figure 25)**: Spheroids isolated from patient ascites display a diameter range between 50-750 μm,[297] and necrotic core formation has been shown for spheroids with diameter larger than 500 μm[302]. Therefore, to avoid excessive necrosis we limited spheroid

growth to 6 days to ensure diameters < 500 μm[264,303–305]. Furthermore, because spheroids inside the patient-derived ascites come with a wide range of sizes[281], we also characterized the spheroids with different numbers of initiating cells (50, 100, 200, and 500).

OVCAR-3 cells formed spheroids with loose aggregate morphology **(Figure 26A)**, while OVCAR-8 spheroids were morphologically compact **(Figure 26E)**. Additionally, we assessed spheroid viability at the end of 6 days by using Live-Dead staining. Spheroid-forming cells were all viable (green) with only a few dead cells (red, **Figure 26A and 5E)**. OVCAR-3 loose aggregates grew to almost double their initial size over the course of 6 days **(Figure 26B).** Average diameter on day 6 were 120 μm for 50, 160 mm for 100, 220 μm for 200 and 260 μm for 500 numbers of initiating cells. Interestingly, all OVCAR-8 spheroids reached to a similar size of about 160 μm in diameter on day 6 regardless of initial cell number, a phenomenon observed previously[306,307] **(Figure 26F)**. Further investigation is required to explain why spheroids started with a small number of cells exhibit higher growth compared to spheroids started with larger numbers of cells; this phenomenon will be the focus of another study **(Figure 27)**. Initiation cell number did not affect the spheroid morphology; according to "circularity value" (ranging from 0 to 1 for non-circular to perfectly circular objects),[264] OVCAR-3 spheroids showed circularity between 0.5 and 0.7 **(Figure 26C)** indicating rather loose structures compared to the OVCAR-8 spheroids with average circularity of 0.95 across all spheroid sizes (**Figure 26G)**. This finding is supported by a complementary analysis using "solidity", a measure of surface roughness that also ranges from 0 to 1; cell aggregates with solidity higher than 0.9 are accepted as spherical[308], and OVCAR-3 spheroids displayed solidity between 0.8 and 0.9 **(Figure 26D)** while OVCAR-8 spheroids displayed solidity >0.99 for all spheroid initiation cell numbers **(Figure 26H)**.

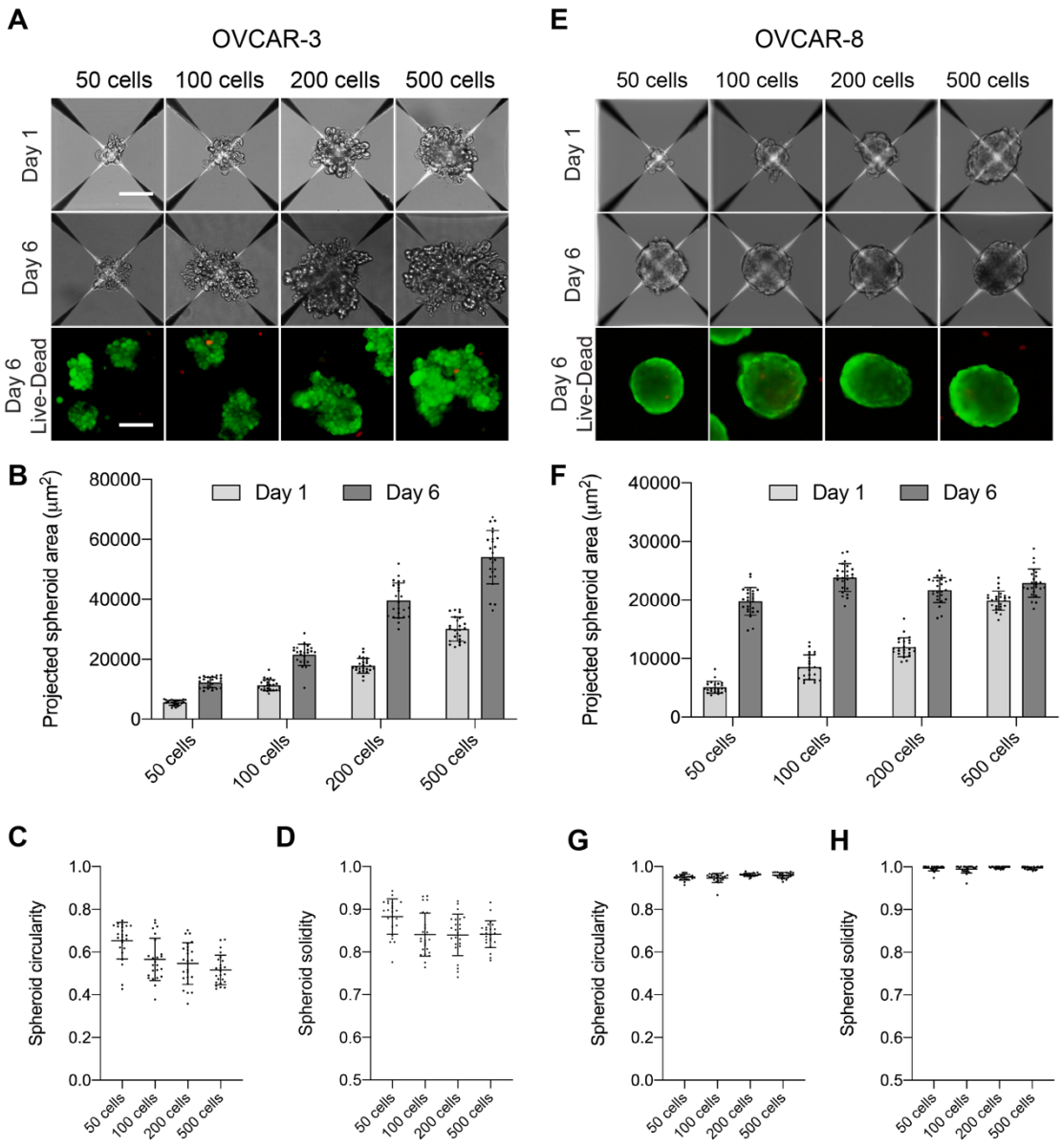


Figure 26. Characterization of OVCAR-3 and OVCAR-8 spheroid formation. (A) OVCAR-3 spheroids were initiated with 50, 100, 200, and 500 cells, and images were taken on day 1 and day 6. (B) Projected surface area characterization of OVCAR-3 spheroids (C) Circularity of OVCAR-3 spheroids at day 6 (D) Solidity of OVCAR-3 spheroids at day 6. (E) OVCAR-8 spheroids were initiated with 50, 100, 200 and 500 cells, and images were taken on day 1 and day 6 (F) Projected surface area characterization of OVCAR-8 spheroids (G) Circularity of OVCAR-8 spheroids at day

6 (H) Solidity of OVCAR-8 spheroids at day 6. For each cell numbers to initiate the spheroids, n=24 spheroids were analyzed by randomly selecting 8 spheroids from 3 independent experiments. Scale bars are 100 μm.

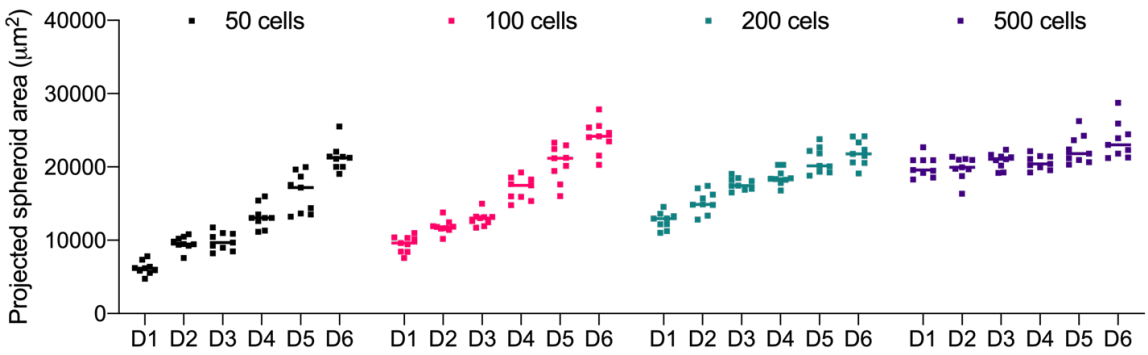


Figure 27 Projected spheroid area of OVCAR-8 spheroids from day 1 to day 6. Area of OVCAR-8 spheroids were measured every day. 3 spheroids per each independent 3 experiments were evaluated.

4.2.4.3. Expression of Epithelial-to-Mesenchymal Markers in EOC Spheroids

The thickness of the 3D spheroid models presents a technical challenge for the standard objectives of a confocal microscope.[309] Therefore, we imaged the OVCAR-3 and OVCAR-8 spheroids with confocal microscopy using a water immersion objective **(Figure 28A)**. Water immersion objectives have lenses designed to image aqueous samples, particularly samples without cover glass. The imaging depth of immersion objectives (5 to 180 μm) is superior to standard objectives[310] and allows optical sectioning[309]. We stained F-actin in the spheroids to better visualize their morphologies **(Figure 28B)**. Confocal images confirmed previous observations of both OVCAR-3 and OVCAR-8 spheroid morphology, while providing a better

understanding of their cell-to-cell interactions. We then investigated the existence and levels of EMT markers E-cadherin and Vimentin in the spheroids. Although OVCAR-3 monolayer E-cadherin expression level was very low in imaging **(Figure 24A)** and could not be detected in western blotting **(Figure 24B)**, we observed highly upregulated E-cadherin in OVCAR-3 spheroids, which we further confirmed with western blotting **(Figure 28C, left column and Figure 28D, top)**. OVCAR-8 spheroids were deficient in E-cadherin **(Figure 28C)** and displayed similar Vimentin expression patterns as their monolayer counterparts **(Figure 28D)**.

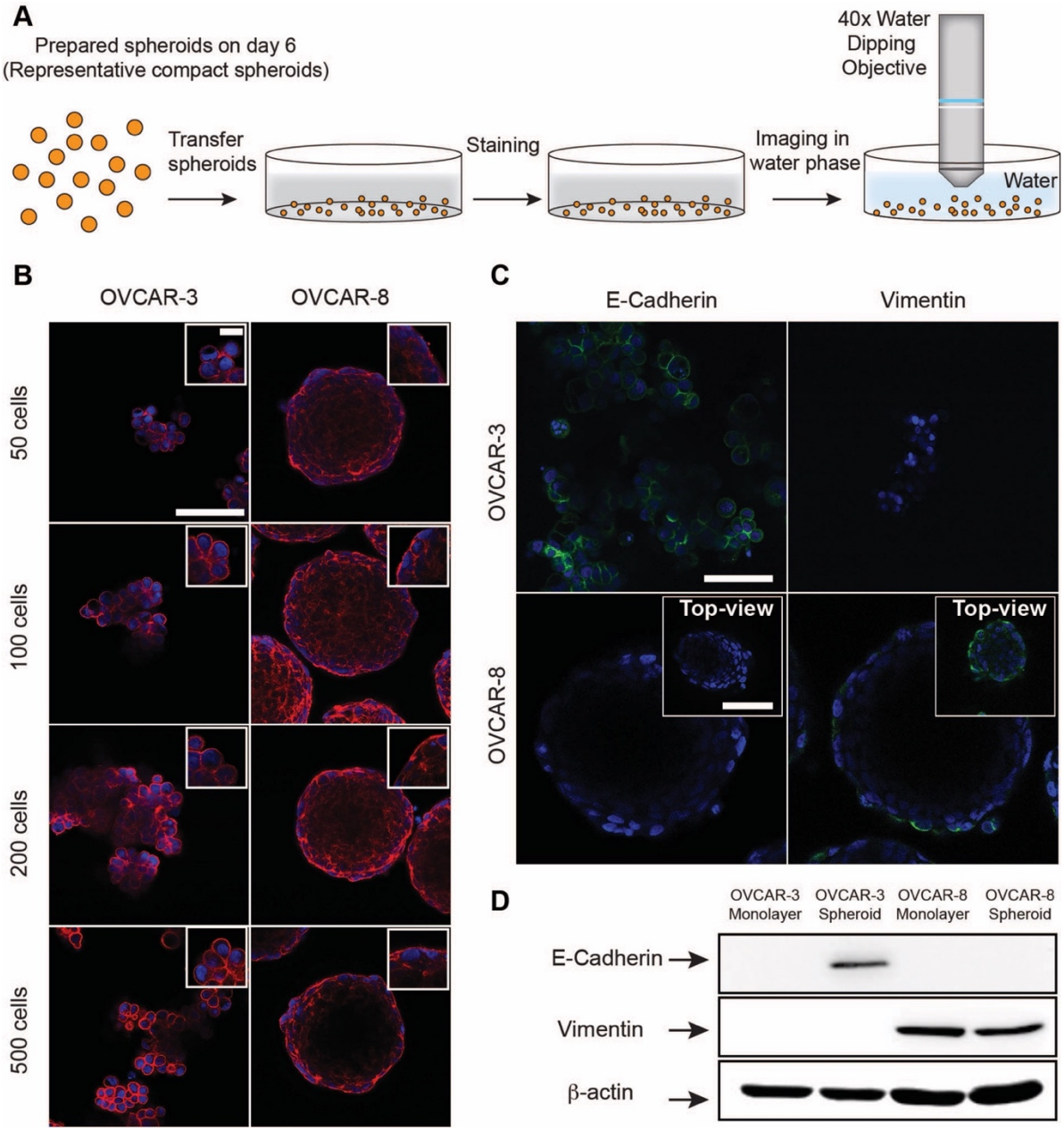


Figure 28. Morphology analysis and epithelial-to-mesenchymal marker expression of ovarian cancer spheroids. (A) Strategy for imaging of spheroids by using water immersion objective. (B) OVCAR-3 and OVCAR-8 spheroids with initiation cell numbers of 50, 100, 200 and 500 were stained for F-actins (red) and DAPI for nuclei (blue), imaged for their morphology. Scale bar is 100 μm. Inset indicates magnified sections from spheroids, scale bar is 20 μm. (C) E-Cadherin (green,

left column), Vimentin (green, right column), and DAPI for nuclei (blue) imaging of OVCAR-3 and OVCAR-8 spheroids with initiation cell number of 200. Top-view panel indicates the top of the OVCAR-8 spheroids, Scale bar is 100 μm. (D) Panel indicates western blot of E-Cadherin and Vimentin from ovarian cancer monolayers and their spheroids (initiation cell number of 200). Housekeeping β-actin was included for total protein loading control.

4.2.4.4. Size and Shape Dependent Cytotoxicity in EOC spheroids

Ascites derived from EOC patients can contain spheroids with different shape and size.[281] However, there is a lack of systematic experimental investigation of the effects of EOC spheroid size and morphology on drug sensitivity. 3D systems might display different cytotoxicity compared to monolayers. Therefore, we compared the cytotoxicity of the anti-cancer drugs on monolayer and 3D spheroids respectively. We carried out a cytotoxicity assay by treating OVCAR-3 and OVCAR-8 monolayers with Taxol and Cisplatin separately, for 48 h. We found Taxol IC_{50} values of 4.217 nM and 7.882 nM for OVCAR-3 and OVCAR-8 respectively, and Cisplatin IC_{50} values of 4.975 μM and 11.397 μM for OVCAR-3 and OVCAR-8 respectively, in agreement with previously published values **(Figure 29)**.

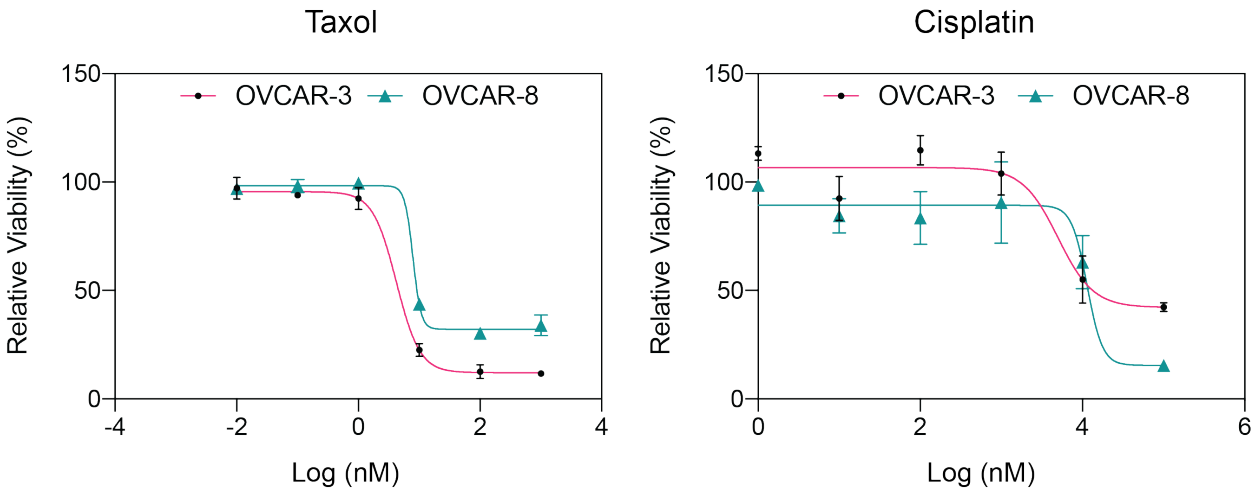


Figure 29 Taxol and Cisplatin treatment of OVCAR-3 and OVCAR-8 monolayers for 48h. Cytotoxicity of Taxol and Cisplatin at various concentrations were analyzed by using Alamar Blue at 48h.

The sizes we observed for OVCAR-3 loose aggregate spheroids ranged from 120 μm (for the initiating cell number of 50) to 260 μm (for the initiating cell number of 500) on day 6. However, for OVCAR-8, we observed the formation of compact spheroids reaching the average diameter of 160 μm on day 6 regardless of the initiating cell numbers. Because the sizes of the spheroids found in patient-derived ascites can reach up to 750 μm[297], to target similar sizes we also introduced spheroids with the initiation cell number of 5000. The spheroids with the initiation cell number of 5000 showed a similar trend in shape to the ones prepared with 50 cells: loose aggregates for OVCAR-3 with an average diameter of 600 μm and compact spheroids for OVCAR-8 with an average diameter of 750 μm **(Figure 30).**

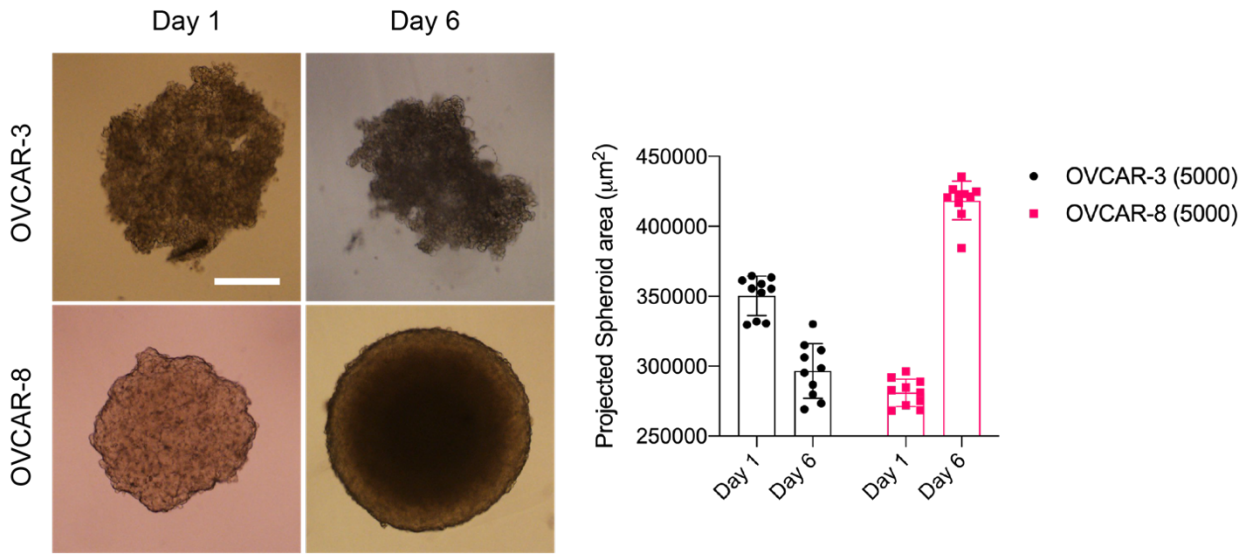


Figure 30 Size analysis of large OVCAR-3 and OVCAR-8 spheroids. OVCAR-3 and OVCAR-8 spheroids were initiated with 5000 cells in U-bottom 96 well plates and monitored for 6 days. Scale bar is 250 μm. 10 spheroids were analyzed.

Similar to the monolayer protocol, we carried out a cytotoxicity assay by treating OVCAR-3 and OVCAR-8 spheroids with Taxol and Cisplatin separately, for 72h. All spheroids showed much increased resistance to Taxol treatment **(Figure 31A and 11B)**. Given Taxol's nanomolar IC_{50} value in monolayer cell culture experiments, we interpret this result as high drug resistance upon spheroid formation. Cisplatin showed toxicity only in concentrations higher than 1 μM in both cell lines in 72 hours **(Figure 31C and 11D)** and the sensitivity of the spheroids were similar in range to their monolayer counterparts. Similar trend was observed also in 48 hours **(Figure 32)**. Size and shape of the spheroids did not have significant effects on the cytotoxicity of Cisplatin, however, increased spheroid size resulted in some level of increased resistance in large spheroids (5000).

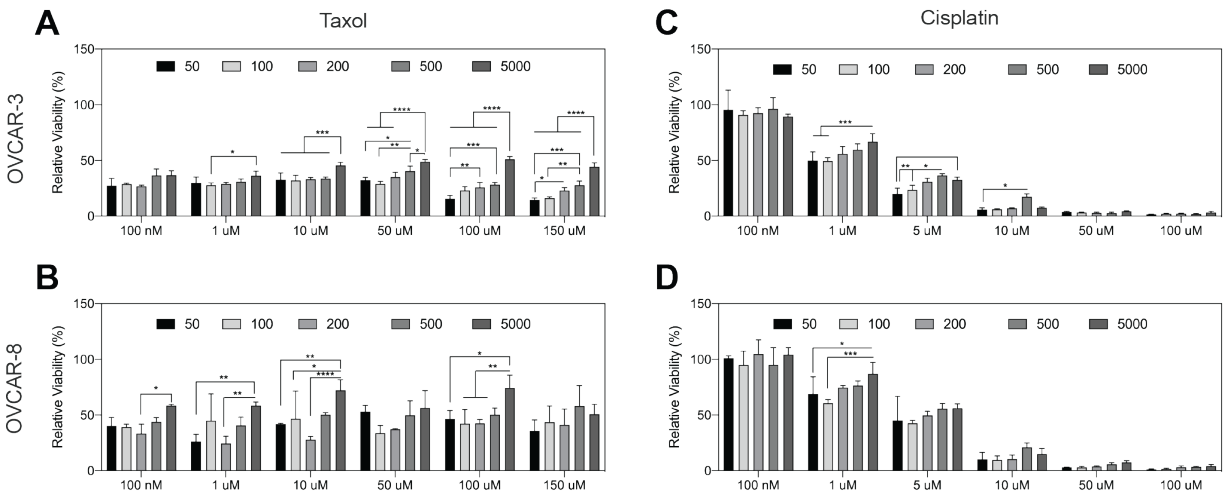


Figure 31. Effect of Taxol and Cisplatin treatment for 72 h on the viability and morphology of the EOC spheroids. (A-D) OVCAR-3 and OVCAR-8 spheroids with the initiation cell number of 50, 100, 200, 500 and 5000 were treated with different concentrations of Taxol and Cisplatin and at 72h viability was measured by CellTiter-Glo3D. Statistical analysis was done by 2-way ANOVA test **** p<0.0001, *** p<0.001, ** p<0.01, * p<0.1.

We looked at the changes in the structures of the spheroids in response to drug treatments under microscope at 48h **(Figure 32E-G)**. Taxol treatment did not have strong impact on the morphology of OVCAR-3 and OVCAR-8 spheroids, and spheroids remained intact with few death cells shed **(Figure 32F)**. However, even though ineffective at low concentrations (100 nM and 1 μM), Cisplatin significantly disrupted spheroid morphology 100 μM **(Figure 32G)**.

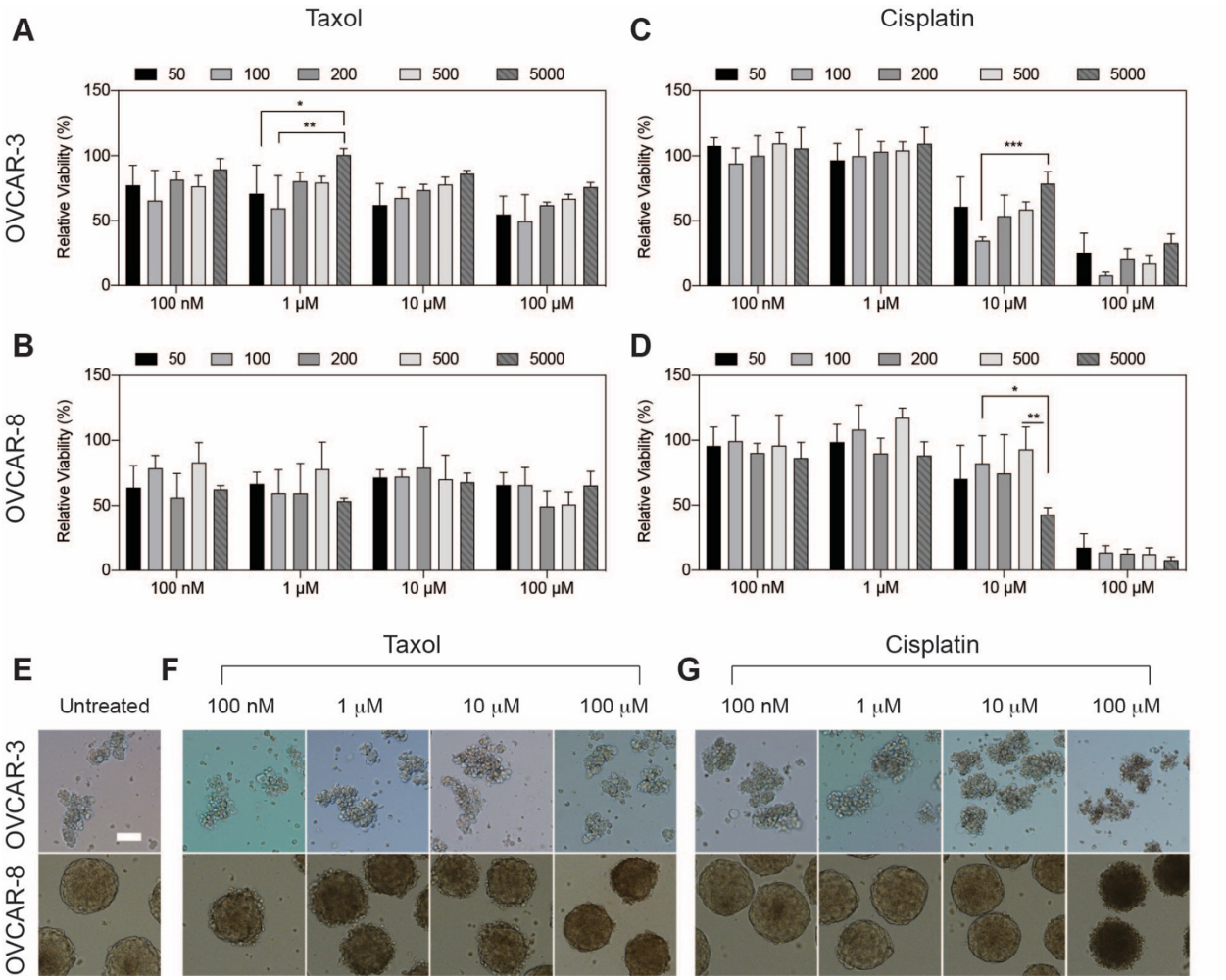


Figure 32 Effect of Taxol and Cisplatin treatment for 48 h on the viability and morphology of the EOC spheroids. (A-D) OVCAR-3 and OVCAR-8 spheroids with the initiation cell number of 50, 100, 200, 500 and 5000 were treated with different concentrations of Taxol and Cisplatin and at 48h viability was measured by CellTiter-Glo3D. (E-G) Images represent the spheroids with the initiation cell number of 200. Scale bar is 100 μm. Statistical analysis was done by 2-way ANOVA test *** $p<0.001$, ** $p<0.01$, * $p<0.1$.

4.2.4.5. Migration Profiles of EOC Spheroids

The expression of Slug protein (a main transcription factor activated during EMT) is correlated with a more invasive phenotype in EOC[311]. We analyzed the expression of Slug both in OVCAR-3 and OVCAR-8 monolayer cells, and their spheroids (initiation cell number of 200), with western blot. Both OVCAR-3 monolayer cells and spheroids were Slug deficient, while OVCAR-8 monolayer cells and spheroids express Slug **(Figure 33A)**. This observation suggests that OVCAR-8 cells could exhibit higher migration compared to OVCAR-3 cells. We tested this hypothesis first by monitoring the migration profiles of these two cell lines in monolayers with a wound closure assay. We created gaps between cells after they reached total confluency on the surface, and quantified how fast they close these gaps (**Figure 33B**). Both cell lines started to close the area within 24 h, and at 48h OVCAR-8 cells closed nearly 2-fold more area than OVCAR-3 cells (**Figure 33C**), indicating higher migration behavior of OVCAR-8. Then, we investigated the migration profiles of the spheroids, by seeding spheroids (initiation cell number of 200) on day 6 on bare surfaces of 6-well plates and quantified how fast they spread at different time points **(Figure 33D)**. Interestingly, despite their loose morphology, OVCAR-3 spheroids remained intact and only started to attach and migrate the surface at 48 h after seeding, whereas the intact spheroids of OVCAR-8 started to migrate on the surface as early as 6 h **(Figure 33E)**. Migration areas covered by the OVCAR-8 spheroids were significantly higher than that of the OVCAR-3 spheroids, nearly 13-fold and 16-fold larger at 24 h and 48 h, respectively **(Figure 33F)**.

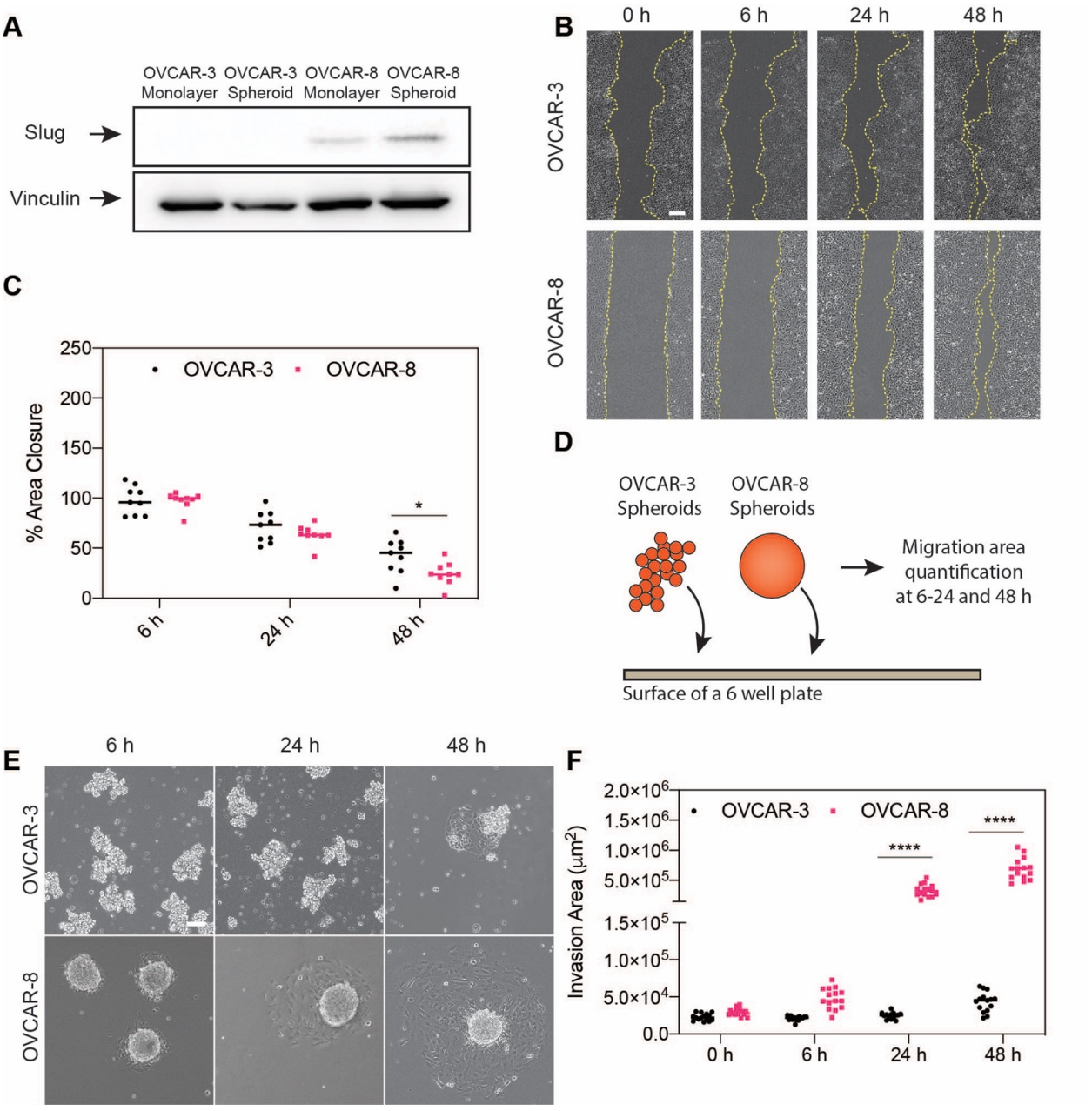


Figure 33. Migration assays. (A) Expression of the transcription factor Slug was analyzed using western blot in OVCAR-3 and OVCAR-8 both as monolayer cells and as spheroids (initiation cell number of 200). Housekeeping vinculin was included for total protein loading control. (B) Wound closure of OVCAR-3 and OVCAR-8 monolayers at 6 h, 24 h and 48 h. Scale bar is 200 μm, (C) Area closure was quantified from a total of 9 different regions for both cell lines. (D) Schematic

depiction of the migration assay for spheroids. (E) 6-days old OVCAR-3 and OVCAR-8 spheroids were plated on the 6-well plates and imaged at 6-24 and 48 h after seeding. (F) Area of the spheroids and migration area was quantified at 6-24 and 48 h using ImageJ. Scale bar is 100 μm. Total of 15 spheroids were analyzed from each group by randomly choosing 5 spheroids from 3 independent experiments. Statistical analysis was done by 2-way ANOVA test, **** $p<0.0001$, * $p<0.1$.

4.2.5. Discussion

Spheroid formation within the peritoneal cavity of the patients is a hallmark of advanced-stage ovarian cancer. Spheroids found in patient-derived ascites come in a wide range of sizes[281], from 50 to 750 μm [297]. In addition to size, distinct morphologies of loose aggregates and tight spherical aggregates have been reported even within the ascites of the same patient[282]. In the present study, we characterized the OVCAR-3 and OVCAR-8 epithelial ovarian cancer cell lines (chosen for their established genetic similarity to the patient tumor samples)[312] using both monolayers and spheroids. We formed spheroids with different initiation cell numbers (50, 100, 200, and 500) to account for the wide range of spheroid sizes in patients; however, spheroid morphology did not differ as a function of initiation cell number for the same cell line. OVCAR-3 spheroids displayed loose aggregate morphology, whereas OVCAR-8 spheroids were more compact, more circular, and exhibited higher solidity. On day 6 after spheroid initiation, spheroids of both cell types were composed almost entirely of viable cells and OVCAR-8 spheroids seeded with 50, 100, 200, and 500 cells all attained roughly the same size (**Figure 25F**).

It is often reported that 3D systems display greater resistance to anti-cancer drugs[313]. Taxol, cisplatin and their combination has been widely used in ovarian cancer,[314–316] with their IC_{50} values on various cancer cell lines extensively studied. In the literature, ovarian cancer cells have IC_{50} values at nanomolar range for Taxol[314,317,318], and micromolar range for Cisplatin[317,319]. Our IC_{50} results for monolayer cell cultures were in strong agreement with the literature. For the IC_{50} estimations in spheroids, using the same spheroid formation technique to avoid its potential effect on drug toxicity[305], we added a larger sized spheroid (initiation cell number of 5000), because OVCAR-8 spheroids reached to similar sizes when initiated with 50, 100, 200, and 500 cells. We measured viability using an ATP-based assay (CellTiter-Glo3D), as colorimetric assays fail to represent viability in 3D models[320]. For both Taxol and Cisplatin, no difference in resistance was observed for different sizes within a particular concentration for 48h. Large spheroids (5000) showed increased resistance to Taxol at 72h. However, spheroids displayed much higher resistance to Taxol compared to monolayers, whereas resistance to Cisplatin was similar for both monolayers and spheroids (in accordance with previous observations)[321]. The toxicity mechanism of Taxol is inhibiting cell division through the inhibition of cytoskeletal proteins[322]. Because the cell proliferation rate slows down in 3D systems, the toxicity of Taxol diminishes. On the other hand, cisplatin toxicity was not dramatically different in monolayer and 3D, which might be because of its DNA crosslinking cytotoxicity mechanism[323].

Previous studies suggested that E-cadherin accumulation on the cell surface inhibits the formation of morphologically compact spheroids[287]. Therefore, we investigated the expression levels of E-cadherin in our cell lines both as monolayers and as spheroids. Monolayer cell culture of OVCAR-3 exhibited very low expression of E-cadherin. Strikingly, E-cadherin expression was

highly upregulated during spheroid formation in OVCAR-3 cells which explains their loose aggregate morphologies. By contrast, OVCAR-8 cells were negative for E-cadherin both in monolayer and spheroid forms. A reduced E-cadherin level is often reported in malignant epithelial tumors,[324] and this downregulation is suggested as a potential mechanism for shed EOC cells to survive anoikis, a programmed cell death induced by cell detachment from the extracellular matrix (ECM) under the anchorage-independent conditions of the abdominal cavity. Anoikis avoidance allows spheroids to adhere to and invade the mesothelium lining, leading to metastasis[325]. Downregulation of E-cadherin is one of the key features of EMT[284], together with the upregulation of Vimentin[290]. We allocated the OVCAR-3 and OVCAR-8 spheroids on an EMT spectrum based on their E-cadherin and Vimentin expressions[325,326]. In line with previous observations, OVCAR-3 spheroids were positive for E-cadherin expression and negative for Vimentin expression (epithelial), whereas OVCAR-8 spheroids were negative for E-cadherin and positive for Vimentin expression (mesenchymal) **(Figure 28)**[277,301,327].

Increased migratory phenotype was previously shown to correlate with upregulation of mesenchymal genes in EOC cell lines and human samples[328]. During the advanced-stages of cancer, EMT is regulated by several transcription factors, such as Snail, Slug and Twist, leading to an increased progression of the disease[329–331332,333]. In particular, overexpression of slug is reported to correlate with the invasiveness of ovarian cancer[311,334]. We examined the expression of slug in our EOC monolayer cells and their spheroids and found that OVCAR-3 monolayers and spheroids were deficient of slug, whereas OVCAR-8 monolayer and spheroids expressed slug, supporting OVCAR-8's mesenchymal phenotype. We then quantified migration profiles and, in line with previous observations[328,335], OVCAR-8 spheroids displayed nearly 13 fold (24 h) and 16

fold (48 h) increased migration area compared to OVCAR-3 spheroids. It should be noted, however, that the high migratory phenotype of cancer cells is also orchestrated by proteins such as CD44[335] and transcription factors such as twist[329] and snail[330,334] in addition to E-cadherin, Vimentin and Slug.

In conclusion, the two distinct morphologies we observed here (loose aggregates and compact spheroids) are clinically relevant because both spheroid morphologies are present in samples isolated from the same patient[281]. Here we showed how these spheroid morphologies are associated with the expression levels of the EMT markers E-cadherin and Vimentin, and the transcription factor Slug. Spheroids displayed size-independent resistance against Taxol, which can be explained by increased mesenchymal like gene expression in ovarian cancer spheroids[336]. Spheroids also displayed size-independent resistance against Cisplatin, and Cisplatin was observed to have similar cytotoxicity for both monolayers and spheroids - a phenomenon observed before[337–339]. These results therefore significantly enhance our understanding of the relationship between spheroid size/morphology and drug resistance. In addition, we also showed how the expression levels of these markers correlate with the migration potential of the EOC spheroids. Previous studies have provided conflicting descriptions of the impacts of the changes in the expression of EMT-related molecules in EOC progression and dissemination[293,294], and further analyses are required to elucidate the specific roles of EMT markers in orchestrating the observed invasive phenotypes; for example, a mesothelial clearance assay with several knock-out EOC cell lines for specific EMT markers would provide a more detailed understanding of this process. We note that *in vivo* experiments might result in different drug response and protein levels because of the complex structure of xenografted samples. Nonetheless, our results provide

an insight into the effects spheroid size variation on chemotherapeutics, and spheroid morphology on migratory profiles for *in vitro* studies.

4.3. [II] aggregation-induced ICD in breast cancer spheroid model

This section is adapted from the following publication which is in preparation:

Gokhan Gunay, Seren Hamsici, Filipa Carvalho, Handan Acar* Peptide aggregation-induced immunogenic cell death in breats cancer spheroid model (in preparation)

4.3.1. Introduction

Inducing cell death has been the primary goal of the treatment strategies against cancer for decades. However, emerging results show that the type of cell death dictates the progression of the tumor. For example, induction of apoptosis within the tumor microenvironment (TME) leads to suppression of the immune system, increased proliferation of cancer cells, and reduced inflammation, all of which increase the progression of cancer[340]. Immunogenic cell death (ICD), on the other hand, results in secretion, release, or surface expression of damage-associated molecular patterns (DAMPs), natural adjuvants capable of engaging the immune system.[17] Moreover, ICD leads to the release of tumor-associated antigens and promotes the initiation of antigen-specific adaptive immunity.[341] Different techniques induce ICD and DAMP release, such as; chemotherapeutics[75], photothermal therapy[148], radiation therapy[342], and recently introduced by our group, the peptide-aggregation model.[343] The concept of ICD and DAMP release is predominantly studied in monolayer cultures. However, monolayer culture does not represent the complexities of in vivo tumors, and animal models are expensive and, for long term, ultimately delay the test of new therapeutics that might be effective.[344] Utilizing tumor spheroids

offers a bridge between in vitro and in vivo models to provide a physiologically relevant, cost-effective, and high throughput model.

Spheroid models offer physiological relevance to in vivo solid tumors in cell to cell interaction, cell to extracellular matrix interaction, drug resistance, and zone formation due to reduced nutrient and oxygen diffusion.[345] Spheroid models exhibit different gene expression profiles compared to their monolayer counterparts.[346] These differences ultimately affect the biological outcomes, one of which is cell death. For example, a recent study showed the apoptotic resistance of breast cancer spheroids against paclitaxel and doxorubicin treatment and found changes in the expression of caspases resulting in an "anti-apoptotic" state.[347] Increased autophagy in breast cancer spheroids reduced the activity of Trastuzumab, making spheroid resistant.[348] Another study showed that spheroids were resistant to ferroptosis (a form of regulated necrosis) induction compared to monolayer counterparts.[349] These efforts highlight the importance of having physiologically relevant models to study and pre-select new therapeutics for treatments.

Aggregation of proteins/peptides such as Aβ is a common hallmark of neurodegenerative conditions such as Alzheimer's, Huntington's, and Parkinson's diseases. Amyloid aggregation was shown to induce inflammation, which recently was linked to DAMPs. Damaged/dying cells due to aggregation activate local immune cells like astrocytes and microglia through the release of DAMPs.[117] Inspired by the amyloid aggregation, we recently established a platform called CoOP[145] to induce ICD and DAMP release. We showed that a peptide pair called [II] (PAIIR) induces ICD and DAMP release in multiple cell lines and elevates the antibody (humoral) response in an influenza vaccination model[343]. Then we showed that [II] aggregation occurs on the cell

membrane and involves the phosphorylation of eIF2α and surface localization of CRT, hallmarks of ICD.[54] Furthermore, we showed that the aggregation state of [II] peptide could be controlled using albumin, resulting in ICD upon the aggregated state while remaining non-cytotoxic in fibrillar form. Consequently, control over the aggregation state equals control over ICD and DAMP release and provides an advantage over modulating the cell death within the same peptide concentration.

Here, we used a breast cancer spheroid model to study ICD and DAMP release. We showed that [II] aggregation induces ICD and DAMP release in the spheroid model. The release of DAMPs was superior to mitoxantrone (ICD inducer) and cisplatin (non-ICD inducer) in terms of type and amount. Furthermore, released DAMPs upon [II] aggregation activated dendritic cells (DCs) into a pro-inflammatory phenotype. Overall, this study uses spheroid models to study ICD and DAMP release and highlights the superiority of the peptide aggregation model against commonly utilized chemotherapeutics.

4.3.2. Results and Discussion

4.3.2.1. Spheroid formation of EMT6 cells

EMT6 is a breast cancer cell line, and it is shown to be an immunogenic cell line.[350] We used the EMT6 breast cancer cell line to form spheroids. Multiple techniques exist to form spheroids, such as ultra-low attachment, hanging drop, magnetic levitation, and spinner flasks.[351] We previously showed the formation of different-sized spheroids by using the ultra-low attachment technique.[352] Here, we used the same technique to form spheroids. The formation of hypoxic core (necrotic core) is associated with drug resistance[353], consequently, one of our criteria was to form large spheroids (>500 μm in diameter), as spheroids larger than 500 μm in diameter

exhibit gradient formation and eventually lead to zone formation.[354,355] Here, we formed and characterized the growth of spheroids and used them on day 7, where their sizes were around 800 mm in diameter **(Figure 34A and B)**. Spheroid surface area increased over time **(Figure 34C)**, and spheroid displayed high circularity **(Figure 34D)** and solidity **(Figure 34E)** throughout the culture period.

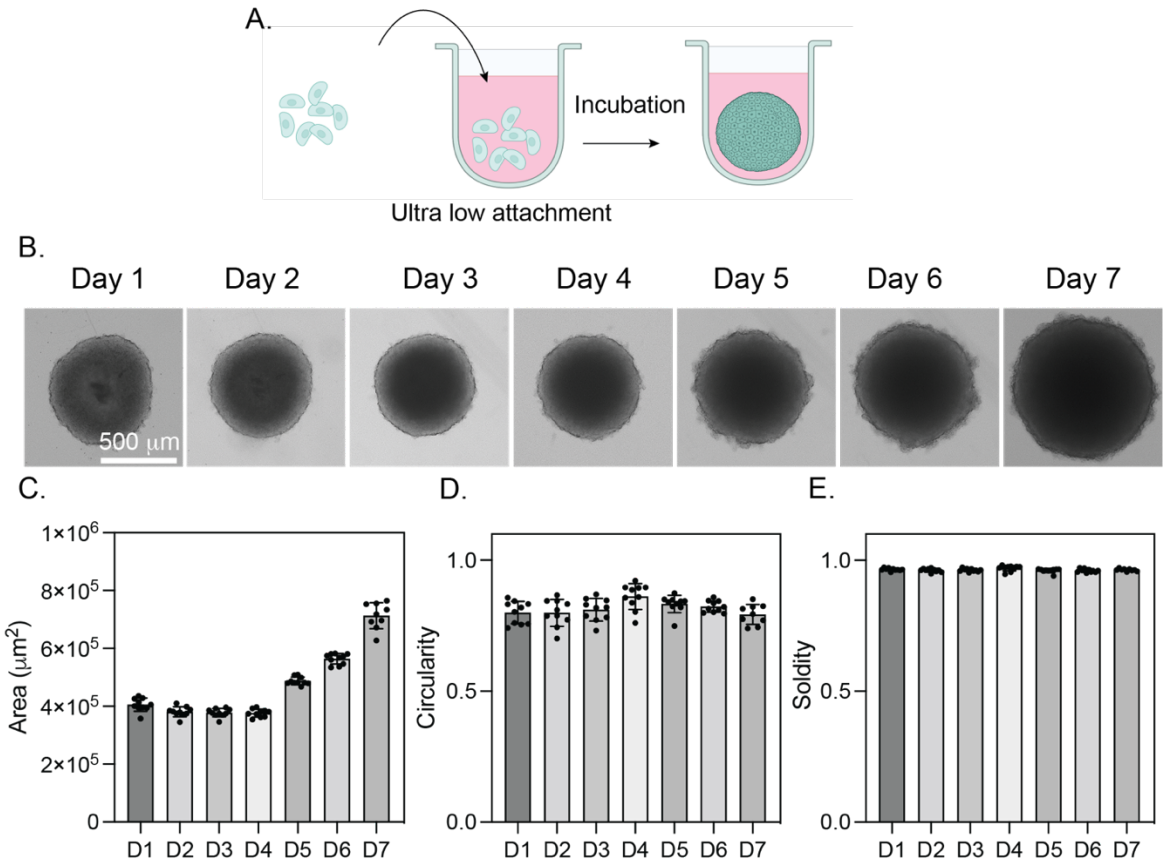


Figure 34 EMT6 spheroid formation and characterization. A. Schematic explanation of ultra-low attachment spheroid formation. B. Representative brightfield images of EMT6 spheroids for 7 days. C. Spheroid area, D. Circularity, and E. Solidity of spheroids for 7 days. The scale bar is 500 μm.

4.3.2.2. [II] peptide aggregation induces cell membrane damage in spheroids

ICD and DAMP release are studied in monolayer cultures, while 3D tumor spheroid models remain largely unexplored. Given that spheroid models offer a better representation of in vivo tumor models in terms of drug resistance, we analyzed the induction of ICD and DAMP release in the EMT6 spheroid model. We previously showed that the aggregation status of [II] peptide could be controlled with albumin. The presence of albumin within the solution prevented early assembly and fibrillization of oppositely charged peptides. This allows time for peptides to aggregate on cell membranes (Cite AichE paper). To analyze the cell death within the spheroids, we treated EMT6 spheroids on day 7 with varying [II] peptide concentrations, prepared in weight %: 1%-0.5%-0.25%-0.125%-0.0625% albumin at 24h. 1 mM and 0.75 mM [II] peptide was not significantly cytotoxic **(Figure 35A and B)**.

This is due to a higher peptide to albumin ratio leading to faster organization into fibrillar structures (non-cytotoxic) analyzed through thioflavin T assay in 1% albumin. ThT assay is commonly utilized to detect b-sheet structures during amyloid fibrillization.[356] An increase in intensity equals higher b-sheet structures indicating higher fibrillization[356]. We previously showed that [II] aggregation, not fibrillization, induces ICD. Highest cytotoxicity was achieved with 0.5 mM, 0.75 mM and 1 mM peptide in 1%, therefore, we analyzed the ThT intensities of these [II] peptide concentrations prepared in 1% albumin. ThT intensity and cell death profile were inversely correlated. Higher intensity values were detected as the peptide concentration increased **(Figure 35G)**, indicating higher levels of fibrillization (non-cytotoxic). Therefore, within a given concentration of albumin (e.g., 1%), increasing peptide concentration would result in a

higher fibrillization state (non-cytotoxic), while lowering peptide concentration would result in aggregation-induced ICD **(Figure 35H)**.

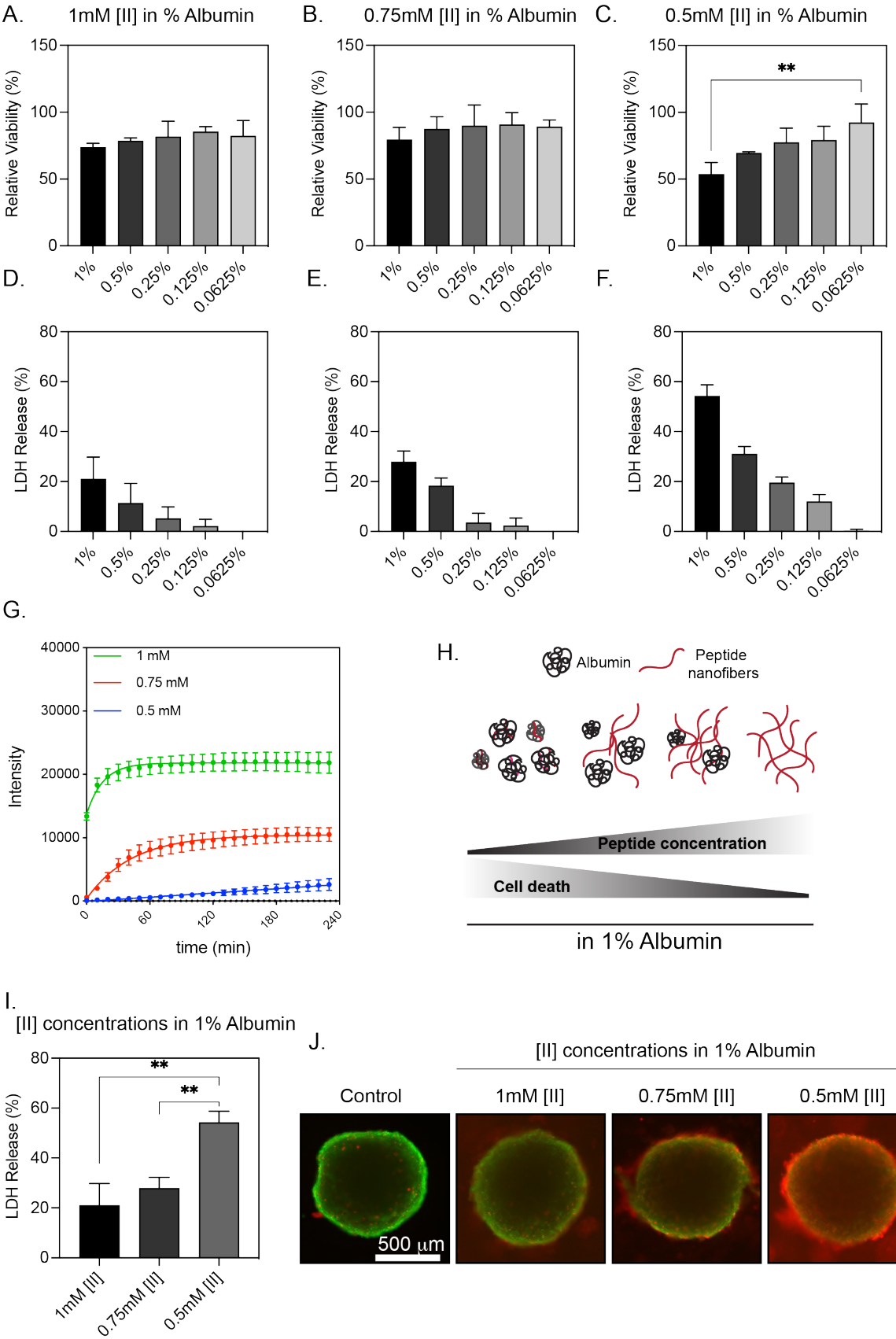

A.
1mM [II] in % Albumin
B.
0.75mM [II] in % Albumin
C.
0.5mM [II] in % Albumin
Relative Viability (%)
150
100
50
0
**
1%
0.5%
0.25%
0.125%
0.0625%
D.
E.
F.
LDH Release (%)
80
60
40
20
0
G.
1 mM
0.75 mM
0.5 mM
Intensity
40000
30000
20000
10000
0
0
60
120
180
240
time (min)
H.
Albumin
Peptide nanofibers
Peptide concentration
Cell death
in 1% Albumin
I.
[II] concentrations in 1% Albumin
**
**
1mM [II]
0.75mM [II]
0.5mM [II]
J.
[II] concentrations in 1% Albumin
Control
1mM [II]
0.75mM [II]
0.5mM [II]
500 µm

Figure 35 [II] aggregation induces controllable membrane damage in the EMT6 spheroid model. Relative viability measurements of A. 1 mM, B. 0.75 mM, and C. 0.5 mM [II] peptide prepared in different albumin concentrations at 24h. LDH release measurements of D. 1 mM, E. 0.75 mM, and F. 0.5 mM [II] peptide prepared in different albumin concentrations at 24h. G. ThT measurement of 1 mM, 0.75 mM, and 0.5 mM [II] peptide prepared in 1% albumin. H. Schematic showing the transition from aggregated state to fibrillar structure with increasing peptide concentration. I. Comparison of LDH release of 1 mM, 0.75 mM, and 0.5 mM [II] peptide prepared in 1% albumin. J. Representative calcein (green) and propidium iodide (red) images of spheroids treated with 1 mM, 0.75 mM, and 0.5 mM [II] peptide prepared in 1% albumin. Statistical analysis was done with a one-way ANOVA test; data are mean ± SD, **p<0.01. The scale bar is 500 μm.

Among the groups studied, 0.5 mM [II] peptide in 1% albumin induced significant (**p<0.01) cell death within the spheroids **(Figure 35C)** at 24h. Next, we checked the release of lactate dehydrogenase (LDH), a cytoplasmic enzyme released upon cell membrane damage[187], to ensure [II] induces cell membrane damage within the spheroids. All [II] concentrations induced the release of LDH, indicating the aggregation kinetics changes the amount of cell death, not the type of cell death. This result also shows the controllability of cell death within the spheroid by modulating the aggregation of the peptide. LDH release was highest with 0.5mM [II] prepared in 1% albumin **(Figure 35I)**, in line with the viability experiments.

We then compared the LDH release from spheroid treated with 1 mM, 0.75 mM, and 0.5 mM [II] peptide in 1% albumin. 0.5 mM [II] peptide-induced significantly (**p<0.01) higher LDH release compared to other conditions **(Figure 35J)**. Additionally, we imaged the [II] peptide-treated spheroids by staining the treated spheroids with calcein (live cells, green) and propidium iodide

(membrane damaged cells, red). Spheroids treated with 0.5 mM [II] in 1% albumin had the highest propidium iodide uptake indicating membrane damage, similar to viability assay and LDH measurements. These results indicate that [II] induces membrane damage within the EMT6 spheroids, controllable through albumin.

4.3.2.3. EMT6 spheroids are resistant to chemotherapeutics

Induction of ICD within the TME is critical for initiating antigen-specific adaptive immunity and protection. Chemotherapeutic drugs have been extensively studied for their capacity to achieve protective immunity through ICD and DAMP release.[32,46] Mitoxantrone and cisplatin are widely studied as an ICD inducer and non-ICD inducer[83], respectively. We aimed to compare the efficacy of [II] aggregation-induced ICD and DAMP release with well-studied controls for cell death. We identified 0.5 mM [II] peptide in 1% albumin induces around 50% cell death **(Figure 35C)**. We wanted to compare the effects of [II] peptide with the chemotherapeutics at a similar spheroid death (%); therefore, we determined IC_{50} values of chemotherapeutics in the spheroid model. To show that spheroid models represent the drug resistance behavior of solid tumors, we treated both monolayer and spheroid cultures of EMT6 with different concentrations of mitoxantrone and cisplatin and determined IC_{50} values. Mitoxantrone had an IC_{50} value of 1.382 μM for monolayer culture and 47.31 μM for spheroid culture **(Figure 36A and B)**. In comparison, cisplatin had 14.32 μM for monolayer culture and 28.49 μM for spheroid culture **(Figure 36A and B)**. Resistance of spheroids to chemotherapeutics has been shown by us[352,357] and others[358–360] before. Here, we showed that EMT6 spheroids are resistant to mitoxantrone and cisplatin. These results showed that spheroid models exhibit the drug resistance aspect of in vivo tumors and offer a high-throughput platform for studying new therapeutics.

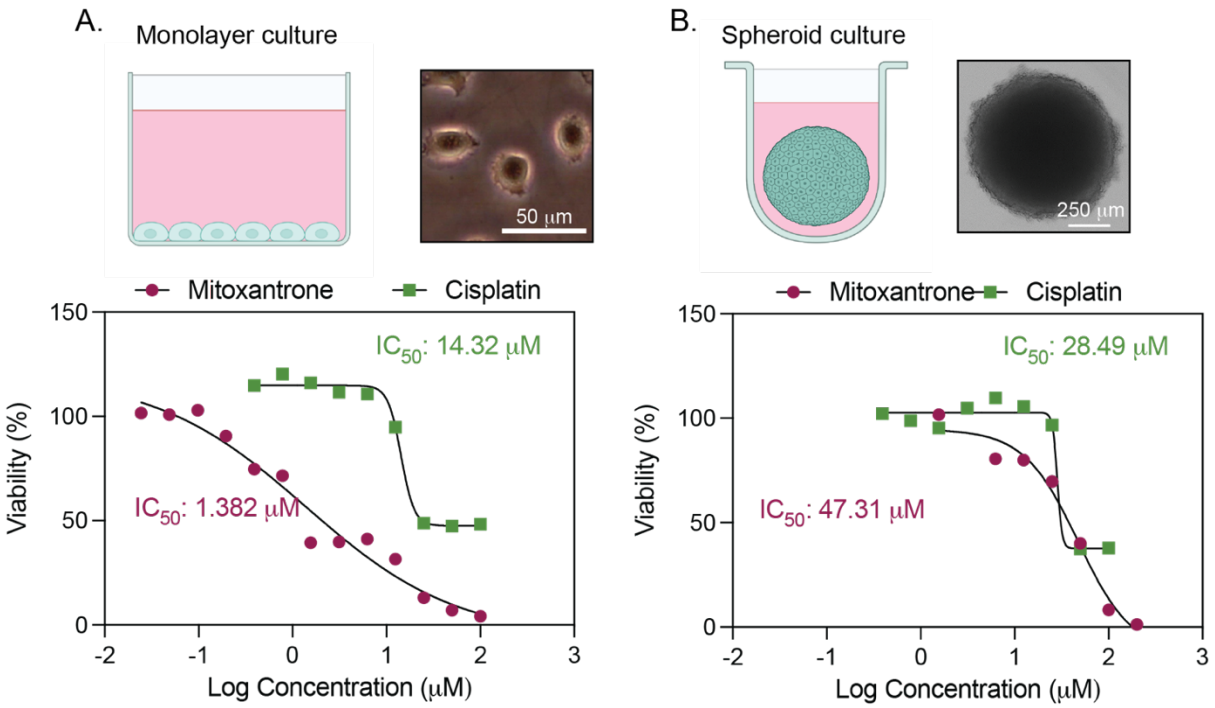


Figure 36 IC_{50} values of chemotherapeutics in monolayer and spheroid culture. A. IC_{50} values of mitoxantrone and cisplatin on monolayer culture at 24h. The scale bar is 50 μm. B. IC_{50} values of mitoxantrone and cisplatin on spheroid culture at 24h. The scale bar is 250 μm.

Determining the concentration for chemotherapeutic drugs is vital because, when they are systemically administered, they have severe side effects.[361] One of the most significant limitations is the low chemotherapeutic concentrations accumulating in solid tumors. Therefore, recent efforts focus on local delivery of chemotherapeutics rather than systemic administration.[361] However, within the TME, multiple factors contribute to the drug resistance, one of which is the upregulation of anti-apoptotic genes.[362] On the contrary, the peptide aggregation model we engineered does not target a specific receptor to initiate ICD and DAMP

release; therefore, it presents a unique model to overcome acquired resistance against chemotherapeutics.

4.3.2.4. [II] aggregation-induced DAMP release is superior to chemotherapeutics

DAMPs have been proven necessary for the immunogenicity of dying cells.[46,51,363] We previously showed [II] aggregation-induced ICD and the release of DAMPs on different cell lines.[343] We treated EMT6 spheroids on day 7 for 24h with 0.5 mM [II] peptide in 1% albumin, mitoxantrone 50 mM, and cisplatin 30 mM (near their 50% cell death concentrations for all conditions) and compared the DAMP release profiles. LDH release was significantly (****$p<0.0001$) higher in [II] peptide and mitoxantrone treated spheroids compared to cisplatin **(Figure 37A)**, indicative of membrane damage. Next, we analyzed the supernatant of spheroids after 24h treatments for the release of DAMPs. A diverse set of molecules are released upon ICD. The following DAMPs have been shown to contribute to the activation of immune cells: extracellular ATP, nucleic acids, and HMGB-1. Extracellular release of ATP acts on purinergic receptors[22] on DCs to secrete IL-1β and activate tumor antigen-specific CD8+ T cells, an effect abolished in the absence of purinergic receptors.[20] We detected significantly (****$p<0.0001$) higher extracellular ATP upon [II] treatment compared to chemotherapeutics **(Figure 37B)**. Mitoxantrone has been shown to induce ATP by some groups[74,76], while others did not detect ATP release at high concentrations.[75] We did not detect ATP release upon mitoxantrone treatment **(Figure 37B)**. The concentration of chemotherapeutics changes their induction of ICD and DAMP release profiles[75], therefore, not observing extracellular ATP could be due to the concentration used in our study.

Pattern recognition receptors (PRRs), such as toll-like receptors (TLRs) on immune cells, are specialized to detect different “patterns,” including nucleic acids, critical for inducing an antiviral

immune response against DNA and RNA viruses.[364] Nucleic acids initiate a robust type I interferon response, crucial for anti-tumor immunity.[365] Specifically, double-stranded DNA (dsDNA) has been shown to increase the expression of genes in DCs responsible for antigen processing and presentation.[366] We detected significantly higher dsDNA release upon [II] treatment compared to chemotherapeutics **(Figure 37C)**. Cisplatin also induced dsDNA release, possibly due to its role in inducing double-strand DNA breaks.[367] HMGB-1 is a nuclear protein released in ICD. Extracellularly, it can engage TLR4 and receptor for advanced glycation end products (RAGE) and stimulate pro-inflammatory cytokine production.[25] We detected higher levels of HMGB-1 in the extracellular matrix of spheroids treated with [II] compared to chemotherapeutics **(Figure 37D)**. Together, [II] aggregation-induced the release of ATP, dsDNA, and HMGB-1 **(Figure 37E)** and was superior in terms of type and amount to chemotherapeutic drugs.

The effects of individual DAMPs on immune cells and their receptor interactions have been studied extensively. However, recent studies highlight the synergistic effects of DAMPs on the activation of immune cells. Silencing HMGB-1 only partially reduced the protective capacity of oxaliplatin-induced ICD in a prophylactic vaccination model.[46] The presence of ATP and HMGB-1 release in the early stage of ferroptosis was protective, while depletion of ATP at the late stage abolished this protection in a prophylactic vaccination model.[51] Given that DAMPs act synergistically, [II] aggregation-induced DAMP release profile is promising for activating innate immune cells such as DCs.

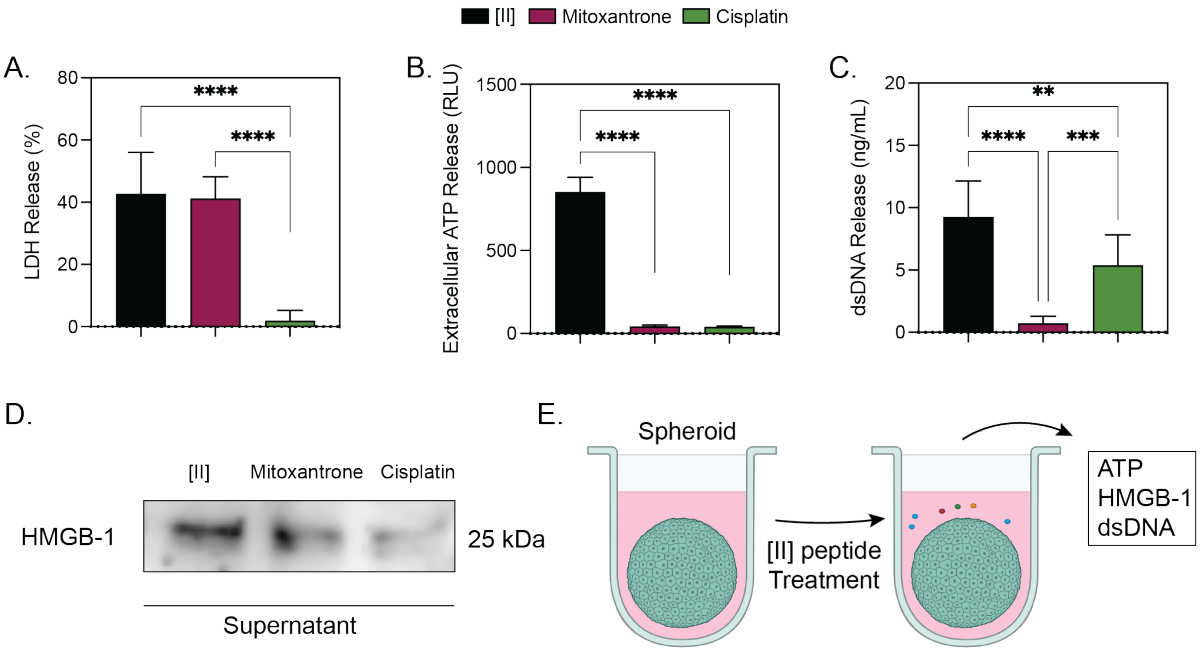


Figure 37 DAMP release from EMT6 spheroids. A. Release of LDH, B. Extracellular ATP, C. dsDNA, and D. HMGB-1 after [II], mitoxantrone, and cisplatin treatment at 24h. E. Schematic represents the DAMPs released by [II] aggregation. Statistical analysis was done with one-way ANOVA test; data are mean ± SD, **p<0.01, ***p<0.001, ****p<0.0001.

4.3.2.5. [II] peptide aggregation-induced DAMP release activates BMDCs

One of the most important cell types within the TME is DCs. Their proper activation is crucial for initiating antigen-specific adaptive immunity. A diverse set of pattern recognition receptors on DCs recognize DAMPs.[163] Several DAMPs and their effects on activating DCs are studied; ATP and HMGB-1 for DC recruitment and activation[368] and nucleic acids for antigen processing and presentation.[366] We used bone marrow differentiated DCs (BMDCs) to analyze the effect of released DAMPs on their activation in terms of cytokine release. We treated the spheroids with [II] peptide, mitoxantrone, and cisplatin for 24h and transferred their supernatants (spheroid

conditioned medium) onto BMDCs and analyzed their cytokine release profiles after incubating the spheroid conditioned medium for 6 and 24h **(Figure 38A)**.

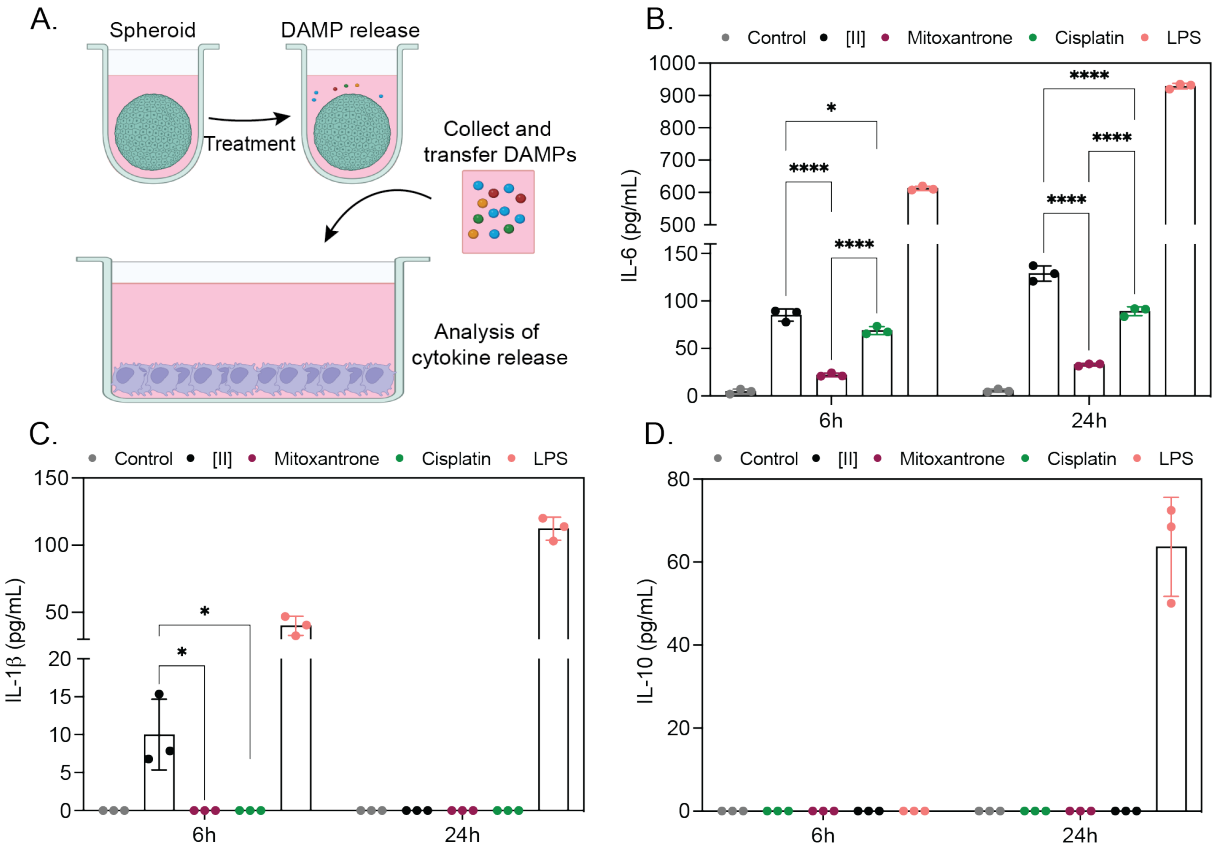


Figure 38 [II] aggregation-induced DAMP release activates BMDCs. A. Experimental plan for the treatment of BMDCs with tumor spheroid conditioned mediums. B. Release of IL-6, C. IL-1β, and D. IL-10, from BMDCs at 6h and 24h after tumor spheroid conditioned medium treatment. Statistical analysis was done with two-way ANOVA test; data are mean ± SD, *p<0.1, ****p<0.0001.

We found a significant (*p<0.1, ****p<0.0001) increase in the pro-inflammatory cytokine IL-6 secretion when BMDCs were cultured with [II] treated spheroid conditioned medium **(Figure 38B)**. IL-1β was only released from BMDCs cultured with [II] treated spheroid conditioned medium **(Figure 38C)**. This effect is due to the presence of extracellular ATP upon [II] treatment **(Figure 37B)**, as extracellular ATP has been shown to induce IL-1β release from DCs.[20] However, ATP is degraded extracellularly[188], which explains the lack of IL-1β release at 24h **(Figure 38C)**. Lastly, we checked the anti-inflammatory cytokine IL-10 and found no release among the conditions. Lipopolysaccharide (LPS) was used as a positive control for BMDC activation.[193]

4.3.2.6. [II] treated spheroid conditioned medium is non-toxic to BMDCs

Mitoxantrone is a bonafide ICD inducer[83], however, we failed to observe the effect of mitoxantrone released DAMPs on BMDC activation **(Figure 38B and C)**. To elaborate on this effect, we measured the viability of BMDCs after the transfer of spheroid conditioned mediums at 24h **(Figure 39A)**. Among the groups, only mitoxantrone induced additional significant cytotoxicity to BMDCs **(Figure 39B)**, explaining the low levels of cytokine release from BMDCs **(Figure 38B and C)**. This effect is due to the high mitoxantrone concentrations required to induce 50% cytotoxicity **(Figure 36B)** in the spheroid model.

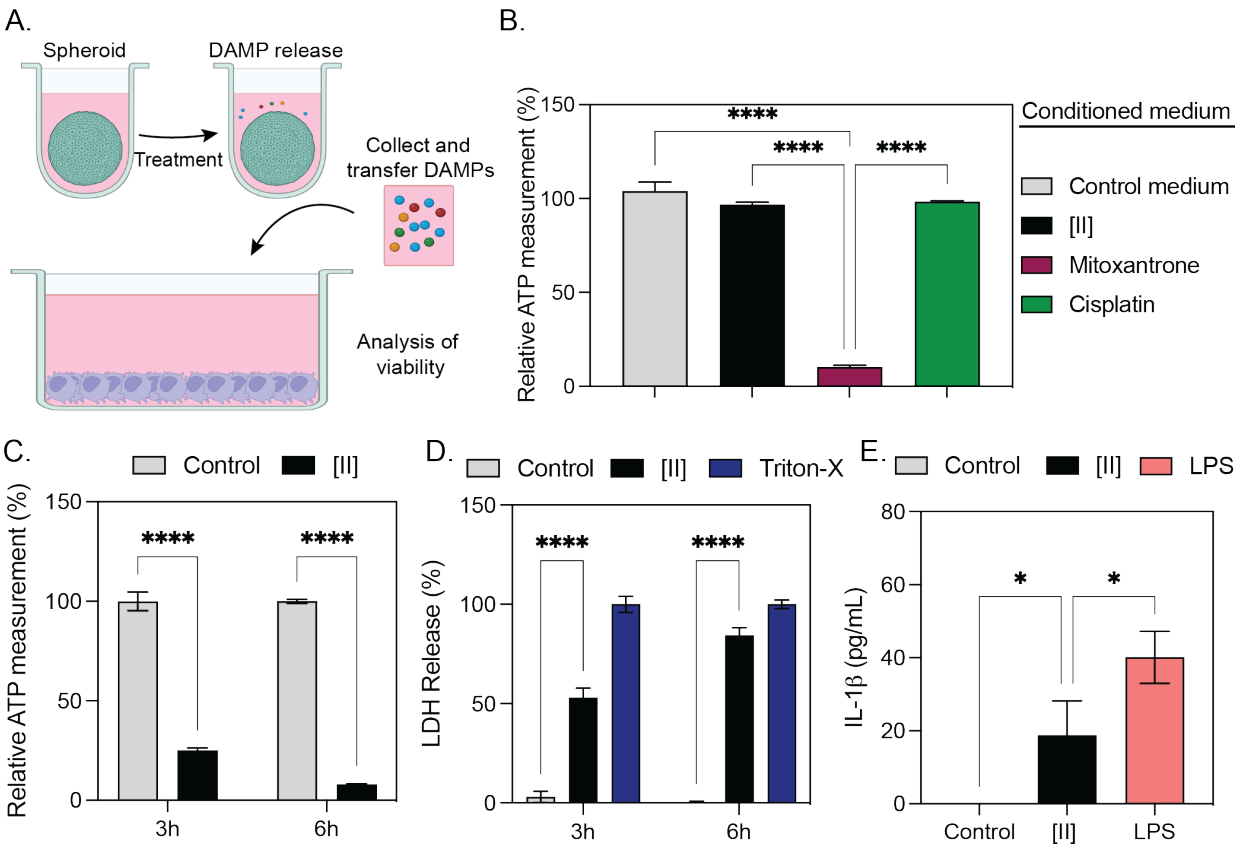


Figure 39 [II] treated spheroid conditioned medium is not cytotoxic to BMDCs. A. Schematic of the design for the viability measurement of BMDCs. B. Viability measurement of BMDCs after incubation with spheroid conditioned mediums at 24h. C. Viability and D. LDH and E. IL-1β release (6h) of BMDCs after [II] peptide treatment. Statistical analysis was done with one-way ANOVA (B and E) and two-way ANOVA tests (C and D); data are mean ± SD, ****p<0.0001.

Chemotherapeutics have side effects and toxicities to normal tissues when administered systemically.[369] While local/intratumoral delivery of chemotherapeutics reduces the side effects, the severity of side effects depends on required concentrations and the diffusion parameters.[370] Conditioned medium from [II] peptide had no cytotoxicity to BMDCs, showing that [II] effect would be contained locally **(Figure 39B)**, as we have shown before.[343] On the other hand, in the

case of an intratumoral treatment strategy, the initial injection will also affect multiple locally present cell types, including DCs. We wanted to understand the effects of [II] on DCs. Therefore, we treated BMDCs with [II] peptide and found that [II] aggregation induces time-dependent cell death **(Figure 39C)** and cell membrane damage **(Figure 39D)**. In addition, [II] treatment also induced IL-1β secretion from BMDCs **(Figure 39E)**. These data show that [II] aggregation-induced ICD and DAMP release is independent of cell type; however, the effects induced would be contained locally.

Here, we used a breast cancer spheroid model and studied the effect of peptide aggregation-induced ICD along with known chemotherapeutics. We showed that [II] aggregation-induced ICD can be controlled and is superior to chemotherapeutics in terms of type and amounts of DAMPs. DAMPs released upon [II] treatment activated DCs to secrete pro-inflammatory cytokines that have a role in orchestrating anti-tumor immunity. Furthermore, the transfer of [II] peptide solution did not induce further cytotoxicity, highlighting that [II] aggregation-induced ICD and DAMP release would be contained locally. This study shows that spheroids offer high throughput and physiologically relevant platform to pre-select and test the efficacy of treatment strategies for inducing ICD and DAMP release.

4.3.3. Conclusions

Classical monolayer culture is limited in understanding the efficacy of new treatment strategies for in vivo studies and eventually transitioning into clinical trials. Spheroids offer physiological relevance to solid tumors and provide a high-throughput system to test various conditions to select promising candidates for further studies. One of the most important relevance of spheroids to in vivo tumors is their resistance to chemotherapeutics, which ultimately changes

cell death. Considering that different concentration of chemotherapeutics alters the immunogenicity and DAMP release of dying cells[46,50,75], it is necessary to use physiologically relevant models to study ICD and DAMP release. Here, we compared the efficacy of the peptide aggregation model with known chemotherapeutics in the breast cancer spheroid model. We showed peptide aggregation model offers a superior platform in DAMP release and subsequent BMDC activation. Studying exclusively in monolayer cultures might not reflect the physiological outcome in terms of the composition and the type of released DAMPs. Therefore, spheroid models offer a more physiologically relevant model to study the immunogenicity of current treatment strategies and offer a platform to test the efficacy of new therapies.

4.3.4. Experimental Section

4.3.4.1. Materials

9-fluorenylmethoxycarbonyl (Fmoc) protected amino acids, [4-[a-(2',4'-dimethoxyphenyl) Fmoc aminomethyl] phenoxy] acetamidonorleucyl-MBHA resin (Rink amide MBHA resin), Oxyma, N, N'-Diisopropylcarbodiimide (DIC), piperidine, Trifluoroacetic acid (TFA), dimethylformamide (DMF), dichloromethane (DCM) was purchased from Gyros Protein Technologies. Triisopropylsilane, Acetic anhydride, Congo Red dye, and pyrene were purchased from Sigma-Aldrich. Deionized water (resistance of 18.2 MΩ.cm) was used during the experiments**.**

4.3.4.2. Peptide synthesis

KFFIIK and EFFIIE peptides were synthesized by solid-phase peptide synthesis with PreludeX automatic peptide synthesizer (Protein Technologies, Inc., Tucson, AZ). They were prepared on a 0.25 scale by repeated amino acid couplings using Fmoc protected amino acid (3 eq. 1mL), DIC (7.5 eq. 1mL), and Oxyma (7.5 eq. 1mL). MBHA Rink Amide resin (High-Loaded, Gyros Protein

Technologies) was used as solid support to construct the peptides. Fmoc protected amino acids (Gyros Protein Technologies) were removed through treatment with 20% piperidine/DMF solution for 45 min (three times for 15 min) at 80°C. All the peptide conjugation was performed for 2h at 80°C and acetylated with treatment with 10% acetonitrile/DMF solution for 15 min twice. Cleavage of the peptides from resin and deprotection of acid labile protected amino acids were carried out with a mixture of TFA/ TIS/ water in a ratio of 95:2.5:2.5 for 3 h at room temperature. Excess TFA and organic solvents were removed by evaporation, and the remaining peptide was precipitated using diethyl ether at 80°C by using 1:4 volume ratio and stayed overnight. After precipitation, peptides in ether solutions were centrifuged at 8000 rpm for 15 min. Peptide precipitates were collected, and ether was removed. The centrifuged white peptide precipitate was dissolved in either (0.1% formic acid in water for KFFIIK peptide) or (0.1% ammonium hydroxide in water for EFFIIE peptide). Peptides were purified with preparative HPLC (Agilent 1260) with Agilent ZORBAX 300 SB-C18 (9.4 x 250 mm) column with a mobile phase of water/acetonitrile mixture (0.1% ammonium hydroxide) used for negatively charged peptides; water/acetonitrile mixture (0.1% formic acid) was used for positively charged peptides. All peptides were tested with a purity >95%. HPLC run started with 100% water for 3 min, followed by a gradient increase in acetonitrile from 0% to 100% over 25 min, followed 100% acetonitrile for 3 min, and ended with 100% for 2 min. The flow rate is 2 mL/min, and injection volumes are 10 µL.

4.3.4.3. Thioflavin T (ThT) Assay

ThT (Sigma-Aldrich) was used to understand the aggregation kinetics of [II] peptide. ThT measurement included 1% albumin for 0.5 mM, 0.75 mM, and 1 mM [II] peptide. At first, fresh albumin (40mg/mL, 4 %w) was dissolved in 1x PBS and diluted into 1% in 1x PBS. Then, stock peptides (10 mM in water) were diluted (0.5 mM) individually. For ThT measurements, 5 μL from 400 μM ThT in PBS was added to 195 μL of 0.5 mM KFFIIK and EFFIIE individually. Then, each peptide was mixed and read with BioTek Neo2SM microplate reader for 4 h with 10 min intervals (Ex: 440, Em:480 with gain:90).

4.3.4.4. Cell Culture and Reagents

Mouse breast cancer cell line EMT6 was cultured in a humidified incubator at 37°C supplied with 5% CO2. EMT6 cells were cultured in Roswell Park Memorial Institute (RPMI) media (SIGMA R8758) supplemented with 10% FBS (Hyclone SH30910.03), 6 mM HEPES, 50 μM 2-mercaptoethanol and 1% antibiotics; penicillin (100 U/mL), and streptomycin (100 μg/mL) (Thermo Fisher 15240062). T75 flask (TPP 90076) was used to culture cells, and cells were passaged upon 85% confluency using trypsin (Sigma 59418C). The media was changed every 2 days.

4.3.4.5. Spheroid Formation and Characterization

EMT6 spheroids were formed through ultra-low attachment technique in U-bottom 96 well plates (CELLTREAT 229590). Briefly, wells of the U-bottom 96 well plate were treated with an anti-adherence rinsing solution (STEMCELL Technologies 07010) and centrifuged at 1300g for 5 min. Then, the solution was aspirated, and surfaces were washed with the basal medium. Then, wells were seeded with 20.000 EMT6 cells, and plates were centrifuged at 100g for 3 min. Media

was changed every day by carefully replacing 100 μL with fresh medium. Spheroids were imaged every 24h and later analyzed for their area, diameter, circularity, and solidity by using ImageJ.

$$Circularity = \frac{(4\pi \times Area)}{Perimeter^2}$$

$$Solidity = \frac{Area}{Convex\ Area}$$

4.3.4.6. Peptide and chemotherapeutics preparation and treatment

EFFIIE and KFFIIK were prepared in indicated concentrations in different albumin concentrations. We previously established the preparation technique of [II] peptide[343]. Briefly, individual charged counterparts were prepared in albumin solutions and mixed for 30 min before treatment. Mitoxantrone (Millipore Sigma M6545) and cisplatin (Millipore Sigma 232120) were used at indicated concentrations and prepared in normal cell culture medium.

4.3.4.7. LDH measurement

Cytoscan-LDH cytotoxicity assay kit (G-BIOSCIENCES 786-210) was used to measure LDH release from treated spheroids. Briefly, at the end of the 24h treatments, supernatants were collected after treatments and mixed with LDH reaction mixture for 20 min at 37°C. The reaction was stopped using the stop solution, and absorbance was measured at 490 nm and 680 nm. Triton-X was used to lyse the spheroids and used as a positive control for LDH release. 680nm background

signal was subtracted, and relative LDH release was calculated based on the positive maximum LDH release control group.

4.3.4.8. Extracellular ATP measurement

CellTiter-Glo 2.0 solution (Promega G9248) was used to measure the extracellular ATP released from spheroids. Briefly, at the end of 24h treatment, supernatants were mixed with CellTiter-Glo 2.0 solution and incubated for 5 min at room temperature. Then, the luminescent signal was measured with BioTek Neo2SM microplate reader accordingly with the manufacturer's instructions.

4.3.4.9. Extracellular dsDNA measurement

Extracellular dsDNA release from spheroids was measured using AccuGreen™ High Sensitivity dsDNA Quantitation Kit (BIOTIUM 31066-T). Briefly, at the end of 24h treatment, supernatants from spheroids were collected, and the released amount of dsDNA was measured accordingly with the manufacturer's instructions. A standard curve was generated and used to quantify the released dsDNA amounts.

4.3.4.10. Immunoblotting reagents

Acrylamide/Bis-acrylamide, 30% solution (Sigma A3699), 1.5 M Tris-HCl, pH 8.8 (Teknova T1588), Tris HCl Buffer 0.5 M solution, sterile pH 6.8 (Bio Basic SD8122), Ammonium persulfate (Sigma A3678), UltraPure 10% SDS (Invitrogen 15553-027), TEMED (Thermo Fisher Scientific 17919), Dithiothreitol (DTT) (BIO-RAD 1610610) Tris Base (Fisher Bioreagents BP152), Glycine (Fisher Bioreagents BP381), 4x Laemmli sample buffer (BIO-RAD 1610747), TWEEN 20 (Sigma P9416), Mini Trans-Blot filter paper (BIO-RAD 1703932), Nitrocellulose Membranes 0.45 μm (BIO-RAD 1620115), Western Blotting Luminol Reagent (Santa Cruz sc-2048).

4.3.4.11. Procedure

Protein samples were diluted in Laemmli buffer and boiled for 5 min at 96 °C. Proteins were then separated by sodium dodecyl sulfate-polyacrylamide gel electrophoresis (SDS-PAGE) gels (15%) and transferred to nitrocellulose membranes. After transfer, the membranes were blocked in 5% milk in Tris Buffered Saline with 0.1% Tween 20 (TBST). Blots were then incubated with HMGB-1-HRP (BioLegend 651411) overnight. The next day blots were washed with TBST and incubated with HRP conjugated secondary antibodies. Lastly, western blotting luminol reagent solution was added to the membranes, and chemiluminescence signal was detected by Azure c600 Imaging Biosystems.

4.3.4.12. BMDC generation

Bone marrow was harvested from the femurs and tibia of an 8-week-old BALB/c mouse. Bones were flushed with a cold medium 2 times and centrifuged twice at 1500 rpm for 5 min. Cells were incubated with 20 ng/mL GMCSF (BioLegend 576304) at a density of 2 x 10^6 cells for 8 days. On day 3, 20 ng/mL GMCSF in 10 mL is added and on day 6, 10 mL of cell solution was replaced with 10 mL fresh medium containing 20 ng/mL GMCSF. On day 8 loosely adhering BMDCs were collected through gentle pipetting.

4.3.4.13. Co-culture of spheroid conditioned medium with BMDCs

EMT6 spheroids were treated with [II] peptide, mitoxantrone, and cisplatin for 24h, and spheroid conditioned medium was mixed 1:1 (v:v) with BMDC medium, and BMDCs were incubated for 6 and 24h.

4.3.4.14. Enzyme-Linked Immunosorbent Assay (ELISA)

Supernatants of BMDCs were collected after 6 and 24h incubation with spheroid conditioned mediums. Collected supernatants were centrifuged at 500g for 5 min at 4 °C and used in ELISA. Briefly, plates were coated with capture antibody overnight. The next day, plates were blocked and incubated with supernatants, followed by incubation with the detection antibodies. Lastly, plates were incubated with Avidin-HRP and developed with TMB substrate solution. Absorbance was measured at 450 nm and 570 nm. 570 nm value was subtracted, and values were calculated based on the standard curve for IL-6 (BioLegend 431315), Il-1β (BioLegend 432615), and IL-10 (BioLegend 431414). Lipopolysaccharide (LPS) (Millipore Sigma L2630) was used as a positive control for cytokine release.

Chapter 5: Conclusions and Future Perspectives

In this dissertation, we introduced a tool inspired by the membrane damaging and DAMP release functionality of Aβ aggregation. [II] peptide aggregation induces ICD and DAMP release, and controllability of aggregation status offers modulation of the immune system. Effectivity of [II] peptide to induce immune response was shown here in three different applications: a quadrivalent influenza vaccination platform, a breast cancer prophylactic vaccination model and 3D breast cancer spheroid model. [II] peptide-based protection ultimately relies on the utilization of endogenous DAMPs present within the host. This makes [II] peptide as a tool to induce cell death but a controllable adjuvant as well. When designing materials, safety is one of the primary concerns. We have shown that [II] peptide is a safe tool engaging DAMP release and its activity is contained locally. It induces a controllable damage to the injection site, however, does not result in trauma or scar formation. Counterparts of [II] peptides are only 6 amino acids and therefore could not be presented by the APCs and do not elicit antibody formation against itself. DAMPs ultimately are the determinants of the immunogenicity of dying cells. The release of these molecules and their interactions with the immune cells are critical in almost every disease known. Their type and composition ultimately alter the progression of the diseases. Therefore, the ability to control the release of DAMPs holds the key to the development of effective therapies against many disease conditions, one of which is cancer. Currently, therapies are limited to, drug resistance, low to no immunogenicity induction within the tumor, and the patient's genetic background. The development of anti-cancer vaccines might offer personalized treatment strategies for cancer patients. In this strategy, the patient's cancer cells are obtained and killed in laboratory conditions and injected back into the patient. These dying cells provide DAMPs and

tumor-associated antigens of that particular patient. The ultimate goal is to induce strong immunogenicity in the dying cells so that the patient's immune system can attack the original tumor. However, mutations in tumors and drug resistance of cancer cells limit these applications severely and ultimately render them ineffective. Techniques that are limited with protein expression/mutations and ultimately drug resistance of a particular patient's cancer cells. Ideal tools for these applications are the tools that engage ICD and DAMP release through stress pathways that are conserved among all cell types. This eliminates the limitation of specific mutations or the patient's background. [II] peptide aggregation, in this regard, would present a very unique application for personalized anti-cancer vaccine development. Controllability of the aggregation-induced cell stress, ICD, and DAMP release offers a wide range of immunogenic windows to be studied for individual patients. In this scenario, the best immunogenic window could be identified for each patient separately by studying aggregation and time-dependent DAMP release. Moreover, patients dying cells could be co-cultured with patient's own isolated DCs and immunogenicity can be determined from the DC activation. Furthermore, in addition to dying cancer cells, the patient's own DCs which are activated with the patient's own cancer cells can be injected back into the patient for the development of a personalized DC vaccine.

In the case of vaccinations against viral infections, the antigen is provided exogenously. Purified antigens are mixed with adjuvants and ultimately used to increase the production of antigen-specific antibody formation. However, one of the limitations is the diffusion of antigens upon injection. This reduces the local antigen amount and ultimately decreases the activation of APCs. [II] peptide can be aggregated using the antigen itself, thereby localizing the antigen to the injection area. This approach not only would lead to higher local antigen concentrations but

attract immune cells due to the DAMP release effect of [II] peptide. Within this highly concentrated antigen-DAMP environment, the antigen itself could be slowly released and the local DAMPs would increase the activation. Localizing the antigen to a highly DAMP-present area might lead to the usage of fewer antigens to be able to induce protective immunity. Therefore, on the grand scale, the cost of antigen production would reduce, and ultimately more vaccinations can be done. Similarly, [II] peptide can be aggregated with the inactivated virus itself. This scenario would have both the DAMPs induced by [II] peptide aggregation but also the PAMPs from the inactivated virus. In this formulation, instead of just surface antigens such as HA, multiple different antigens of the virus would be presented to the immune system, increasing the protective capacity. Overall, engaging ICD and DAMP release is an emerging concept in both cancer treatment and development of new vaccinations strategies against viruses. Controlling the immunogenicity of dying cells by utilizing tools such as [II] have high potential to be translated in clinics for different treatment strategies.

Table 3 List of acronyms

Abbreviation	Meaning
A	
AD	Alzheimer's disease
AFM	Atomic force microscopy
Aβ	Amyloid beta
APC	Antigen presenting cell
B	
BMDC	Bone marrow derived dendritic cells
BSA	Bovine serum albumin
C	
CAC	Critical aggregation concentration
CoOP	Co-assembly of oppositely charged peptides
D	
DAMP	Damage associated molecular pattern
DC	Dendritic cell
DLS	Dynamic light scattering
DMEM	Dulbecco's Modified Eagle Medium
DPH	1,6-diphenyl-1,3,5-hexatriene
E	
ECM	Extracellular matrix

eIF2α	Eukaryotic initiation factor 2 alpha
ELISA	Enzyme linked immunosorbent assay
EMT	Epithelial mesenchymal transition
EOC	Epithelial ovarian cancer
F	
FBS	Fetal bovine serum
G	
GMCSF	Granulocyte macrophage colony stimulating factor
GSDMD	Gasdermin D
GSDME	Gasdermin E
H	
HA	Hemagglutinin
HSP	Heat shock protein
HMGB-1	High mobility group box 1
I	
ICD	Immunogenic cell death
IgG	Immunoglobulin G
IL	Interleukin
L	
LDH	Lactate dehydrogenase
LOT	Liquid overlay technique

LPS	Lipopolysaccharide
M	
MCTS	Multicellular tumor spheroid
MSA	Mouse serum albumin
P	
PAMP	Pathogen associated molecular patterns
PBS	Phosphate buffer saline
PFA	Paraformaldehyde
PI	Propidium iodide
PMA	Phorbol-12-myristate-13-acetate
PRR	Pattern recognition receptor
R	
RPMI	Roswell Park Memorial Institute (RPMI) 1640
S	
SDS	Sodium dodecyl sulfate
SEM	Scanning electron microscopy
T	
TBS	Tris-buffered saline
TBST	Tris-buffered saline tween
TEM	Transmission electron microscopy
ThT	Thioflavin T

TME	Tumor microenvironment
TLR	Toll like receptor
Y	
YAP	Yes associated protein

References

1. Thiery, J. *et al.* Perforin pores in the endosomal membrane trigger the release of endocytosed granzyme B into the cytosol of target cells. *Nat Immunol* **12**, 770–777 (2011).
2. Dunkelberger, J. R. & Song, W.-C. Complement and its role in innate and adaptive immune responses. *Cell Res* **20**, 34–50 (2010).
3. Vidarsson, G., Dekkers, G. & Rispens, T. IgG Subclasses and Allotypes: From Structure to Effector Functions. *Front Immunol* **5**, 520 (2014).
4. Jegaskanda, S., Reading, P. C. & Kent, S. J. Influenza-Specific Antibody-Dependent Cellular Cytotoxicity: Toward a Universal Influenza Vaccine. *J.I.* **193**, 469–475 (2014).
5. Nimmerjahn, F. Divergent Immunoglobulin G Subclass Activity Through Selective Fc Receptor Binding. *Science* **310**, 1510–1512 (2005).
6. Zhang, J. & Tao, A. Antigenicity, Immunogenicity, Allergenicity. in *Allergy Bioinformatics* (eds. Tao, A. & Raz, E.) vol. 8 175–186 (Springer Netherlands, 2015).
7. Ilinskaya, A. N. & Dobrovolskaia, M. A. Understanding the immunogenicity and antigenicity of nanomaterials: Past, present and future. *Toxicology and Applied Pharmacology* **299**, 70–77 (2016).
8. Kroemer, G., Galassi, C., Zitvogel, L. & Galluzzi, L. Immunogenic cell stress and death. *Nat Immunol* **23**, 487–500 (2022).
9. Jhunjhunwala, S., Hammer, C. & Delamarre, L. Antigen presentation in cancer: insights into tumour immunogenicity and immune evasion. *Nat Rev Cancer* **21**, 298–312 (2021).

10. Hubo, M. *et al.* Costimulatory Molecules on Immunogenic Versus Tolerogenic Human Dendritic Cells. *Front. Immunol.* **4**, (2013).
11. Goronzy, J. J. & Weyand, C. M. T-cell co-stimulatory pathways in autoimmunity. *Arthritis Res Ther* **10**, S3 (2008).
12. Gong, T., Liu, L., Jiang, W. & Zhou, R. DAMP-sensing receptors in sterile inflammation and inflammatory diseases. *Nat Rev Immunol* **20**, 95–112 (2020).
13. Matzinger, P. Tolerance, Danger, and the Extended Family. *Annual Review of Immunology* **12**, 991–1045 (1994).
14. Galluzzi, L. *et al.* Molecular mechanisms of cell death: recommendations of the Nomenclature Committee on Cell Death 2018. *Cell Death Differ* **25**, 486–541 (2018).
15. Tang, R. *et al.* Ferroptosis, necroptosis, and pyroptosis in anticancer immunity. *Journal of Hematology & Oncology* **13**, 110 (2020).
16. Green, D. R. The Coming Decade of Cell Death Research: Five Riddles. *Cell* **177**, 1094–1107 (2019).
17. Krysko, D. V. *et al.* Immunogenic cell death and DAMPs in cancer therapy. *Nat Rev Cancer* **12**, 860–875 (2012).
18. Kopp, R., Krautloher, A., Ramírez-Fernández, A. & Nicke, A. P2X7 Interactions and Signaling – Making Head or Tail of It. *Front. Mol. Neurosci.* **12**, 183 (2019).
19. Karmakar, M., Katsnelson, M. A., Dubyak, G. R. & Pearlman, E. Neutrophil P2X 7 receptors mediate NLRP3 inflammasome-dependent IL-1β secretion in response to ATP. *Nat Commun* **7**, 10555 (2016).

20. Ghiringhelli, F. *et al.* Activation of the NLRP3 inflammasome in dendritic cells induces IL-1β–dependent adaptive immunity against tumors. *Nat Med* **15**, 1170–1178 (2009).

21. Elliott, M. R. *et al.* Nucleotides released by apoptotic cells act as a find-me signal to promote phagocytic clearance. *Nature* **461**, 282–286 (2009).

22. Fucikova, J. *et al.* Detection of immunogenic cell death and its relevance for cancer therapy. *Cell Death Dis* **11**, 1–13 (2020).

23. Yu, M. *et al.* HMGB1 SIGNALS THROUGH TOLL-LIKE RECEPTOR (TLR) 4 AND TLR2. *Shock* **26**, 174–179 (2006).

24. Xu, J. *et al.* Macrophage endocytosis of high-mobility group box 1 triggers pyroptosis. *Cell Death Differ* **21**, 1229–1239 (2014).

25. Yang, H., Wang, H. & Andersson, U. Targeting Inflammation Driven by HMGB1. *Front. Immunol.* **11**, 484 (2020).

26. Messmer, D. *et al.* High Mobility Group Box Protein 1: An Endogenous Signal for Dendritic Cell Maturation and Th1 Polarization. *J Immunol* **173**, 307–313 (2004).

27. Yang, D. *et al.* High mobility group box-1 protein induces the migration and activation of human dendritic cells and acts as an alarmin. *Journal of Leukocyte Biology* **81**, 59–66 (2007).

28. Lee, S.-A., Kwak, M. S., Kim, S. & Shin, J.-S. The Role of High Mobility Group Box 1 in Innate Immunity. *Yonsei Med J* **55**, 1165 (2014).

29. Apetoh, L. *et al.* The interaction between HMGB1 and TLR4 dictates the outcome of anticancer chemotherapy and radiotherapy. *Immunol Rev* **220**, 47–59 (2007).

30. Hayashi, K. *et al.* Tipping the immunostimulatory and inhibitory DAMP balance to harness immunogenic cell death. *Nat Commun* **11**, 6299 (2020).

31. Gardai, S. J. *et al.* Cell-Surface CRT Initiates Clearance of Viable or Apoptotic Cells through trans-Activation of LRP on the Phagocyte. *Cell* **123**, 321–334 (2005).

32. Obeid, M. *et al.* CRT exposure dictates the immunogenicity of cancer cell death. *Nat Med* **13**, 54–61 (2007).

33. Asea, A. *et al.* HSP70 stimulates cytokine production through a CD14-dependant pathway, demonstrating its dual role as a chaperone and cytokine. *Nat Med* **6**, 435–442 (2000).

34. Imai, T. *et al.* Heat shock protein 90 (HSP90) contributes to cytosolic translocation of extracellular antigen for cross-presentation by dendritic cells. *PNAS* **108**, 16363–16368 (2011).

35. Luo, M. *et al.* Laser immunotherapy for cutaneous squamous cell carcinoma with optimal thermal effects to enhance tumour immunogenicity. *Int J Hyperthermia* **34**, 1337–1350 (2018).

36. Mathew, A. *et al.* Degraded Mitochondrial DNA is a Newly Identified Subtype of the Damage Associated Molecular Pattern (DAMP) Family and Possible Trigger of Neurodegeneration. *JAD* **30**, 617–627 (2012).

37. Zhang, J.-Z., Liu, Z., Liu, J., Ren, J.-X. & Sun, T.-S. Mitochondrial DNA induces inflammation and increases TLR9/NF-κB expression in lung tissue. *International Journal of Molecular Medicine* **33**, 817–824 (2014).

38. Simmons, J. D. *et al.* Elevated Levels of Plasma Mitochondrial DNA DAMPs Are Linked to Clinical Outcome in Severely Injured Human Subjects. *Annals of Surgery* **258**, 591–598 (2013).

39. Tian, J. *et al.* Toll-like receptor 9–dependent activation by DNA-containing immune complexes is mediated by HMGB1 and RAGE. *Nat Immunol* **8**, 487–496 (2007).

40. Rose II, W. A., Okragly, A. J., Patel, C. N. & Benschop, R. J. IL-33 released by alum is responsible for early cytokine production and has adjuvant properties. *Sci Rep* **5**, 13146 (2015).

41. Oleszycka, E. *et al.* IL-1α and inflammasome-independent IL-1β promote neutrophil infiltration following alum vaccination. *FEBS J* **283**, 9–24 (2016).

42. Yu, J. *et al.* Cleavage of GSDME by caspase-3 determines lobaplatin-induced pyroptosis in colon cancer cells. *Cell Death & Disease* **10**, 1–20 (2019).

43. Dinarello, C. A. IL-18: A TH1 -inducing, proinflammatory cytokine and new member of the IL-1 family. *Journal of Allergy and Clinical Immunology* **103**, 11–24 (1999).

44. Yang, H., Wang, H., Chavan, S. S. & Andersson, U. High Mobility Group Box Protein 1 (HMGB1): The Prototypical Endogenous Danger Molecule. *Mol Med* **21**, S6–S12 (2015).

45. Yamazaki, T. *et al.* Defective immunogenic cell death of HMGB1-deficient tumors: compensatory therapy with TLR4 agonists. *Cell Death Differ* **21**, 69–78 (2014).

46. Tesniere, A. *et al.* Immunogenic death of colon cancer cells treated with oxaliplatin. *Oncogene* **29**, 482–491 (2010).

47. Apetoh, L. *et al.* Toll-like receptor 4–dependent contribution of the immune system to anticancer chemotherapy and radiotherapy. *Nat Med* **13**, 1050–1059 (2007).

48. Bergmann, C. *et al.* Toll-like receptor 4 single-nucleotide polymorphisms Asp299Gly and Thr399Ile in head and neck squamous cell carcinomas. *J Transl Med* **9**, 139 (2011).

49. Selzner, N. *et al.* Water induces autocrine stimulation of tumor cell killing through ATP release and P2 receptor binding. *Cell Death Differ* **11**, S172–S180 (2004).

50. Martins, I. *et al.* Chemotherapy induces ATP release from tumor cells. *Cell Cycle* **8**, 3723–3728 (2009).

51. Efimova, I. *et al.* Vaccination with early ferroptotic cancer cells induces efficient antitumor immunity. *J Immunother Cancer* **8**, e001369 (2020).

52. Garg, A. D., Krysko, D. V., Vandenabeele, P. & Agostinis, P. Extracellular ATP and P2X7 receptor exert context-specific immunogenic effects after immunogenic cancer cell death. *Cell Death Dis* **7**, e2097–e2097 (2016).

53. Fucikova, J. *et al.* CRT Expression in Human Non–Small Cell Lung Cancers Correlates with Increased Accumulation of Antitumor Immune Cells and Favorable Prognosis. *Cancer Res* **76**, 1746–1756 (2016).

54. Bezu, L. *et al.* eIF2α phosphorylation is pathognomonic for immunogenic cell death. *Cell Death Differ* **25**, 1375–1393 (2018).

55. Panaretakis, T. *et al.* Mechanisms of pre-apoptotic CRT exposure in immunogenic cell death. *EMBO J* **28**, 578–590 (2009).

56. Garg, A. D. *et al.* A novel pathway combining CRT exposure and ATP secretion in immunogenic cancer cell death: CRT, ATP, and immunogenic cancer cell death. *The EMBO Journal* **31**, 1062–1079 (2012).

57. S. Wheeler, D. Extracellular Heat Shock Proteins: Alarmins for the Host Immune System. *TOINFJ* **4**, 49–60 (2011).

58. Basu, S., Binder, R. J., Suto, R., Anderson, K. M. & Srivastava, P. K. Necrotic but not apoptotic cell death releases heat shock proteins, which deliver a partial maturation signal to dendritic cells and activate the NF-κB pathway. *Int Immunol* **12**, 1539–1546 (2000).

59. Spisek, R. *et al.* Bortezomib enhances dendritic cell (DC)–mediated induction of immunity to human myeloma via exposure of cell surface heat shock protein 90 on dying tumor cells: therapeutic implications. *Blood* **109**, 4839–4845 (2007).

60. Brough, D., Pelegrin, P. & Nickel, W. An emerging case for membrane pore formation as a common mechanism for the unconventional secretion of FGF2 and IL-1β. *Journal of Cell Science* jcs.204206 (2017) doi:10.1242/jcs.204206.

61. Evavold, C. L. *et al.* The Pore-Forming Protein Gasdermin D Regulates Interleukin-1 Secretion from Living Macrophages. *Immunity* **48**, 35-44.e6 (2018).

62. Cullen, S. P., Kearney, C. J., Clancy, D. M. & Martin, S. J. Diverse Activators of the NLRP3 Inflammasome Promote IL-1β Secretion by Triggering Necrosis. *Cell Reports* **11**, 1535–1548 (2015).

63. Martin, S. J. Cell death and inflammation: the case for IL-1 family cytokines as the canonical DAMPs of the immune system. *FEBS J* **283**, 2599–2615 (2016).

64. Sasaki, E. *et al.* Nasal alum-adjuvanted vaccine promotes IL-33 release from alveolar epithelial cells that elicits IgA production via type 2 immune responses. *PLoS Pathog* **17**, e1009890 (2021).

65. Yatim, N., Cullen, S. & Albert, M. L. Dying cells actively regulate adaptive immune responses. *Nat Rev Immunol* **17**, 262–275 (2017).

66. Martin, S. J., Frezza, V., Davidovich, P., Najda, Z. & Clancy, D. M. IL-1 family cytokines serve as 'activity recognition receptors' for aberrant protease activity indicative of danger. *Cytokine* **157**, 155935 (2022).

67. Chen, C.-J. *et al.* Identification of a key pathway required for the sterile inflammatory response triggered by dying cells. *Nat Med* **13**, 851–856 (2007).

68. Gu, H. *et al.* High-mobility group box 1 protein contributes to the immunogenicity of rTcdB-treated CT26 cells. *Acta Biochimica et Biophysica Sinica* **50**, 921–928 (2018).

69. Zhang, W. *et al.* Necrotic Myocardial Cells Release Damage-Associated Molecular Patterns That Provoke Fibroblast Activation In Vitro and Trigger Myocardial Inflammation and Fibrosis In Vivo. *JAHA* **4**, (2015).

70. Zhang, Q. *et al.* Circulating mitochondrial DAMPs cause inflammatory responses to injury. *Nature* **464**, 104–107 (2010).

71. Vono, M. *et al.* The adjuvant MF59 induces ATP release from muscle that potentiates response to vaccination. *PNAS* **110**, 21095–21100 (2013).

72. Zhang, Y. *et al.* Temperature-dependent cell death patterns induced by functionalized gold nanoparticle photothermal therapy in melanoma cells. *Sci Rep* **8**, 8720 (2018).

73. Oresta, B. *et al.* Mitochondrial metabolic reprogramming controls the induction of immunogenic cell death and efficacy of chemotherapy in bladder cancer. *Sci. Transl. Med.* **13**, eaba6110 (2021).

74. Li, C. *et al.* Mitoxantrone triggers immunogenic prostate cancer cell death via p53-dependent PERK expression. *Cell Oncol.* **43**, 1099–1116 (2020).

75. Sriram, G. *et al. The Injury Response to DNA Damage Promotes Anti-Tumor Immunity*. http://biorxiv.org/lookup/doi/10.1101/2020.04.26.062216 (2020) doi:10.1101/2020.04.26.062216.

76. Wei, W. *et al.* Proteasome inhibitors attenuates mitoxantrone-triggered immunogenic cell death in prostate cancer cells. *Med Oncol* **37**, 116 (2020).

77. Casares, N. *et al.* Caspase-dependent immunogenicity of doxorubicin-induced tumor cell death. *Journal of Experimental Medicine* **202**, 1691–1701 (2005).

78. Broz, P., Pelegrín, P. & Shao, F. The gasdermins, a protein family executing cell death and inflammation. *Nature Reviews Immunology* **20**, 143–157 (2020).

79. Zhang, Z. *et al.* Gasdermin E suppresses tumour growth by activating anti-tumour immunity. *Nature* **579**, 415–420 (2020).

80. Op de Beeck, K., Van Laer, L. & Van Camp, G. DFNA5, a Gene Involved in Hearing Loss and Cancer: A Review. *Ann Otol Rhinol Laryngol* **121**, 197–207 (2012).

81. Akino, K. *et al.* Identification of DFNA5 as a target of epigenetic inactivation in gastric cancer. *Cancer Science* **98**, 88–95 (2007).

82. Zhao, T. *et al.* Inhibition of HIF-1α by PX-478 enhances the anti-tumor effect of gemcitabine by inducing immunogenic cell death in pancreatic ductal adenocarcinoma. *Oncotarget* **6**, 2250–2262 (2015).

83. Kepp, O. *et al.* Consensus guidelines for the detection of immunogenic cell death. *OncoImmunology* **3**, e955691 (2014).

84. Hangai, S. *et al.* PGE2 induced in and released by dying cells functions as an inhibitory DAMP. *Proc. Natl. Acad. Sci. U.S.A.* **113**, 3844–3849 (2016).

85. Martins, I. *et al.* Restoration of the immunogenicity of cisplatin-induced cancer cell death by endoplasmic reticulum stress. *Oncogene* **30**, 1147–1158 (2011).

86. Obeid, M. *et al.* CRT exposure is required for the immunogenicity of gamma-irradiation and UVC light-induced apoptosis. *Cell Death Differ* **14**, 1848–1850 (2007).

87. Stangl, S. *et al.* Detection of irradiation-induced, membrane heat shock protein 70 (Hsp70) in mouse tumors using Hsp70 Fab fragment. *Radiotherapy and Oncology* **99**, 313–316 (2011).

88. Rodriguez-Ruiz, M. E., Vitale, I., Harrington, K. J., Melero, I. & Galluzzi, L. Immunological impact of cell death signaling driven by radiation on the tumor microenvironment. *Nat Immunol* **21**, 120–134 (2020).

89. Zhu, M. *et al.* Immunogenic Cell Death Induction by Ionizing Radiation. *Front. Immunol.* **12**, 705361 (2021).

90. Huang, Y. *et al.* Comparison of the effects of photon, proton and carbon-ion radiation on the ecto-CRT exposure in various tumor cell lines. *Ann. Transl. Med.* **7**, 542–542 (2019).

91. Liu, S. *et al.* Effects of radiation on T regulatory cells in normal states and cancer: mechanisms and clinical implications. *Am J Cancer Res* **5**, 3276–3285 (2015).

92. Aryankalayil, M. J. *et al.* Defining Molecular Signature of Pro-Immunogenic Radiotherapy Targets in Human Prostate Cancer Cells. *Radiation Research* **182**, 139–148 (2014).

93. Lugade, A. A. *et al.* Local Radiation Therapy of B16 Melanoma Tumors Increases the Generation of Tumor Antigen-Specific Effector Cells That Traffic to the Tumor. *J Immunol* **174**, 7516–7523 (2005).

94. Hu, Q., Huang, Z., Duan, Y., Fu, Z., & Bin Liu. Reprogramming Tumor Microenvironment with Photothermal Therapy. *Bioconjugate Chem.* **31**, 1268–1278 (2020).

95. Sweeney, E. E., Cano-Mejia, J. & Fernandes, R. Photothermal Therapy Generates a Thermal Window of Immunogenic Cell Death in Neuroblastoma. *Small* **14**, 1800678 (2018).

96. Bear, A. S. *et al.* Elimination of Metastatic Melanoma Using Gold Nanoshell-Enabled Photothermal Therapy and Adoptive T Cell Transfer. *PLoS ONE* **8**, e69073 (2013).

97. Zhou, F. *et al.* Local Phototherapy Synergizes with Immunoadjuvant for Treatment of Pancreatic Cancer through Induced Immunogenic Tumor Vaccine. *Clin Cancer Res* **24**, 5335–5346 (2018).

98. Bahar, A. A. & Ren, D. Antimicrobial Peptides. *Pharmaceuticals* **6**, 1543–1575 (2013).

99. Lei, J. *et al.* The antimicrobial peptides and their potential clinical applications. *Am J Transl Res* **11**, 3919–3931 (2019).

100. Wodlej, C. *et al.* Interaction of two antitumor peptides with membrane lipids – Influence of phosphatidylserine and cholesterol on specificity for melanoma cells. *PLoS ONE* **14**, e0211187 (2019).

101. Wang, Y. *et al.* Intratumoral Expression of Mature Human Neutrophil Peptide-1 Mediates Antitumor Immunity in Mice. *Clinical Cancer Research* **15**, 6901–6911 (2009).

102. Lee, H. S. *et al.* Mechanism of anticancer activity of buforin IIb, a histone H2A-derived peptide. *Cancer Letters* **271**, 47–55 (2008).

103. Chen, X. *et al.* A novel antimicrobial peptide, Ranatuerin-2PLx, showing therapeutic potential in inhibiting proliferation of cancer cells. *Bioscience Reports* **38**, BSR20180710 (2018).

104. Kim, J.-Y. *et al.* Necrosis-inducing peptide has the beneficial effect on killing tumor cells through neuropilin (NRP-1) targeting. *Oncotarget* **7**, 32449–32461 (2016).

105. Phan, T. K. *et al.* Human β-defensin 3 contains an oncolytic motif that binds PI(4,5)P2 to mediate tumour cell permeabilisation. *Oncotarget* **7**, 2054–2069 (2016).

106. Zhou, H. *et al.* The oncolytic peptide LTX-315 triggers immunogenic cell death. *Cell Death Dis* **7**, e2134–e2134 (2016).

107. Eike, L.-M., Yang, N., Rekdal, Ø. & Sveinbjørnsson, B. The oncolytic peptide LTX-315 induces cell death and DAMP release by mitochondria distortion in human melanoma cells. *Oncotarget* **6**, 34910–34923 (2015).

108. Camilio, K. A., Berge, G., Ravuri, C. S., Rekdal, Ø. & Sveinbjørnsson, B. Complete regression and systemic protective immune responses obtained in B16 melanomas after treatment with LTX-315. *Cancer Immunol Immunother* **63**, 601–613 (2014).

109. Zhou, H. *et al.* The oncolytic peptide LTX-315 kills cancer cells through Bax/Bak-regulated mitochondrial membrane permeabilization. *Oncotarget* **6**, 26599–26614 (2015).

110. Krajewski, S. *et al.* Reduced expression of proapoptotic gene BAX is associated with poor response rates to combination chemotherapy and shorter survival in women with metastatic breast adenocarcinoma. *Cancer Res* **55**, 4471–4478 (1995).

111. Camilio, K. A. *et al.* Combining the oncolytic peptide LTX-315 with doxorubicin demonstrates therapeutic potential in a triple-negative breast cancer model. *Breast Cancer Res* **21**, 9 (2019).

112. Eike, L.-M., Mauseth, B., Camilio, K. A., Rekdal, Ø. & Sveinbjørnsson, B. The Cytolytic Amphipathic β(2,2)-Amino Acid LTX-401 Induces DAMP Release in Melanoma Cells and Causes Complete Regression of B16 Melanoma. *PLoS ONE* **11**, e0148980 (2016).

113. Xie, W. *et al.* Tumor lysis with LTX-401 creates anticancer immunity. *OncoImmunology* **8**, e1594555 (2019).

114. Munshi, T., Sparrow, A., Wren, B. W., Reljic, R. & Willcocks, S. J. The Antimicrobial Peptide, Bactenecin 5, Supports Cell-Mediated but Not Humoral Immunity in the Context of a Mycobacterial Antigen Vaccine Model. *Antibiotics* **9**, 926 (2020).

115. Olafsdottir, T. A., Lingnau, K., Nagy, E. & Jonsdottir, I. IC31 ®, a Two-Component Novel Adjuvant Mixed with a Conjugate Vaccine Enhances Protective Immunity against Pneumococcal Disease in Neonatal Mice. *Scandinavian Journal of Immunology* **69**, 194–202 (2009).

116. Sriram, G. *et al.* The injury response to DNA damage in live tumor cells promotes antitumor immunity. *Sci. Signal.* **14**, eabc4764 (2021).

117. Lin, M., Liu, N., Qin, Z. & Wang, Y. Mitochondrial-derived damage-associated molecular patterns amplify neuroinflammation in neurodegenerative diseases. *Acta Pharmacol Sin* (2022) doi:10.1038/s41401-022-00879-6.

118. Gambardella, S. *et al.* ccf-mtDNA as a Potential Link Between the Brain and Immune System in Neuro-Immunological Disorders. *Front. Immunol.* **10**, 1064 (2019).

119. Wilkins, H. M. *et al.* Extracellular Mitochondria and Mitochondrial Components Act as Damage-Associated Molecular Pattern Molecules in the Mouse Brain. *J Neuroimmune Pharmacol* **11**, 622–628 (2016).

120. Tanaka, H. *et al.* YAP-dependent necrosis occurs in early stages of Alzheimer's disease and regulates mouse model pathology. *Nat Commun* **11**, 507 (2020).

121. Walter, S. *et al.* Role of the Toll-Like Receptor 4 in Neuroinflammation in Alzheimer's Disease. *Cell Physiol Biochem* **20**, 947–956 (2007).

122. Lee, D. Y. *et al.* Activation of PERK Signaling Attenuates Aβ-Mediated ER Stress. *PLoS ONE* **5**, e10489 (2010).

123. Chang, R. C. C., Wong, A. K. Y., Ng, H.-K. & Hugon, J. Phosphorylation of eukaryotic initiation factor-2α (eIF2α) is associated with neuronal degeneration in Alzheimer's disease: *NeuroReport* **13**, 2429–2432 (2002).

124. Carrillo-Mora, P., Luna, R. & Colín-Barenque, L. Amyloid Beta: Multiple Mechanisms of Toxicity and Only Some Protective Effects? *Oxidative Medicine and Cellular Longevity* **2014**, 1–15 (2014).

125. Irwin, M. *et al.* A Positive Feedback Loop of Hippo- and c-Jun-Amino-Terminal Kinase Signaling Pathways Regulates Amyloid-Beta-Mediated Neurodegeneration. *Front. Cell Dev. Biol.* **8**, 117 (2020).

126. Hao, Y., Chun, A., Cheung, K., Rashidi, B. & Yang, X. Tumor Suppressor LATS1 Is a Negative Regulator of Oncogene YAP. *Journal of Biological Chemistry* **283**, 5496–5509 (2008).

127. Abylkassov, R. & Xie, Y. Role of Yes-associated protein in cancer: An update. *Oncology Letters* **12**, 2277–2282 (2016).

128. Mueller, K. A. *et al.* Hippo Signaling Pathway Dysregulation in Human Huntington's Disease Brain and Neuronal Stem Cells. *Sci Rep* **8**, 11355 (2018).

129. Moujalled, D., Strasser, A. & Liddell, J. R. Molecular mechanisms of cell death in neurological diseases. *Cell Death Differ* **28**, 2029–2044 (2021).

130. Koper, M. J. *et al.* Necrosome complex detected in granulovacuolar degeneration is associated with neuronal loss in Alzheimer's disease. *Acta Neuropathol* **139**, 463–484 (2020).

131. Motawi, T. M. K., Abdel-Nasser, Z. M. & Shahin, N. N. Ameliorative Effect of Necrosulfonamide in a Rat Model of Alzheimer's Disease: Targeting Mixed Lineage Kinase Domain-like Protein-Mediated Necroptosis. *ACS Chem. Neurosci.* **11**, 3386–3397 (2020).

132. Zhao, W. *et al.* Targeting Necroptosis as a Promising Therapy for Alzheimer's Disease. *ACS Chem. Neurosci.* acschemneuro.2c00172 (2022) doi:10.1021/acschemneuro.2c00172.

133. Tan, M.-S. *et al.* Amyloid- β induces NLRP1-dependent neuronal pyroptosis in models of Alzheimer's disease. *Cell Death & Disease* **5**, e1382–e1382 (2014).

134. Halle, A. *et al.* The NALP3 inflammasome is involved in the innate immune response to amyloid-β. *Nat Immunol* **9**, 857–865 (2008).

135. Nakanishi, A. *et al.* Amyloid β directly interacts with NLRP3 to initiate inflammasome activation: identification of an intrinsic NLRP3 ligand in a cell-free system. *Inflamm Regen* **38**, (2018).

136. Goodman, L. ALZHEIMER'S DISEASE: A Clinico-pathologic Analysis of Twenty-three Cases with a Theory on Pathogenesis. *The Journal of Nervous and Mental Disease* **118**, 97–130 (1953).

137. Reichert, C. O. *et al.* Ferroptosis Mechanisms Involved in Neurodegenerative Diseases. *IJMS* **21**, 8765 (2020).

138. Hallgren, B. & Sourander, P. THE NON-HAEMIN IRON IN THE CEREBRAL CORTEX IN ALZHEIMER'S DISEASE. *J Neurochem* **5**, 307–310 (1960).

139. Rao, S. S. *et al.* Characterising the spatial and temporal brain metal profile in a mouse model of tauopathy. *Metallomics* **12**, 301–313 (2020).

140. Yan, N. & Zhang, J. Iron Metabolism, Ferroptosis, and the Links With Alzheimer's Disease. *Front. Neurosci.* **13**, 1443 (2020).

141. Hambright, W. S., Fonseca, R. S., Chen, L., Na, R. & Ran, Q. Ablation of ferroptosis regulator glutathione peroxidase 4 in forebrain neurons promotes cognitive impairment and neurodegeneration. *Redox Biology* **12**, 8–17 (2017).

142. Paradís-Bas, M., Tulla-Puche, J. & Albericio, F. The road to the synthesis of "difficult peptides". *Chem. Soc. Rev.* **45**, 631–654 (2016).

143. Kasim, J. K., Kavianinia, I., Harris, P. W. R. & Brimble, M. A. Three Decades of Amyloid Beta Synthesis: Challenges and Advances. *Front. Chem.* **7**, 472 (2019).

144. Leverone, J. A$beta;1-15 is less immunogenic than A$beta;1-40/42 for intranasal immunization of wild-type mice but may be effective for ?boosting? *Vaccine* **21**, 2197–2206 (2003).

145. Hamsici, S., White, A. D. & Acar, H. Peptide framework for screening the effects of amino acids on assembly. *Science Advances* (2022) doi:10.1126/sciadv.abj0305.

146. Galluzzi, L., Buqué, A., Kepp, O., Zitvogel, L. & Kroemer, G. Immunogenic cell death in cancer and infectious disease. *Nat Rev Immunol* **17**, 97–111 (2017).

147. Hu, L. *et al.* Chemotherapy-induced pyroptosis is mediated by BAK/BAX-caspase-3-GSDME pathway and inhibited by 2-bromopalmitate. *Cell Death Dis* **11**, (2020).

148. Li, Y., Liu, X., Pan, W., Li, N. & Tang, B. Photothermal therapy-induced immunogenic cell death based on natural melanin nanoparticles against breast cancer. *Chem. Commun.* **56**, 1389–1392 (2020).

149. Hayashi, T. *et al.* DAMP-Inducing Adjuvant and PAMP Adjuvants Parallelly Enhance Protective Type-2 and Type-1 Immune Responses to Influenza Split Vaccination. *Front. Immunol.* **9**, (2018).

150. Gao, J., Wang, W., Pei, Q., Lord, M. S. & Yu, H. Engineering nanomedicines through boosting immunogenic cell death for improved cancer immunotherapy. *Acta Pharmacol Sin* **41**, 986–994 (2020).

151. Zhu, X. *et al.* Temperature-feedback upconversion nanocomposite for accurate photothermal therapy at facile temperature. *Nat Commun* **7**, 10437 (2016).

152. Paules, C. I., Sullivan, S. G., Subbarao, K. & Fauci, A. S. Chasing Seasonal Influenza — The Need for a Universal Influenza Vaccine. *New England Journal of Medicine* **378**, 7–9 (2018).

153. Shao, W., Li, X., Goraya, M., Wang, S. & Chen, J.-L. Evolution of Influenza A Virus by Mutation and Re-Assortment. *IJMS* **18**, 1650 (2017).

154. Davis, C. W. *et al.* Influenza vaccine–induced human bone marrow plasma cells decline within a year after vaccination. *Science* **370**, 237–241 (2020).

155. Moran, T. M., Park, H., Fernandez-Sesma, A. & Schulman, J. L. Th2 Responses to Inactivated Influenza Virus Can Be Converted to Th1 Responses and Facilitate Recovery

from Heterosubtypic Virus Infection. *The Journal of Infectious Diseases* **180**, 579–585 (1999).

156. Oleszycka, E. *et al.* The vaccine adjuvant alum promotes IL-10 production that suppresses Th1 responses. *Eur. J. Immunol.* **48**, 705–715 (2018).
157. Miyauchi, K. *et al.* Protective neutralizing influenza antibody response in the absence of T follicular helper cells. *Nat Immunol* **17**, 1447–1458 (2016).
158. Stevens, T. L. *et al.* Regulation of antibody isotype secretion by subsets of antigen-specific helper T cells. *Nature* **334**, 255–258 (1988).
159. Firacative, C. *et al.* Identification of T helper (Th)1- and Th2-associated antigens of Cryptococcus neoformans in a murine model of pulmonary infection. *Sci Rep* **8**, 2681 (2018).
160. Liu, Y. *et al.* Visualization of perforin/gasdermin/complement-formed pores in real cell membranes using atomic force microscopy. *Cellular & Molecular Immunology* **16**, 611–620 (2019).
161. Walsh, P. *et al.* The Mechanism of Membrane Disruption by Cytotoxic Amyloid Oligomers Formed by Prion Protein(106–126) Is Dependent on Bilayer Composition. *Journal of Biological Chemistry* **289**, 10419–10430 (2014).
162. Liu, X. & Lieberman, J. Knocking 'em Dead: Pore-Forming Proteins in Immune Defense. *Annual Review of Immunology* **38**, 455–485 (2020).
163. Zhou, J. *et al.* Immunogenic cell death in cancer therapy: Present and emerging inducers. *Journal of Cellular and Molecular Medicine* **23**, 4854–4865 (2019).

164. Chen, G. Y. & Nuñez, G. Sterile inflammation: sensing and reacting to damage. *Nat Rev Immunol* **10**, 826–837 (2010).

165. Fagone, P. *et al.* Molecular adjuvant HMGB1 enhances anti-influenza immunity during DNA vaccination. *Gene Therapy* **18**, 1070–1077 (2011).

166. Murshid, A., Gong, J. & Calderwood, S. K. Hsp90 mediates Efficient Antigen Cross Presentation Through the Scavenger Receptor SREC-I. *J Immunol* **185**, 2903–2917 (2010).

167. Dumitriu, I. E., Bianchi, M. E., Bacci, M., Manfredi, A. A. & Rovere-Querini, P. The secretion of HMGB1 is required for the migration of maturing dendritic cells. *Journal of Leukocyte Biology* **81**, 84–91 (2007).

168. Gray, V. P. *et al.* Biomaterials via peptide assembly: design, characterization, and application in tissue engineering. *Acta Biomaterialia* (2021) doi:10.1016/j.actbio.2021.10.030.

169. Hamsici, S. *et al.* CHAPTER 9 Drug Delivery Applications of Peptide Materials. in *Peptide-based Biomaterials* 291–334 (The Royal Society of Chemistry, 2021). doi:10.1039/9781839161148-00291.

170. Acar, H. *et al.* Self-assembling peptide-based building blocks in medical applications. *Adv. Drug Deliv. Rev.* **110–111**, 65–79 (2017).

171. Travkova, O. G., Moehwald, H. & Brezesinski, G. The interaction of antimicrobial peptides with membranes. *Advances in Colloid and Interface Science* **247**, 521–532 (2017).

172. Moore, A. N. & Hartgerink, J. D. Self-Assembling Multidomain Peptide Nanofibers for Delivery of Bioactive Molecules and Tissue Regeneration. *Acc. Chem. Res.* **50**, 714–722 (2017).

173. Mu, Y. & Yu, M. Effects of Hydrophobic Interaction Strength on the Self-Assembled Structures of Model Peptides. *Soft Matter* **10**, 4956–4965 (2014).

174. Heuvel, M. van den *et al.* Mechanical and thermal stabilities of peptide amphiphile fibres. *Soft Matter* **7**, 9737–9743 (2011).

175. Yakupova, E. I., Bobyleva, L. G., Vikhlyantsev, I. M. & Bobylev, A. G. Congo Red and amyloids: history and relationship. *Biosci Rep* **39**, BSR20181415 (2019).

176. Fluorescence Sensing. in *Principles of Fluorescence Spectroscopy* (ed. Lakowicz, J. R.) 623–673 (Springer US, 2006). doi:10.1007/978-0-387-46312-4_19.

177. Chan, D. I., Prenner, E. J. & Vogel, H. J. Tryptophan- and arginine-rich antimicrobial peptides: Structures and mechanisms of action. *Biochimica et Biophysica Acta (BBA) - Biomembranes* **1758**, 1184–1202 (2006).

178. de Jesus, A. J. & Allen, T. W. The role of tryptophan side chains in membrane protein anchoring and hydrophobic mismatch. *Biochimica et Biophysica Acta (BBA) - Biomembranes* **1828**, 864–876 (2013).

179. Seo, Y.-W. *et al.* The Cell Death–Inducing Activity of the Peptide Containing Noxa Mitochondrial-Targeting Domain Is Associated with Calcium Release. *Cancer Res* **69**, 8356–8365 (2009).

180. Boohaker, R. J., Lee, M. W., Vishnubhotla, P., Perez, J. M. & Khaled, A. R. The use of therapeutic peptides to target and to kill cancer cells. *Curr. Med. Chem.* **19**, 3794–3804 (2012).

181. Haug, B. E. *et al.* Discovery of a 9-mer Cationic Peptide (LTX-315) as a Potential First in Class Oncolytic Peptide. *J. Med. Chem.* **59**, 2918–2927 (2016).

182. Wei, M. C. *et al.* Proapoptotic BAX and BAK: A Requisite Gateway to Mitochondrial Dysfunction and Death. *Science* **292**, 727–730 (2001).

183. Olejniczak, S. H., Hernandez-Ilizaliturri, F. J., Clements, J. L. & Czuczman, M. S. Acquired Resistance to Rituximab Is Associated with Chemotherapy Resistance Resulting from Decreased Bax and Bak Expression. *Clin Cancer Res* **14**, 1550–1560 (2008).

184. Perego, P. *et al.* Association between Cisplatin Resistance and Mutation of p53 Gene and Reduced Bax Expression in Ovarian Carcinoma Cell Systems. *Cancer Res* **56**, 556–562 (1996).

185. Sawai, H. & Domae, N. Discrimination between primary necrosis and apoptosis by necrostatin-1 in Annexin V-positive/propidium iodide-negative cells. *Biochemical and Biophysical Research Communications* **411**, 569–573 (2011).

186. Hou, L. *et al.* Necrotic pyknosis is a morphologically and biochemically distinct event from apoptotic pyknosis. *Journal of Cell Science* jcs.184374 (2016) doi:10.1242/jcs.184374.

187. Kumar, P., Nagarajan, A. & Uchil, P. D. Analysis of Cell Viability by the Lactate Dehydrogenase Assay. *Cold Spring Harb Protoc* **2018**, pdb.prot095497 (2018).

188. Meghji, P. & Burnstock, G. Inhibition of extracellular ATP degradation in endothelial cells. *Life Sciences* **57**, 763–771 (1995).

189. Tang, D., Kang, R., Berghe, T. V., Vandenabeele, P. & Kroemer, G. The molecular machinery of regulated cell death. *Cell Res* **29**, 347–364 (2019).

190. Walsh, J. G. *et al.* Executioner caspase-3 and caspase-7 are functionally distinct proteases. *Proceedings of the National Academy of Sciences* **105**, 12815–12819 (2008).

191. Schilder, R. J. *et al.* Metallothionein gene expression and resistance to cisplatin in human ovarian cancer. *Int. J. Cancer* **45**, 416–422 (1990).

192. Zhang, Y. *et al.* Temperature-dependent cell death patterns induced by functionalized gold nanoparticle photothermal therapy in melanoma cells. *Sci Rep* **8**, 8720 (2018).

193. Aaes, T. L. *et al.* Vaccination with Necroptotic Cancer Cells Induces Efficient Anti-tumor Immunity. *Cell Reports* **15**, 274–287 (2016).

194. Yu, P. *et al.* Pyroptosis: mechanisms and diseases. *Signal Transduction and Targeted Therapy* **6**, 1–21 (2021).

195. Jiang, X. & Wang, X. Cytochrome ***C*** -Mediated Apoptosis. *Annu. Rev. Biochem.* **73**, 87–106 (2004).

196. Garrido, C. *et al.* Mechanisms of cytochrome c release from mitochondria. *Cell Death Differ* **13**, 1423–1433 (2006).

197. Bhola, P. D. *et al.* High-throughput dynamic BH3 profiling may quickly and accurately predict effective therapies in solid tumors. *Sci. Signal.* **13**, (2020).

198. Gunay, G. *et al.* Antigenic GM3 Lactone Mimetic Molecule Integrated Mannosylated Glycopeptide Nanofibers for the Activation and Maturation of Dendritic Cells. *ACS Appl. Mater. Interfaces* **9**, 16035–16042 (2017).

199. Langevin, H. M., Bouffard, N. A., Badger, G. J., Churchill, D. L. & Howe, A. K. Subcutaneous tissue fibroblast cytoskeletal remodeling induced by acupuncture: Evidence for a mechanotransduction-based mechanism. *J. Cell. Physiol.* **207**, 767–774 (2006).

200. Huber, V. C. *et al.* Distinct Contributions of Vaccine-Induced Immunoglobulin G1 (IgG1) and IgG2a Antibodies to Protective Immunity against Influenza. *Clin Vaccine Immunol* **13**, 981–990 (2006).

201. Shibuya, M., Aoshi, T., Kuroda, E. & Yoshioka, Y. Murine Cross-Reactive Nonneutralizing Polyclonal IgG1 Antibodies Induced by Influenza Vaccine Inhibit the Cross-Protective Effect of IgG2 against Heterologous Virus in Mice. *Journal of Virology* **94**, e00323-20 (2020).

202. Wieczorek, M. *et al.* Major Histocompatibility Complex (MHC) Class I and MHC Class II Proteins: Conformational Plasticity in Antigen Presentation. *Front Immunol* **8**, 292 (2017).

203. Chiti, F. *et al.* Designing conditions for in vitro formation of amyloid protofilaments and fibrils. *Proceedings of the National Academy of Sciences* **96**, 3590–3594 (1999).

204. Dobson, C. M. Protein misfolding, evolution and disease. *Trends in Biochemical Sciences* **24**, 329–332 (1999).

205. Iadanza, M. G., Jackson, M. P., Hewitt, E. W., Ranson, N. A. & Radford, S. E. A new era for understanding amyloid structures and disease. *Nature Reviews Molecular Cell Biology* **19**, 755–773 (2018).

206. Gallardo, R., Ranson, N. A. & Radford, S. E. Amyloid structures: much more than just a cross-β fold. *Current Opinion in Structural Biology* **60**, 7–16 (2020).

207. Jia, Z., Schmit, J. D. & Chen, J. Amyloid assembly is dominated by misregistered kinetic traps on an unbiased energy landscape. *Proceedings of the National Academy of Sciences* **117**, 10322–10328 (2020).

208. Kulenkampff, K., Wolf Perez, A.-M., Sormanni, P., Habchi, J. & Vendruscolo, M. Quantifying misfolded protein oligomers as drug targets and biomarkers in Alzheimer and Parkinson diseases. *Nat Rev Chem* **5**, 277–294 (2021).

209. Fusco, G. *et al.* Structural basis of membrane disruption and cellular toxicity by α-synuclein oligomers. *Science* **358**, 1440–1443 (2017).

210. Yasumoto, T. *et al.* High molecular weight amyloid β1-42 oligomers induce neurotoxicity via plasma membrane damage. *Alzheimer's & Dementia* **16**, e037546 (2020).

211. Milner, M. T., Maddugoda, M., Götz, J., Burgener, S. S. & Schroder, K. The NLRP3 inflammasome triggers sterile neuroinflammation and Alzheimer's disease. *Current Opinion in Immunology* **68**, 116–124 (2021).

212. McKenzie, B. A., Dixit, V. M. & Power, C. Fiery Cell Death: Pyroptosis in the Central Nervous System. *Trends in Neurosciences* **43**, 55–73 (2020).

213. Walsh, D. M. & Selkoe, D. J. Amyloid β-protein and beyond: the path forward in Alzheimer's disease. *Current Opinion in Neurobiology* **61**, 116–124 (2020).

214. Guo, A. Z., Fluitt, A. M. & de Pablo, J. J. Early-stage human islet amyloid polypeptide aggregation: Mechanisms behind dimer formation. *J. Chem. Phys.* **149**, 025101 (2018).

215. Serrano, A. L., Lomont, J. P., Tu, L.-H., Raleigh, D. P. & Zanni, M. T. A Free Energy Barrier Caused by the Refolding of an Oligomeric Intermediate Controls the Lag Time of Amyloid Formation by hIAPP. *J. Am. Chem. Soc.* **139**, 16748–16758 (2017).

216. Fan, J. *et al.* Modeling amide-I vibrations of alanine dipeptide in solution by using neural network protocol. *Spectrochimica Acta Part A: Molecular and Biomolecular Spectroscopy* **268**, 120675 (2022).

217. Kazman, P., Absmeier, R. M., Engelhardt, H. & Buchner, J. Dissection of the amyloid formation pathway in AL amyloidosis. *Nat Commun* **12**, 6516 (2021).

218. Gunay, G. *et al.* Peptide Aggregation Induced Immunogenic Rupture (PAIIR). *Advanced Science* **n/a**, 2105868 (2022).

219. Leong, Y. Q., Ng, K. Y., Chye, S. M., Ling, A. P. K. & Koh, R. Y. Mechanisms of action of amyloid-beta and its precursor protein in neuronal cell death. *Metab Brain Dis* **35**, 11–30 (2020).

220. Finn, T. E., Nunez, A. C., Sunde, M. & Easterbrook-Smith, S. B. Serum Albumin Prevents Protein Aggregation and Amyloid Formation and Retains Chaperone-like Activity in the Presence of Physiological Ligands. *Journal of Biological Chemistry* **287**, 21530–21540 (2012).

221. Zhao, M. & Guo, C. Multipronged Regulatory Functions of Serum Albumin in Early Stages of Amyloid-β Aggregation. *ACS Chem. Neurosci.* **12**, 2409–2420 (2021).

222. Picón-Pagès, P. *et al.* Human Albumin Impairs Amyloid β-peptide Fibrillation Through its C-terminus: From docking Modeling to Protection Against Neurotoxicity in Alzheimer's disease. *Computational and Structural Biotechnology Journal* **17**, 963–971 (2019).

223. Kakinen, A., Javed, I., Faridi, A., Davis, T. P. & Ke, P. C. Serum albumin impedes the amyloid aggregation and hemolysis of human islet amyloid polypeptide and alpha synuclein. *Biochimica et Biophysica Acta (BBA) - Biomembranes* **1860**, 1803–1809 (2018).

224. Bond, S., Lopez-Lloreda, C., Gannon, P. J., Akay-Espinoza, C. & Jordan-Sciutto, K. L. The Integrated Stress Response and Phosphorylated Eukaryotic Initiation Factor 2α in

Neurodegeneration. *Journal of Neuropathology & Experimental Neurology* **79**, 123–143 (2020).

225. Ohno, M. Roles of eIF2Î± kinases in the pathogenesis of Alzheimerâ€™s disease. *Front. Mol. Neurosci.* **7**, (2014).

226. Yerlikaya, A., Kimball, S. R. & Stanley, B. A. Phosphorylation of eIF2α in response to 26S proteasome inhibition is mediated by the haem-regulated inhibitor (HRI) kinase. *Biochemical Journal* **412**, 579–588 (2008).

227. Cui, X., Hartanto, Y. & Zhang, H. Advances in multicellular spheroids formation. *J R Soc Interface* **14**, (2017).

228. Heyer, J., Kwong, L. N., Lowe, S. W. & Chin, L. Non-germline genetically engineered mouse models for translational cancer research. *Nature Reviews Cancer* **10**, 470–480 (2010).

229. Curzer, H. J., Perry, G., Wallace, M. C. & Perry, D. The Three Rs of Animal Research: What they Mean for the Institutional Animal Care and Use Committee and Why. *Sci Eng Ethics* **22**, 549–565 (2016).

230. Innovation or Stagnation: Challenge and Opportunity on the Critical Path to New Medical Products. Preprint at https://www.who.int/intellectualproperty/documents/en/FDAproposals.pdf (2004).

231. Mak, I. W., Evaniew, N. & Ghert, M. Lost in translation: animal models and clinical trials in cancer treatment. *Am J Transl Res* **6**, 114–118 (2014).

232. Bledsoe, M. J. & Grizzle, W. E. Use of human specimens in research: the evolving United States regulatory, policy, and scientific landscape. *Diagn Histopathol (Oxf)* **19**, 322–330 (2013).

233. Mueller-Klieser, W. Multicellular spheroids. *J Cancer Res Clin Oncol* **113**, 101–122 (1987).

234. Doyle, A. D. & Yamada, K. M. Mechanosensing via cell-matrix adhesions in 3D microenvironments. *Experimental Cell Research* **343**, 60–66 (2016).

235. Longati, P. *et al.* 3D pancreatic carcinoma spheroids induce a matrix-rich, chemoresistant phenotype offering a better model for drug testing. *BMC Cancer* **13**, 1–13 (2013).

236. Khawar, I. A. *et al.* Three Dimensional Mixed-Cell Spheroids Mimic Stroma-Mediated Chemoresistance and Invasive Migration in hepatocellular carcinoma. *Neoplasia* **20**, 800–812 (2018).

237. Melissaridou, S. *et al.* The effect of 2D and 3D cell cultures on treatment response, EMT profile and stem cell features in head and neck cancer. *Cancer Cell Int* **19**, 1–10 (2019).

238. Gunay, G. *et al.* The effects of size and shape of the ovarian cancer spheroids on the drug resistance and migration. *Gynecologic Oncology* (2020) doi:10.1016/j.ygyno.2020.09.002.

239. Rafehi, S. *et al.* TGFβ signaling regulates epithelial–mesenchymal plasticity in ovarian cancer ascites-derived spheroids. *Endocrine-Related Cancer* **23**, 147–159 (2016).

240. Mehta, G., Hsiao, A. Y., Ingram, M., Luker, G. D. & Takayama, S. Opportunities and challenges for use of tumor spheroids as models to test drug delivery and efficacy. *Journal of Controlled Release* **164**, 192–204 (2012).

241. Sutherland, R. M., McCredie, J. A. & Inch, W. R. Growth of Multicell Spheroids in Tissue Culture as a Model of Nodular Carcinomas. *J Natl Cancer Inst* **46**, 113–120 (1971).

242. Sutherland, R. M. Cell and environment interactions in tumor microregions: the multicell spheroid model. *Science* **240**, 177–184 (1988).

243. Alvarez-Pérez, J., Ballesteros, P. & Cerdán, S. Microscopic images of intraspheroidal pH by 1H magnetic resonance chemical shift imaging of pH sensitive indicators. *MAGMA* **18**, 293–301 (2005).

244. Curcio, E. *et al.* Mass transfer and metabolic reactions in hepatocyte spheroids cultured in rotating wall gas-permeable membrane system. *Biomaterials* **28**, 5487–5497 (2007).

245. Hirschhaeuser, F. *et al.* Multicellular tumor spheroids: An underestimated tool is catching up again. *Journal of Biotechnology* **148**, 3–15 (2010).

246. Kim, Y. J. *et al.* A microchip filter device incorporating slit arrays and 3-D flow for detection of circulating tumor cells using CAV1-EpCAM conjugated microbeads. *Biomaterials* **35**, 7501–7510 (2014).

247. Lin, R.-Z. & Chang, H.-Y. Recent advances in three-dimensional multicellular spheroid culture for biomedical research. *Biotechnol. J.* **3**, 1172–1184 (2008).

248. Souza, G. R. *et al.* Three-dimensional tissue culture based on magnetic cell levitation. *Nature Nanotech* **5**, 291–296 (2010).

249. Chaudhuri, P. K., Low, B. C. & Lim, C. T. Mechanobiology of Tumor Growth. *Chem. Rev.* **118**, 6499–6515 (2018).

250. Antunes, J. *et al.* In-air production of 3D co-culture tumor spheroid hydrogels for expedited drug screening. *Acta Biomaterialia* **94**, 392–409 (2019).

251. Moshksayan, K. *et al.* Spheroids-on-a-chip: Recent advances and design considerations in microfluidic platforms for spheroid formation and culture. *Sensors and Actuators B: Chemical* **263**, 151–176 (2018).

252. Acikgöz, A., Giri, S., Cho, M.-G. & Bader, A. Morphological and Functional Analysis of Hepatocyte Spheroids Generated on Poly-HEMA-Treated Surfaces under the Influence of Fetal Calf Serum and Nonparenchymal Cells. *Biomolecules* **3**, 242–269 (2013).

253. Ariyoshi, W. *et al.* 3D spheroid culture models for chondrocytes using polyethylene glycol-coated microfabricated chip. *Biomed. Res.* **41**, 187–197 (2020).

254. Bell, C. C. *et al.* Characterization of primary human hepatocyte spheroids as a model system for drug-induced liver injury, liver function and disease. *Scientific Reports* **6**, 25187 (2016).

255. Costa, E. C., Melo-Diogo, D. de, Moreira, A. F., Carvalho, M. P. & Correia, I. J. Spheroids Formation on Non-Adhesive Surfaces by Liquid Overlay Technique: Considerations and Practical Approaches. *Biotechnology Journal* **13**, 1700417 (2018).

256. Tu, T.-Y. *et al.* Rapid Prototyping of Concave Microwells for the Formation of 3D Multicellular Cancer Aggregates for Drug Screening. *Adv. Healthcare Mater.* **3**, 609–616 (2014).

257. Chao, C., Ngo, L. P. & Engelward, B. P. SpheroidChip: Patterned Agarose Microwell Compartments Harboring HepG2 Spheroids are Compatible with Genotoxicity Testing. *ACS Biomater. Sci. Eng.* **6**, 2427–2439 (2020).

258. Gong, X. *et al.* Generation of Multicellular Tumor Spheroids with Microwell-Based Agarose Scaffolds for Drug Testing. *PLOS ONE* **10**, e0130348 (2015).

259. Mirab, F., Kang, Y. J. & Majd, S. Preparation and characterization of size-controlled glioma spheroids using agarose hydrogel microwells. *PLOS ONE* **14**, e0211078 (2019).

260. Casey, R. C. *et al.* β1-Integrins Regulate the Formation and Adhesion of Ovarian Carcinoma Multicellular Spheroids. *The American Journal of Pathology* **159**, 2071–2080 (2001).

261. Del Duca, D., Werbowetski, T. & Del Maestro, R. F. Spheroid Preparation from Hanging Drops: Characterization of a Model of Brain Tumor Invasion. *J Neurooncol* **67**, 295–303 (2004).

262. Kelm, J. M., Timmins, N. E., Brown, C. J., Fussenegger, M. & Nielsen, L. K. Method for generation of homogeneous multicellular tumor spheroids applicable to a wide variety of cell types. *Biotechnol. Bioeng.* **83**, 173–180 (2003).

263. Tung, Y.-C. *et al.* High-throughput 3D spheroid culture and drug testing using a 384 hanging drop array. *Analyst* **136**, 473–478 (2011).

264. Amaral, R. L. F., Miranda, M., Marcato, P. D. & Swiech, K. Comparative Analysis of 3D Bladder Tumor Spheroids Obtained by Forced Floating and Hanging Drop Methods for Drug Screening. *Front. Physiol.* **8**, 605 (2017).

265. Achilli, T.-M., Meyer, J. & Morgan, J. R. Advances in the formation, use and understanding of multi-cellular spheroids. *Expert Opinion on Biological Therapy* **12**, 1347–1360 (2012).

266. Castañeda, F. & Kinne, R. K. H. Short exposure to millimolar concentrations of ethanol induces apoptotic cell death in multicellular HepG2 spheroids. *J Cancer Res Clin Oncol* **126**, 305–310 (2000).

267. Okubo, H. *et al.* A Novel Method for Faster Formation of Rat Liver Cell Spheroids. *Artificial Organs* **26**, 497–505 (2002).

268. Jaganathan, H. *et al.* Three-Dimensional In Vitro Co-Culture Model of Breast Tumor using Magnetic Levitation. *Sci Rep* **4**, 6468 (2015).

269. Daquinag, A. C., Souza, G. R. & Kolonin, M. G. Adipose Tissue Engineering in Three-Dimensional Levitation Tissue Culture System Based on Magnetic Nanoparticles. *Tissue Engineering Part C: Methods* **19**, 336–344 (2013).

270. Tseng, H. *et al.* Assembly of a Three-Dimensional Multitype Bronchiole Coculture Model Using Magnetic Levitation. *Tissue Engineering Part C: Methods* **19**, 665–675 (2013).

271. Lewis, N. S. *et al.* Magnetically levitated mesenchymal stem cell spheroids cultured with a collagen gel maintain phenotype and quiescence. *J Tissue Eng* **8**, (2017).

272. Wang, Z. *et al.* Inhibitory effects of a gradient static magnetic field on normal angiogenesis. *Bioelectromagnetics* **30**, 446–453 (2009).

273. Torre, L. A. *et al.* Ovarian cancer statistics, 2018: Ovarian Cancer Statistics, 2018. *CA: A Cancer Journal for Clinicians* **68**, 284–296 (2018).

274. Lengyel, E. Ovarian cancer development and metastasis. *American Journal of Pathology* **177**, 1053–1064 (2010).

275. Kipps, E., Tan, D. S. P. & Kaye, S. B. Meeting the challenge of ascites in ovarian cancer: New avenues for therapy and research. *Nature Reviews Cancer* (2013) doi:10.1038/nrc3432.

276. Ayantunde, A. A. & Parsons, S. L. Pattern and prognostic factors in patients with malignant ascites: a retrospective study. *Annals of Oncology* **18**, 945–949 (2007).

277. Al Habyan, S., Kalos, C., Szymborski, J. & McCaffrey, L. Multicellular detachment generates metastatic spheroids during intra-abdominal dissemination in epithelial ovarian cancer. *Oncogene* (2018) doi:10.1038/s41388-018-0317-x.

278. Xing, H. *et al.* Knock-down of P-glycoprotein reverses taxol resistance in ovarian cancer multicellular spheroids. *Oncol Rep* (2007) doi:10.3892/or.17.1.117.

279. Burleson, K. M., Boente, M. P., Pambuccian, S. E. & Skubitz, A. P. N. Disaggregation and invasion of ovarian carcinoma ascites spheroids. *J Transl Med* **4**, 6 (2006).

280. Yung, S., Li, F. K. & Chan, T. M. Peritoneal mesothelial cell culture and biology. *Perit Dial Int* **26**, 162–173 (2006).

281. Allen, H. J., Porter, C., Gamarra, M., Piver, S. & Johnson, E. A. Z. Isolation and Morphologic Characterization of Human Ovarian Carcinoma Cell Clusters Present in Effusions. *Pathobiology* (2008) doi:10.1159/000163419.

282. Latifi, A. *et al.* Isolation and Characterization of Tumor Cells from the Ascites of Ovarian Cancer Patients: Molecular Phenotype of Chemoresistant Ovarian Tumors. *PLoS ONE* **7**, e46858 (2012).

283. Thiery, J. P., Acloque, H., Huang, R. Y. J. & Nieto, M. A. Epithelial-Mesenchymal Transitions in Development and Disease. *Cell* **139**, 871–890 (2009).

284. Gheldof, A. & Berx, G. Cadherins and Epithelial-to-Mesenchymal Transition. in *Progress in Molecular Biology and Translational Science* vol. 116 317–336 (Elsevier, 2013).

285. Bagnato, A. & Rosanò, L. Epithelial-Mesenchymal Transition in Ovarian Cancer Progression: A Crucial Role for the Endothelin Axis. *Cells Tissues Organs* **185**, 85–94 (2007).

286. Angst, B. D., Marcozzi, C. & Magee, A. I. The cadherin superfamily: diversity in form and function. *J. Cell. Sci.* **114**, 629–641 (2001).

287. Lin, R.-Z., Chou, L.-F., Chien, C.-C. M. & Chang, H.-Y. Dynamic analysis of hepatoma spheroid formation: roles of E-cadherin and β1-integrin. *Cell Tissue Res* **324**, 411–422 (2006).

288. van Roy, F. & Berx, G. The cell-cell adhesion molecule E-cadherin. *Cell. Mol. Life Sci.* **65**, 3756–3788 (2008).

289. Auersperg, N., Wong, A. S. T., Choi, K.-C., Kang, S. K. & Leung, P. C. K. Ovarian Surface Epithelium: Biology, Endocrinology, and Pathology [1]. *Endocrine Reviews* **22**, 255–288 (2001).

290. Mendez, M. G., Kojima, S. & Goldman, R. D. Vimentin induces changes in cell shape, motility, and adhesion during the epithelial to mesenchymal transition. *FASEB j.* **24**, 1838–1851 (2010).

291. Eckes, B. *et al.* Impaired mechanical stability, migration and contractile capacity in vimentin-deficient fibroblasts. *J. Cell. Sci.* **111 (Pt 13)**, 1897–1907 (1998).

292. Kidd, M. E., Shumaker, D. K. & Ridge, K. M. The Role of Vimentin Intermediate Filaments in the Progression of Lung Cancer. *Am J Respir Cell Mol Biol* 130827094923003 (2013) doi:10.1165/rcmb.2013-0314TR.

293. Hudson, L. G., Zeineldin, R. & Stack, M. S. Phenotypic plasticity of neoplastic ovarian epithelium: unique cadherin profiles in tumor progression. *Clin. Exp. Metastasis* **25**, 643–655 (2008).

294. Ahmed, N., Thompson, E. W. & Quinn, M. A. Epithelial-mesenchymal interconversions in normal ovarian surface epithelium and ovarian carcinomas: an exception to the norm. *J. Cell. Physiol.* **213**, 581–588 (2007).

295. Pampaloni, F., Reynaud, E. G. & Stelzer, E. H. K. The third dimension bridges the gap between cell culture and live tissue. *Nature Reviews Molecular Cell Biology* Preprint at https://doi.org/10.1038/nrm2236 (2007).

296. Sontheimer-Phelps, A., Hassell, B. A. & Ingber, D. E. Modelling cancer in microfluidic human organs-on-chips. *Nature Reviews Cancer* Preprint at https://doi.org/10.1038/s41568-018-0104-6 (2019).

297. Casey, R. C. *et al.* Beta 1-integrins regulate the formation and adhesion of ovarian carcinoma multicellular spheroids. *Am. J. Pathol.* **159**, 2071–2080 (2001).

298. Auersperg, N. *et al.* E-cadherin induces mesenchymal-to-epithelial transition in human ovarian surface epithelium. *Proceedings of the National Academy of Sciences* **96**, 6249–6254 (1999).

299. Marques, F. R., Fonsechi-Carvasan, G. A., De Angelo Andrade, L. A. L. & Böttcher-Luiz, F. Immunohistochemical patterns for α- and β-catenin, E- and N-cadherin expression in ovarian epithelial tumors. *Gynecologic Oncology* **94**, 16–24 (2004).

300. Davies, Worsley, & Ponder. Expression of E-cadherin, α-catenin and β-catenin in normal ovarian surface epithelium and epithelial ovarian cancers. *Histopathology* **32**, 69–80 (1998).

301. Haley, J. *et al.* Functional characterization of a panel of high-grade serous ovarian cancer cell lines as representative experimental models of the disease. *Oncotarget* **7**, (2016).

302. Hirschhaeuser, F. *et al.* Multicellular tumor spheroids: An underestimated tool is catching up again. *Journal of Biotechnology* **148**, 3–15 (2010).

303. Park, M. C. *et al.* Novel Morphologic and Genetic Analysis of Cancer Cells in a 3D Microenvironment Identifies STAT3 as a Regulator of Tumor Permeability Barrier Function. *Cancer Research* **76**, 1044–1054 (2016).

304. Takayama, S. *et al.* Formation of stable small cell number three-dimensional ovarian cancer spheroids using hanging drop arrays for preclinical drug sensitivity assays. *Gynecologic Oncology* (2015) doi:10.1016/j.ygyno.2015.04.014.

305. Horst, E. N. *et al.* Comparative analysis of tumor spheroid generation techniques for differential in vitro drug toxicity. *Oncotarget* (2016) doi:10.18632/oncotarget.7659.

306. Shi, W. *et al.* Facile Tumor Spheroids Formation in Large Quantity with Controllable Size and High Uniformity. *Sci Rep* **8**, 6837 (2018).

307. Nath, S. & Devi, G. R. Three-dimensional culture systems in cancer research: Focus on tumor spheroid model. *Pharmacology & Therapeutics* **163**, 94–108 (2016).

308. Santo, V. E. *et al.* Adaptable stirred-tank culture strategies for large scale production of multicellular spheroid-based tumor cell models. *Journal of Biotechnology* **221**, 118–129 (2016).

309. le Roux, L. *et al.* Optimizing Imaging of Three-Dimensional Multicellular Tumor Spheroids with Fluorescent Reporter Proteins Using Confocal Microscopy. *Mol Imaging* **7**, 7290.2008.00023 (2008).

310. Heine, J. *et al.* Three dimensional live-cell STED microscopy at increased depth using a water immersion objective. *Review of Scientific Instruments* **89**, 053701 (2018).

311. Uygur, B. & Wu, W.-S. SLUG promotes prostate cancer cell migration and invasion via CXCR4/CXCL12 axis. *Mol Cancer* **10**, 139 (2011).

312. Domcke, S., Sinha, R., Levine, D. A., Sander, C. & Schultz, N. Evaluating cell lines as tumour models by comparison of genomic profiles. *Nat Commun* **4**, 2126 (2013).

313. Lovitt, C., Shelper, T. & Avery, V. Advanced Cell Culture Techniques for Cancer Drug Discovery. *Biology* **3**, 345–367 (2014).

314. Smith, J. A., Ngo, H., Martin, M. C. & Wolf, J. K. An evaluation of cytotoxicity of the taxane and platinum agents combination treatment in a panel of human ovarian carcinoma cell lines. *Gynecologic Oncology* **98**, 141–145 (2005).

315. Untch, M. *et al.* Evaluation of Paclitaxel (Taxol), Cisplatin, and the Combination Paclitaxel-Cisplatin in Ovarian Cancer in Vitro with the ATP Cell Viability Assay. *Gynecologic Oncology* **53**, 44–49 (1994).

316. du Bois, A. A Randomized Clinical Trial of Cisplatin/Paclitaxel Versus Carboplatin/Paclitaxel as First-Line Treatment of Ovarian Cancer. *CancerSpectrum Knowledge Environment* **95**, 1320–1329 (2003).

317. Bicaku, E. *et al.* In vitro analysis of ovarian cancer response to cisplatin, carboplatin, and paclitaxel identifies common pathways that are also associated with overall patient survival. *Br J Cancer* **106**, 1967–1975 (2012).

318. McGrail, D. J. *et al.* Alterations in Ovarian Cancer Cell Adhesion Drive Taxol Resistance by Increasing Microtubule Dynamics in a FAK-dependent Manner. *Sci Rep* **5**, 9529 (2015).

319. Muenyi, C. S. *et al.* Sodium Arsenite ± Hyperthermia Sensitizes p53-Expressing Human Ovarian Cancer Cells to Cisplatin by Modulating Platinum-DNA Damage Responses. *Toxicological Sciences* **127**, 139–149 (2012).

320. Kijanska, M. & Kelm, J. In vitro 3D Spheroids and Microtissues: ATP-based Cell Viability and Toxicity Assays. in *Assay Guidance Manual* (eds. Sittampalam, G. S. et al.) (Eli Lilly & Company and the National Center for Advancing Translational Sciences, 2004).

321. Mittler, F. *et al.* High-Content Monitoring of Drug Effects in a 3D Spheroid Model. *Front. Oncol.* **7**, 293 (2017).

322. Yvon, A.-M. C., Wadsworth, P. & Jordan, M. A. Taxol Suppresses Dynamics of Individual Microtubules in Living Human Tumor Cells. *MBoC* **10**, 947–959 (1999).

323. Dasari, S. & Bernard Tchounwou, P. Cisplatin in cancer therapy: Molecular mechanisms of action. *European Journal of Pharmacology* **740**, 364–378 (2014).

324. Yap, A. S. The Morphogenetic Role of Cadherin Cell Adhesion Molecules in Human Cancer: A Thematic Review. *Cancer Investigation* **16**, 252–261 (1998).

325. Rosso, M. *et al.* E-cadherin: A determinant molecule associated with ovarian cancer progression, dissemination and aggressiveness. *PLoS ONE* (2017) doi:10.1371/journal.pone.0184439.

326. Huang, R. Y.-J. *et al.* An EMT spectrum defines an anoikis-resistant and spheroidogenic intermediate mesenchymal state that is sensitive to e-cadherin restoration by a src-kinase inhibitor, saracatinib (AZD0530). *Cell Death Dis* **4**, e915 (2013).

327. Yi, B.-R., Kim, T.-H., Kim, Y.-S. & Choi, K.-C. Alteration of epithelial-mesenchymal transition markers in human normal ovaries and neoplastic ovarian cancers. *International Journal of Oncology* **46**, 272–280 (2015).

328. Davidowitz, R. A. *et al.* Mesenchymal gene program–expressing ovarian cancer spheroids exhibit enhanced mesothelial clearance. *J. Clin. Invest.* **124**, 2611–2625 (2014).

329. Hosono, S. *et al.* Expression of Twist increases the risk for recurrence and for poor survival in epithelial ovarian carcinoma patients. *Br J Cancer* **96**, 314–320 (2007).

330. Jin, H. *et al.* Snail is critical for tumor growth and metastasis of ovarian carcinoma. *Int. J. Cancer* n/a-n/a (2009) doi:10.1002/ijc.24901.

331. Bagnato, A. & Rosanò, L. Understanding and overcoming chemoresistance in ovarian cancer: emerging role of the endothelin axis. *Curr. Oncol.* **19**, 36–38 (2012).

332. Gu, A., Jie, Y., Yao, Q., Zhang, Y. & Mingyan, E. Slug Is Associated With Tumor Metastasis and Angiogenesis in Ovarian Cancer. *Reprod Sci* **24**, 291–299 (2017).

333. Li, Y. *et al.* Slug contributes to cancer progression by direct regulation of ERα signaling pathway. *International Journal of Oncology* **46**, 1461–1472 (2015).

334. Kurrey, N. K., K, A. & Bapat, S. A. Snail and Slug are major determinants of ovarian cancer invasiveness at the transcription level. *Gynecologic Oncology* **97**, 155–165 (2005).

335. Mao, M. *et al.* Effects of CD44 and E-cadherin overexpression on the proliferation, adhesion and invasion of ovarian cancer cells. *Exp Ther Med* (2017) doi:10.3892/etm.2017.5259.

336. Hirst, J. *et al.* Licofelone Enhances the Efficacy of Paclitaxel in Ovarian Cancer by Reversing Drug Resistance and Tumor Stem-like Properties. *Cancer Res* **78**, 4370–4385 (2018).

337. DesRochers, T. M., Suter, L., Roth, A. & Kaplan, D. L. Bioengineered 3D Human Kidney Tissue, a Platform for the Determination of Nephrotoxicity. *PLoS ONE* **8**, e59219 (2013).

338. Chowanadisai, W. *et al.* Cisplatin Resistant Spheroids Model Clinically Relevant Survival Mechanisms in Ovarian Tumors. *PLoS ONE* **11**, e0151089 (2016).

339. Godwin, A. K. *et al.* High resistance to cisplatin in human ovarian cancer cell lines is associated with marked increase of glutathione synthesis. *Proceedings of the National Academy of Sciences* **89**, 3070–3074 (1992).

340. Gadiyar, V. *et al.* Cell Death in the Tumor Microenvironment: Implications for Cancer Immunotherapy. *Cells* **9**, 2207 (2020).

341. Fabian, K. P., Wolfson, B. & Hodge, J. W. From Immunogenic Cell Death to Immunogenic Modulation: Select Chemotherapy Regimens Induce a Spectrum of Immune-Enhancing Activities in the Tumor Microenvironment. *Front. Oncol.* **11**, 728018 (2021).

342. Golden, E. B. & Apetoh, L. Radiotherapy and Immunogenic Cell Death. *Seminars in Radiation Oncology* **25**, 11–17 (2015).

343. Gunay, G. *et al.* Peptide Aggregation Induced Immunogenic Rupture (PAIIR). *Advanced Science* **472230**, (2022).

344. Van Norman, G. A. Limitations of Animal Studies for Predicting Toxicity in Clinical Trials. *JACC: Basic to Translational Science* **4**, 845–854 (2019).

345. Mehta, G., Hsiao, A. Y., Ingram, M., Luker, G. D. & Takayama, S. Opportunities and challenges for use of tumor spheroids as models to test drug delivery and efficacy. *Journal of Controlled Release* **164**, 192–204 (2012).

346. Duval, K. *et al.* Modeling Physiological Events in 2D vs. 3D Cell Culture. *Physiology* **32**, 266–277 (2017).

347. Imamura, Y. *et al.* Comparison of 2D- and 3D-culture models as drug-testing platforms in breast cancer. *Oncology Reports* **33**, 1837–1843 (2015).

348. Rodríguez, C. E., Reidel, S. I., Bal de Kier Joffé, E. D., Jasnis, M. A. & Fiszman, G. L. Autophagy Protects from Trastuzumab-Induced Cytotoxicity in HER2 Overexpressing Breast Tumor Spheroids. *PLoS ONE* **10**, e0137920 (2015).

349. Demuynck, R., Efimova, I., Lin, A., Declercq, H. & Krysko, D. V. A 3D Cell Death Assay to Quantitatively Determine Ferroptosis in Spheroids. *Cells* **9**, 703 (2020).

350. Yu, J. W. *et al.* Tumor-immune profiling of murine syngeneic tumor models as a framework to guide mechanistic studies and predict therapy response in distinct tumor microenvironments. *PLoS ONE* **13**, e0206223 (2018).

351. Kamatar, A., Gunay, G. & Acar, H. Natural and Synthetic Biomaterials for Engineering Multicellular Tumor Spheroids. *Polymers* **12**, 2506 (2020).

352. Gunay, G. *et al.* The effects of size and shape of the ovarian cancer spheroids on the drug resistance and migration. *Gynecologic Oncology* **159**, 563–572 (2020).

353. Jing, X. *et al.* Role of hypoxia in cancer therapy by regulating the tumor microenvironment. *Mol Cancer* **18**, 157 (2019).

354. Hirschhaeuser, F. *et al.* Multicellular tumor spheroids: An underestimated tool is catching up again. *Journal of Biotechnology* **148**, 3–15 (2010).

355. Yan, F. *et al.* Characterization and quantification of necrotic tissues and morphology in multicellular ovarian cancer tumor spheroids using optical coherence tomography. *Biomed. Opt. Express, BOE* **12**, 3352–3371 (2021).

356. Biancalana, M. & Koide, S. Molecular mechanism of Thioflavin-T binding to amyloid fibrils. *Biochimica et Biophysica Acta (BBA) - Proteins and Proteomics* **1804**, 1405–1412 (2010).

357. Bensen, R. C. *et al.* Small Molecule Targeting of Oxysterol-Binding Protein (OSBP)-Related Protein 4 and OSBP Inhibits Ovarian Cancer Cell Proliferation in Monolayer and Spheroid Cell Models. *ACS Pharmacol. Transl. Sci.* (2021) doi:10.1021/acsptsci.0c00207.

358. Azharuddin, M. *et al.* Dissecting multi drug resistance in head and neck cancer cells using multicellular tumor spheroids. *Sci Rep* **9**, 20066 (2019).

359. Nunes, A. S., Barros, A. S., Costa, E. C., Moreira, A. F. & Correia, I. J. 3D tumor spheroids as in vitro models to mimic in vivo human solid tumors resistance to therapeutic drugs: NUNES ET AL. *Biotechnology and Bioengineering* **116**, 206–226 (2019).

360. Perche, F. & Torchilin, V. P. Cancer cell spheroids as a model to evaluate chemotherapy protocols. *Cancer Biology & Therapy* **13**, 1205–1213 (2012).

361. Krukiewicz, K. & Zak, J. K. Biomaterial-based regional chemotherapy: Local anticancer drug delivery to enhance chemotherapy and minimize its side-effects. *Materials Science and Engineering: C* **62**, 927–942 (2016).

362. Shahar, N. & Larisch, S. Inhibiting the inhibitors: Targeting anti-apoptotic proteins in cancer and therapy resistance. *Drug Resistance Updates* **52**, 100712 (2020).

363. Land, W. G. The Role of Damage-Associated Molecular Patterns (DAMPs) in Human Diseases. *Sultan Qaboos Univ Med J* **15**, e157–e170 (2015).

364. Eisenächer, K., Steinberg, C., Reindl, W. & Krug, A. The role of viral nucleic acid recognition in dendritic cells for innate and adaptive antiviral immunity. *Immunobiology* **212**, 701–714 (2008).

365. Sistigu, A. *et al.* Cancer cell–autonomous contribution of type I interferon signaling to the efficacy of chemotherapy. *Nat Med* **20**, 1301–1309 (2014).

366. Suzuki, K. *et al.* Activation of target-tissue immune-recognition molecules by double-stranded polynucleotides. *Proceedings of the National Academy of Sciences* **96**, 2285–2290 (1999).

367. Chen, S.-H. *et al.* O6-methylguanine-DNA methyltransferase modulates cisplatin-induced DNA double-strand breaks by targeting the homologous recombination pathway in nasopharyngeal carcinoma. *J Biomed Sci* **28**, 2 (2021).

368. Bianchi, M. E. DAMPs from cell death to new life. *Frontiers in Immunology* **6**, 11 (2015).

369. Mortezaee, K. *et al.* NF-κB targeting for overcoming tumor resistance and normal tissues toxicity. *Journal Cellular Physiology* **234**, 17187–17204 (2019).

370. Hong, W. X. *et al.* Intratumoral Immunotherapy for Early-stage Solid Tumors. *Clin Cancer Res* **26**, 3091–3099 (2020).